Università degli Studi di Padova

Department of Information Engineering

Ph.D. Course on Information Engineering

Curriculum: Information Science and Technologies

XXXII Series

Analysis of degradation mechanisms induced by electrical over-stress on high efficiency gallium nitride LEDs

Ph.D Student

Nicola Renso

Supervisor

Prof. Matteo Meneghini

Coordinator

Ch.mo Prof. Andrea Neviani

Academic Year 2018/2019

Contents

Abstract **v**

Sommario **vii**

Publications **ix**

Introduction **xi**

1 Principles of Light Emitting Diodes **1**

1.1 Radiative recombination 1

1.1.1 Radiative recombination for low-level excitation 2

1.1.2 Radiative recombination for high-level excitation 3

1.1.3 Luminescence decay 4

1.2 Non-radiative recombination 5

1.2.1 Auger recombination 6

1.2.2 Non-radiative recombination at surfaces 7

1.3 Internal quantum efficiency 9

1.4 Electrical properties of LEDs 10

1.4.1 p-n junction 10

1.4.2 I-V characteristic 12

1.4.3 Non ideality in the I-V characteristic 13

1.4.4 Carrier distribution in homojunction and heterojunction 16

1.4.5 Heterojunctions characteristics 17

1.5 Optical properties of LEDs 23

1.5.1 LED efficiency 23

1.5.2 Emission spectrum 24

1.5.3 L-I characteristic 26

1.5.4 Light extraction 28

1.6 Reverse bias conduction mechanisms 30

1.7 Degradation mechanisms 33

1.7.1 Gradual degradation mechanisms 33

1.7.2 Catastrophic degradation 36

2 Advanced characterization techniques **39**
2.1 Deep Level Transient Spectroscopy (DLTS) . . . 39
2.1.1 Capacitance Transient . . . 39
2.1.2 Bias Voltage Pulses . . . 42
2.1.3 DLTS measurement procedure . . . 43
2.1.4 The dual-gate integrator (double boxcar) . . . 44
2.1.5 Trap concentration profile . . . 46
2.1.6 Capture process characterization . . . 49
2.2 Deep Level Optical Spectroscopy . . . 50
2.2.1 The working principle . . . 50
2.2.2 The experimental procedure . . . 52
2.2.3 Steady-State Photo-Capacitance . . . 54

3 Effects of growth parameters of GaN-based LEDs on the ESD robustness **57**
3.1 Variations on n-side . . . 57
3.1.1 DC and pulsed characterization . . . 58
3.1.2 Capacitance DLTS measurements . . . 62
3.1.3 Optical DLTS measurements . . . 64
3.2 Variations on p-side . . . 66
3.2.1 DC and pulsed characterization . . . 66
3.2.2 Capacitance DLTS characterization . . . 73
3.2.3 Global comparison . . . 77
3.2.4 Arrhenius analysis of identified defects . . . 77
3.3 Closing remarks . . . 78

4 Failure limits of GaN-based LEDs under EOS **81**
4.1 Experimental details . . . 81
4.2 Failure modes analysis . . . 82
4.3 Temperature varying and spectral analysis . . . 84
4.4 Conclusions . . . 87

5 Evidence for avalanche generation in reverse-biased InGaN LEDs **89**
5.1 Introduction . . . 89
5.2 Experimental details . . . 90
5.3 Electrical characterization . . . 90
5.4 Optical characterization . . . 92
5.5 Conclusion . . . 94

6 Gradual degradation of color coded test structures **97**
6.1 Experimental details . . . 97
6.2 Structures A and B: different QWs order . . . 98

6.3 Structures A and C: different Al concentration in EBL 105
6.4 DLTS on Wafer B 112
6.5 Closing remarks 114

7 Conclusions **117**

List of Abbreviations **121**

Bibliography **123**

Abstract

This thesis investigates the reliability of state-of-the-art InGaN LEDs for lighting applications and the impact of the diffusion-related mechanisms on optoelectronic GaN-based wafers, with the aim to identify the physical mechanisms responsible for the premature degradation of those devices. By means of custom experimental setups, developed during the triennial research activity, it is possible to identify the dominant failure modes and degradation mechanisms of GaN LEDs subjected to electrical over-stress (EOS), both in forward and reverse bias, and to correlate specific failures with the epitaxy related weaknesses of state-of-the-art LEDs. In particular, to understand the role of defects in the device degradation, advanced techniques such as Deep-Level Transient Spectroscopy (DLTS) and Deep-Level Optical Spectroscopy (DLOS) are employed.

An extensive analysis aimed to correlate the epitaxial growth parameters (indicated with letters from A to E due to confidentiality agreements) and LEDs electro-static discharge (ESD) robustness in reverse bias is presented. The analysis investigates separately the roles of the epitaxial features on the n- and p-side by means of DC and pulsed characterizations. The results suggest: i) on the n-side, the value of the parameter A is critical in the robustness to ESD events; ii) on the p-side, C is the critical parameter; iii) leakage paths in the structure can act as radiative recombination centers in reverse bias conditions and can be responsible for the failure via junction shorting; iv) nitrogen vacancies may be the physical origin of those defects. The information about the physical mechanisms responsible for degradation are used as a feedback for devices manufacturers, for the improvement of the technological processes.

The analysis of the failure modes trigged by EOS events in forward bias describes the power dissipation as the main cause of damage: according to the amount of power delivered to the chip, due to the strong self-heating, the failure can interest the chip (leading to a short-like failure) or the whole package (inducing an open-like failure). Further experiments allow to identify four different regions before the failure of the device: i) radiative recombination is the dominant recombination process and non-uniform band-filling can be detected, ii) by increasing the current density, strong self-heating can be noticed, and then iii) the saturation of the quantum wells (QWs) induces a strong overflow and may lead to additional power dissipation. Finally, (iv) the extreme high current density induces the current crowding effect, leading to a progressive decay of the optical properties of the device and to the device failure.

Avalanche generation in state-of-the-art high power InGaN LEDs is detected: the ex-

tremely high electric field generated by strong reverse biases triggers band-to-band tunneling, leading to impact ionization. Current-voltage characterizations at cryogenic temperatures detect the shift of IV curves with increasing temperatures, confirming the role of avalanche generation. Further analysis of the electro-luminescence spectral distribution, in this extreme bias conditions, shows that (i) hole and electron pairs generated by the avalanche process recombine radiatively, generating photons, (ii) which are partially re-absorbed in the In-containing layers and n-GaN side and then (iii) re-emitted as internal photoluminescence of the yellow-emitting defects in the n-GaN layer.

Experiments on color coded structures with different QW order and electron blocking layer (EBL) Al content show that i) leakage current increase in reverse and low forward bias conditions is related to diffusion, ii) the optical degradation is not dominated by diffusion but is related to the defects propagation triggered by the energy released by SRH recombination, iii) the optical degradation starts from the p-side and iv) the physical origin of those defects are impurities on the AlGaN/GaN interface or nitrogen vacancies.

Sommario

Questo lavoro di tesi è focalizzato sullo studio dell'affidabilità di dispositivi LED allo stato dell'arte per applicazioni di illuminotecnica e sull'impatto dei meccanismi di diffusione in wafer optoelettronici in nitruro di gallio, con l'obiettivo di identificare i meccanismi fisici responsabili per il degrado prematuro di tali dispositivi. Mediante l'utilizzo di setup sperimentali, sviluppati durante i tre anni di attività di ricerca, è stato possibile identificare i meccanismi di failure e di degrado dominanti in dispositivi LED basati su GaN sottoposti a condizioni di over-stress elettrico (EOS), sia in polarizzazione diretta che inversa, e correlare le specifiche modalità di fallimento con le difettosità epitassiali di LED allo stato dell'arte. In particolare, al fine di appurare il ruolo dei difetti cristallini nel degrado del dispositivo, sono state utilizzate tecniche di caratterizzazione avanzate: il Deep-Level Transient Spectroscopy (DLTS) e il Deep-Level Optical Spectroscopy.

In questa tesi è presentata un'analisi approfondita finalizzata alla correlazione dei parametri di crescita epitassiale (nominati con lettere dalla A alla E poichè coperti da un accordo di non divulgazione) con la robustezza dei dispositivi LED alle scariche elettrostatiche. La trattazione analizza separatamente i ruoli dei parametri epitassiali di lato p ed n, attraverso caratterizzazioni DC e impulsate. I risultati suggeriscono che: i) sul lato n, A è il parametro critico per la robustezza alle scariche elettrostatiche; ii) mentre sul lato p, il parametro critico è C; iii) i percorsi di leakage nella struttura possono fungere da centri di ricombinazione radiativa quando il dispositivo è polarizzato inversamente e possono favorire il fallimento previa corto-circuitazione della giunzione; iv) le vacanze di azoto possono essere la causa fisica delle difettosità epitassiali. Le informazioni relative ai meccanismi fisici di degrado sono state condivise con il produttore dei dispositivi, al fine di promuovere il miglioramento della tecnologia di processo.

L'analisi dei meccanismi di fallimento indotti da EOS in condizioni di polarizzazione diretta indica la dissipazione di potenza come la principale causa di degrado: in base al livello di potenza dissipata nel dispositivo e al conseguente auto-riscaldamento, il fallimento può interessare il chip (portando ad un fallimento come corto-circuito) o l'intero package (portando ad un fallimento di tipo circuito-aperto). Ulteriori esperimenti hanno permesso di identificare quattro regioni di funzionamento, prima del fallimento del dispositivo: i) la ricombinazione di tipo radiativo è dominante ed il riempimento delle buche quantiche non è uniforme, ii) l'incremento della densità di corrente induce un forte auto-riscaldamento, iii) e porta alla

saturazione delle buche quantiche e all'overflow dei portatori. Infine, iv) l'estrema densità di corrente induce l'effetto di current crowding, portando ad un progressivo decadimento delle proprietà ottiche del dispositivo e al successivo fallimento.

La generazione del processo avalanche è identificata in dispositivi LED di potenza: a causa del forte campo elettrico indotto nel dispositivo, sottoposto a polarizzazione inversa, si instaura il processo di tunneling banda a banda dei portatori e la conseguente ionizzazione da impatto. La caratterizzazione elettrica effettuata a temperature criogeniche evidenzia lo spostamento delle curve IV all'incremento della temperatura, confermando la presenza della generazione avalanche. Ulteriori analisi dell'elettroluminescenza e dei suoi diversi contributi spettrali mostrano che: i) le coppie elettrone-lacuna generate dal processo di avalanche ricombinano radiativamente, generando fotoni, ii) i quali sono parzialmente riassorbiti nel lato n della struttura e successivamente iii) riemessi come fotoluminescenza nelle lunghezze d'onda del giallo dai difetti presenti nel cristallo.

Esperimenti su strutture color coded con buche quantiche disposte con diverso ordine nello stack epitassiale e diversa concentrazione di Al all'interno dell'electron blocking layer (EBL) mostrano che i) l'incremento della corrente di leakage in condizioni di polarizzazione inversa e debolmente diretta sono correlate alla diffusione, ii) il degrado ottico non è dominato da tale processo di diffusione, ma è collegato alla propagazione di difetti indotta dall'energia termica rilasciata da ricombinazione di tipo SRH, iii) il degrado ottico ha inizio dal lato p della giunzione e iv) l'origine fisica di tali difetti è rappresentata da impurezze all'interfaccia AlGaN/GaN o vacanze di azoto.

Publications

International journal papers

1. M. Buffolo, M. Meneghini, C. De Santi, H. Felber, N. Renso, G. Meneghesso, and E. Zanoni, "*Experimental observation of TDDB-like behavior in reverse-biased green InGaN LEDs*", Microelectron. Reliab., vol. 64, 2016, DOI:10.1016/J.MICROREL.2016.07.103.

2. N. Renso, M. Meneghini, M. Buffolo, C. De Santi, G. Meneghesso, E. Zanoni, C. De Santi, G. Meneghesso, and E. Zanoni, "*Understanding the degradation processes of GaN based LEDs submitted to extremely high current density*", Microelectron. Reliab., vol. 76–77, no. 2016, 2017, DOI:10.1016/J.MICROREL.2017.06.044.

3. C. De Santi, A. Caria, N. Renso, E. Dogmus, M. Zegaoui, F. Medjdoub, G. Meneghesso, E. Zanoni, and M. Meneghini, "*Evidence of optically induced degradation in gallium nitride optoelectronic devices*", Appl. Phys. Express, vol. 11, no. 11, p. 111002, Nov. 2018, DOI:10.7567/APEX.11.111002.

4. N. Renso, M. Buffolo, C. De Santi, M. Ronzani, G. Meneghesso, E. Zanoni, and M. Meneghini, "*Failure limits and electro-optical characteristics of GaN-based LEDs under electrical overstress*", Microelectron. Reliab., vol. 88–90, pp. 887–890, Sep. 2018, DOI:10.1016/J.MICROREL.2018.06.054.

5. C. De Santi, M. Buffolo, N. Renso, A. Neviani, G. Meneghesso, E. Zanoni, and M. Meneghini, "*Evidence for defect-assisted tunneling and recombination at extremely low current in InGaN/GaN-based LEDs*", Appl. Phys. Express, vol. 12, no. 5, p. 052007, May 2019, DOI:10.7567/1882-0786/AB10E3.

Papers in conference proceedings

1. N. Renso, C. De Santi, P. Dalapati, D. Monti, M. Binder, B. Galler, R. Zeisel, G. Meneghesso, E. Zanoni, and M. Meneghini, "*Evidence for avalanche generation in reverse-biased InGaN LEDs*", in Light-Emitting Devices, Materials, and Applications, 2019, p. 70.

2. C. De Santi, M. Meneghini, N. Renso, M. Buffolo, N. Trivellin, G. Mura, M. Vanzi, A. Migliori, V. Morandi, G. Meneghesso, and E. Zanoni, "*Investigation of the time-dependent failure of InGaN-based LEDs submitted to reverse-bias stress*", in Light-Emitting Diodes: Materials, Devices, and Applications for Solid State Lighting XXI, 2017, vol. 10124, no. February 2017, p. 101240F.

3. C. De Santi, M. Buffolo, N. Renso, G. Meneghesso, E. Zanoni, and M. Meneghini, "*Origin of the low-forward leakage current in InGaN-based LEDs*", in Light-Emitting Devices, Materials, and Applications, 2019, vol. 10940, no. May, p. 18.

4. C. De Santi, M. Meneghini, A. Caria, N. Renso, E. Dogmus, M. Zagaoui, F. Medjdoub, E. Zanoni, and G. Meneghesso, "*Electrically- and Optically-driven Degradation Processes in InGaN-based Photodetectors*", in GaN Marathon 2.0, 2018.

5. C. De Santi, M. Meneghini, A. Caria, N. Renso, E. Dogmus, M. Zegaoui, F. Medjdoub, E. Zanoni, and G. Meneghesso, "Evidence for recombination-induced degradation processes in InGaN-based optoelectronic devices", in Compound Semiconductor Week Proceedings, 2018.

6. N. Renso, C. De Santi, P. Dalapati, D. Monti, M. Binder, B. Galler, R. Zeisel, G. Meneghesso, E. Zanoni, and M. Meneghini, "Demonstration of band-to-band tunneling and avalanche regime in InGaN LEDs", in ICNS-13 Proceedings, 2019.

7. N. Renso, M. Buffolo, C. De Santi, G. Meneghesso, E. Zanoni, and M. Meneghini, "*Demonstration of tunneling and sub-bandgap recombination in InGaN LEDs at extremely low current levels*", in ICNS-13 Proceedings, 2019.

8. E. Zanoni, C. De Santi, N. Trivellin, N. Renso, M. Buffolo, D. Monti, A. Caria, G. Meneghesso, M. Meneghini, F. Piva, G. Meneghesso, and M. Meneghini, "*Challenges for highly-reliable GaN-based LEDs*", in Light-Emitting Devices, Materials, and Applications, 2019, p. 22.

9. C. De Santi, M. Meneghini, A. Caria, N. Renso, E. Dogmus, M. Zegaoui, F. Medjdoub, E. Zanoni, and G. Meneghesso, "*Degradation of InGaN-based optoelectronic devices under electrical and optical stress*", in Proceedings of the 50th Annual Meeting of the Associazione Società Italiana di Elettronica (SIE 2018), 2018.

10. A. Caria, N. Renso, C. De Santi, F. Dalla Torre, G. Meneghesso, E. Zanoni, M. Meneghini, "Dependence of degradation on InGaN quantum well position: a study based on color coded structures", in SPIE Photonics West 2020 (under revision).

Introduction

During the last two decades, the development of optoelectronic devices based on gallium nitride showed a fast evolution. In fact, GaN-based opto-electronics is widely exploited in the modern technology, such as Blu-ray readers, projectors, automotive headlamps and rear-lamps, optical telecommunications, displays, general lighting, biomedical devices for skin treatments and UV-C devices for the water sanitation.

Thanks to the scientific research, light emitting diodes have achieved impressive improvements in quantum efficiency, optical power and reliability. Late 90's devices had a very low quantum efficiency (below 1%), low optical power (42μW at 20mA) [1] and a limited lifetime [2]. Nowadays, external quantum efficiency of blue light emitting diodes (LEDs), needed for white light generation, exceeds 75% [3]. The expected lifetime of modern GaN LEDs exceeds 50000 hours [4, 5] at junction temperatures up to 150°C, allowing solid-state lighting to overcome the traditional light sources, like incandescent and neon lamps, not only in terms of reliability, but also in optical power and energy efficiency. In fact, modern GaN based white LEDs can achieve energy efficiencies higher than 300lm/W [6], widely overcoming incandescent lamps (about 10lm/W) and fluorescent lamps (about 90lm/W) [7]. Moreover, due to its impressive useful lifetime, solid state lighting can be successfully exploited in all the specific environments where maintenance costs and difficulties have a strong impact.

To achieve such high reliability standards, the scientific research played a central role not only in the improvement of the device performance, but also in limiting the impact of those degradation processes that reduce the device useful lifetime. In fact, when a device is working in nominal operating conditions, it can be submitted to current densities above 100A/cm^2 and junction temperature that can exceed 150°C. These extreme conditions may trigger and accelerate several degradation mechanisms that lead to the worsening of the semiconductor chip [8, 9, 10, 11] and, eventually, of the device package [12].

Despite the good properties of these devices, several extrinsic events, like electrical overstress (EOS), can induce permanent damages and, eventually, lead to the catastrophic failure of the device [13]. EOS refers to a condition whereby the device is biased above the absolute maximum electrical value specified by the manufacturer and is commonly characterized by voltages not above several tens of volts and time duration of more than tens of microseconds. Since the EOS is a very broad concept, many are the possible sources, including power-on and power-off transients, inrush and hot plugging currents, latch-up conditions and device over-

driving [14]. The high current/power densities reached during an EOS event may accelerate several degradation mechanisms, thus leading to a premature degradation of the semiconductor material [15, 16], of the ohmic contact [16, 17, 10], of the packaging materials [18, 19] and, in general, to a premature decrease in the optical power of the device over time [18, 19, 9]. For these reasons, it is very important to investigate the degradation processes induced by EOS, which is considered as one of the leading failure mechanisms for LEDs, responsible for more than 40% of the failure events [20, 21].

A particular category of EOS is the electro-static discharge (ESD), which are characterized by voltage pulses of tens of KV that can last tens of nanoseconds [22]. ESD events are typically related to the accumulation of electrostatic charge which can be generated during the processes of manufacturing and packaging and during the handling by operators and machinery [14].

Typically, it is not possible to predict when a device will be submitted to an ESD or EOS event. Then, the understanding of short-term and long-term impacts of those events on the electro-optical performance of LEDs is fundamental to improve the robustness of optoelectronic structures. Several papers [23, 24, 25] revealed the correlation between the semiconductor defect concentration and the ESD robustness. Moreover, some external solutions, such as protection diodes and clamping circuits, have been presented to limit the impact of those events on optoelectronic devices. Despite this, solutions that can be directly implemented inside the semiconductor are missing, especially to limit the impact of EOS events.

Because of the aforementioned motivations, the aim of this work is to investigate the degradation mechanisms that lead to the premature decay of the electro-optical performance of GaN-based LEDs, by means of specific tests and procedures. In particular, this work is structured as follows:

- *Chapter 1: Principles of Light Emitting Diodes* In the first chapter, the theoretical basis and the working principles of light emitting diodes will be presented. Some detail on electrical and optical characteristics of LED structure will be given. The chapter will close with an overview on the main degradation mechanisms that limit the LEDs lifetime.

- *Chapter 2: Advanced characterization techniques* The principles of the most advanced characterization techniques exploited in this work will be presented, like the Deep Level Transient Spectroscopy (DLTS) and Deep Level Optical Spectroscopy (DLOS).

- *Chapter 3: Effects of growth parameters of GaN-based LEDs on the ESD robustness* In this part, a comparison among growth parameters, DC and pulsed characterization results and ESD stability will be presented. The aim of this work is to analyze the degradation processes responsible for the LEDs failure and identify how the different growth parameters impact on the ESD robustness.

- *Chapter 4: Failure limits and electro-optical characteristics of GaN-based LEDs under electrical overstress* This chapter will present the analysis of the degradation mechanisms

and of the electro-optical characteristics of light emitting diodes (LEDs) submitted to electrical overstress in forward bias, published on the scientific journal *Microelectronics Reliability* ([26]). The research will be focused on: a) the dependence of failure current/power on pulse duration, b) the dependence of the electrical characteristics on temperature, and c) the optical characteristics of the devices under overstress conditions.

- *Chapter 5: Evidence for avalanche generation in reverse-biased InGaN LEDs* In this part will be presented the experimental evidence that avalanche generation can take place in state-of-the-art InGaN-based blue LEDs. The current-voltage and electroluminescence curves of the devices in extreme reverse bias conditions will be shown. Numerical simulations will show that in this bias condition the band-to-band tunneling barrier thickness is low, leading to the possible injection of highly-energetic electrons from the p-side to the n-side that can start the avalanche process. The relevant outcomes of this work were presented to the conference *Photonics West 2019* and included in the conference proceedings [27].
- *Chapter 6: Gradual degradation of color coded test structures* In this part, color coded test structures will be exploited to investigate the role of p-side and n-side in the gradual degradation of optical properties. Several structures with different QWs order and Al content in EBL will be compared.
- *Chapter 7: Conclusions* The last chapter will summarize the main outcomes of this three years research activity.

Chapter 1

Principles of Light Emitting Diodes

The *recombination* is a process in which an electron in excited state, such as an electron in the conduction band, releases part of the excess energy, going into a free state at lower energy in the valence band (hole). In a semiconductor, according to the process used by the recombining electron to release its energy, it is possible to define two types of recombination processes: the radiative and non-radiative one. Being only the radiative recombination able to emit photons, the LED design is focused on the maximization of the radiative recombination and the minimization of the non-radiative one.

1.1 Radiative recombination

Under equilibrium conditions, i.e. without external stimuli such as light or current, the law of mass action teaches that the product of the electron and hole concentrations is constant

$$n_0 p_0 = n_i^2 \tag{1.1}$$

where n_0 and p_0 are the electron and hole concentrations at equilibrium and n_i is the intrinsic carrier concentration. An excess of carrier can be generated either by absorption of light or by a current injection. In non-equilibrium conditions, the total carrier concentration can be calculated as the sum of the equilibrium and the excess carrier ones

$$n = n_0 + \Delta n \quad p = p_0 + \Delta p \tag{1.2}$$

where Δn and Δp are the excess electron and hole concentrations, respectively.

Considering a free electron in the conduction band, the probability that such electron recombines with a hole is proportional to the hole concentration, that is, $R \propto p$. The number of recombination events will also be proportional to the concentration of electrons. Thus the recombination rate is proportional to the product of electron and hole concentrations, that is, $R \propto np$. Using a proportionality constant, the *bimolecular recombination rate* per unit time

per unit volume can be defined as

$$R = -\frac{dn}{dt} = -\frac{dp}{dt} = Bnp \tag{1.3}$$

where B is the *bimolecular recombination coefficient*. It has typical values of 10^{-11}–$10^{-9}\text{cm}^3/\text{s}$ for direct III-V semiconductors.

Considering now the recombination dynamics in function of time, since electrons and holes are generated and annihilated in pairs, we can assume that in steady-state conditions their concentrations are equal, then

$$\Delta n(t) = \Delta p(t). \tag{1.4}$$

Employing the 1.2 and 1.3, the recombination rate becomes

$$R = B[n_0 + \Delta n(t)][p_0 + \Delta p(t)] \tag{1.5}$$

1.1.1 Radiative recombination for low-level excitation

In case of *low-level excitation*, the photo-generated carrier concentration is much smaller than the majority carrier concentration, i.e. $\Delta n \ll (n_0+p_0)$. Using the 1.4, the 1.5 can be rewritten as

$$\begin{aligned} R &= Bn_i^2 + B(n_0 + p_0)\Delta n(t) \\ &= R_0 + R_{excess} \end{aligned} \tag{1.6}$$

where the first summand can be identified as the equilibrium recombination rate (R_0) and the second one as the excess recombination rate (R_{excess}). Then, the time-dependent carrier concentration can be calculated from the rate equation

$$\frac{dn(t)}{dt} = G - R = (G_0 + G_{excess}) - (R_0 + R_{excess}) \tag{1.7}$$

where G_0 and R_0 are the equilibrium generation and recombination rates, respectively.

Assuming that the semiconductor has been illuminated with light and at time $t = 0$ the illumination is switched off, since that instant the generation of excess carriers is stopped ($G_{excess} = 0$). The recombination rate can be calculated by insertion of the 1.6 into 1.7 and imposing $G_0 = R_0$, obtaining

$$\frac{d}{dt}\Delta n(t) = -B(n_0 + p_0)\Delta n(t) \ . \tag{1.8}$$

The solution of the differential equation gives

$$\Delta n(t) = \Delta n_0 e^{B(n_0+p_0)t} = \Delta n_0 e^{-t/\tau} \quad \text{where} \quad \Delta n_0 = \Delta n(t=0)\,. \tag{1.9}$$

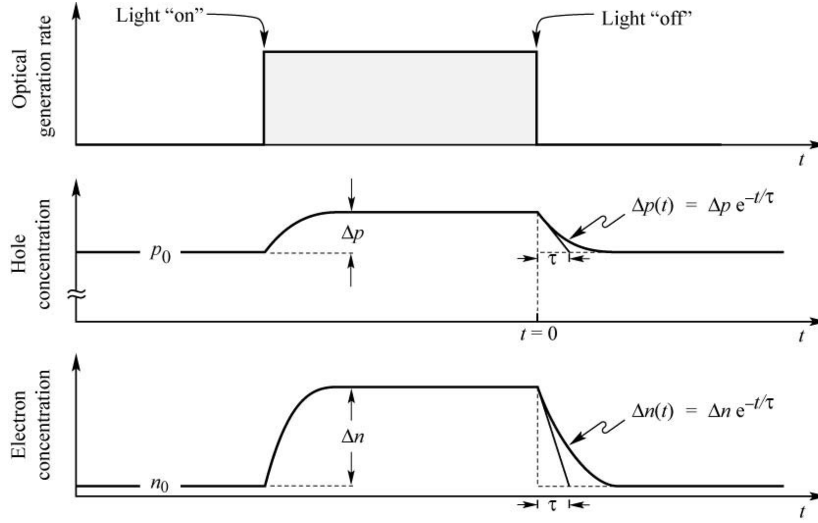

Figure 1.1: Carrier concentration as a function of time before, during, and after an optical excitation pulse. The semiconductor is assumed to be p-type and thus it is $p_0 \gg n_0$. Electrons and holes are generated in pairs, thus $\Delta p = \Delta n$. Under low-level excitation as shown here, it is $\Delta n \ll p_0$ [28].

The carrier lifetime can be identified as

$$\tau = \frac{1}{B(n_0 + p_0)}. \tag{1.10}$$

Being in low-level excitation condition, for a semiconductor with a specific doping type (i.e. p-type), the minority carrier lifetime calculated with the 1.10 can be reduced to the contribute of the majority carrier concentration only ($\tau_n = 1/Bp_0$ in p-type). The figure 1.1 shows the majority and minority carrier concentrations in a p-type semiconductor as a function of time in the case of low-level excitation: photo-generated carrier concentration is much smaller than the majority carrier concentration. At the end of the photo-excitation, the minority carriers concentration decays exponentially with a time constant τ, which is the mean time between generation and recombination events for a minority carrier. Also the majority carriers decay with the same time constant, but only a small fraction of them disappear by recombination. In fact, for low-level excitation, the average time it takes for a majority carrier to recombine is much longer than the minority carrier lifetime. For many practical purposes, the majority carrier lifetime can be assumed to be infinitely long.

1.1.2 Radiative recombination for high-level excitation

In case of *high-level excitation*, the photo-generated carrier concentration is larger than the equilibrium carrier concentration, i.e. $\Delta n \gg (n_0 + p_0)$. The bimolecular rate equation 1.3 can be rewritten as

$$R = \frac{d\Delta n(t)}{dt} = -B\Delta n^2\,. \tag{1.11}$$

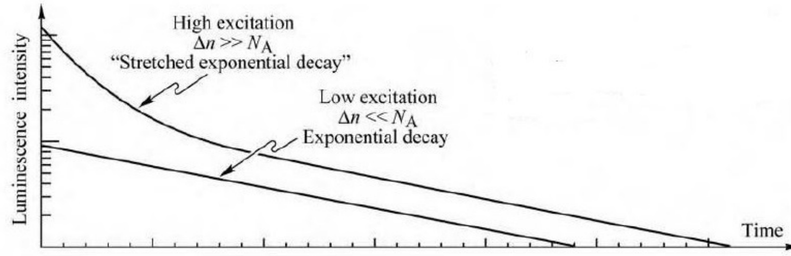

Figure 1.2: Luminescence decay for low and high excitation densities. [28]

Solving this differential equation, using $\Delta n(0) = \Delta n_0$, gives

$$\Delta n(t) = \frac{1}{Bt + \Delta n_0^{-1}} . \tag{1.12}$$

In this case, the solution presents a non-exponential decay. For this reason, the time constant τ for the carries concentration decay is calculated as the slope of the decay by using the following equation

$$\tau(t) = -\frac{\Delta n(t)}{\frac{d\Delta n(t)}{dt}} \tag{1.13}$$

which yields to

$$\tau(t) = t + \frac{1}{B\Delta n_0} . \tag{1.14}$$

Thus, for non-exponential decays, the time constant depends on time. Equation 1.14 shows that the minority carrier lifetime increases with time. For sufficiently long times, low-level excitation conditions will be reached and τ will approach the low-level value.

1.1.3 Luminescence decay

Since the luminescence intensity is proportional to the recombination rate, the carrier decay in semiconductors can be measured by the decay of the luminescence after a short optical excitation pulse. Calculating the recombination rate for the low and high excitation cases, one obtains

$$R = -\frac{dn(t)}{dt} = \frac{\Delta n_0}{\tau} e^{-t/\tau} \quad \text{for low excitation} \tag{1.15}$$

and

$$R = -\frac{dn(t)}{dt} = \frac{B}{(Bt + \Delta n_0^{-1})^2} \quad \text{for high excitation.} \tag{1.16}$$

In the latter case, the decay is non-exponential. All non-exponential decay functions can be expressed by an exponential function with a time-dependent time constant, i.e. $\exp[-t/\tau(t)]$. In most cases, the time constant τ increases with time. This type of decay function is frequently called a stretched exponential decay function which describes a slower-than-exponential decay. A graphical description of the optical decay can be observed in figure 1.2.

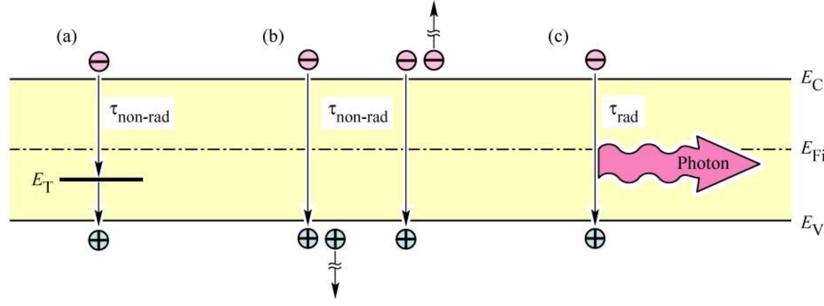

Figure 1.3: Band diagram illustrating recombination: (a) non-radiative recombination via deep level, (b) non-radiative recombination via Auger process and (c) radiative. [28]

1.2 Non-radiative recombination

During non-radiative recombination, the electron energy is converted to vibrational energy of lattice atoms, i.e. phonons. Thus, the electron energy is converted to heat. There are several physical mechanisms by which non-radiative recombination can occur. Defects in the crystal structure are the most common cause for non-radiative recombination. These defects include unwanted foreign atoms, native defects, dislocations, and any complexes of defects, foreign atoms, or dislocations [29]. All such defects have energy level structures that are different from substitutional semiconductor atoms. It is quite common for such defects to form one or several energy levels within the forbidden gap of the semiconductor. Energy levels within the gap of the semiconductor are efficient recombination centers; in particular, if the energy level is close to the middle of the gap. The recombination of carriers via a trap level is shown schematically in figure 1.3.

A first study on recombination of free carriers via deep levels was performed by Shockley, Read and Hall in 1952 [30, 31]. The non-radiative recombination rate via deep levels with energy level E_T and concentration N_T is given by

$$R_{SRH} = \frac{p_0\Delta n + n_0\Delta p + \Delta n\Delta p}{(N_T\nu_p\sigma_p)^{-1}(n_0 + n_1 + \Delta n) + (N_T\nu_n\sigma_n)^{-1}(p_0 + p_1 + \Delta p)} \tag{1.17}$$

where $\Delta n = \Delta p$; ν_n and ν_p are the electron and hole thermal velocities, respectively, and σ_n and σ_p are capture cross section of the traps. Parameters n_1 and p_1 are electron and hole concentrations in case the Fermi level is located at the trap level; these two are:

$$n_1 = n_i \exp\left(\frac{E_T - E_{Fi}}{kT}\right) \quad \text{and} \quad p_1 = n_i \exp\left(\frac{E_{Fi} - E_T}{kT}\right) \tag{1.18}$$

where E_{Fi} is the Fermi level in the intrinsic semiconductor. The non-radiative lifetime of excess electrons can be deduced from the equation 1.17, knowing that $R_{SRH} = \Delta n/\tau$. As a consequence, the life-time is given by:

$$\frac{1}{\tau} = \frac{p_0 + n_0 + \Delta n}{(N_T\nu_p\sigma_p)^{-1}(n_0 + n_1 + \Delta n) + (N_T\nu_n\sigma_n)^{-1}(p_0 + p_1 + \Delta p)} \tag{1.19}$$

Assuming that the semiconductor is p-type, majority carriers will be holes, i.e. $p_0 \gg n_0$ and $p_0 \gg p_1$, and a small deviation from equilibrium, i.e. $\Delta n \ll p_0$, the minority carrier lifetime is

$$\frac{1}{\tau} = \frac{1}{\tau_{n_0}} = N_T \nu_n \sigma_n \tag{1.20}$$

Instead, if electrons were majority carriers, that means the semiconductor is n-type, then we would obtain:

$$\frac{1}{\tau} = \frac{1}{\tau_{p_0}} = N_T \nu_p \sigma_p \tag{1.21}$$

From the previous equations, we can deduce that the SRH recombination rate is limited by the minority carrier capture rate; in fact, the capture of majority carriers is a more likely event with respect to the capture of minority carriers. Equation 1.19 becomes:

$$\frac{1}{\tau} = \frac{p_0 + n_0 + \Delta n}{\tau_{p_0}(n_0 + n_1 + \Delta n) + \tau_{n_0}(p_0 + p_1 + \Delta p)} \tag{1.22}$$

Assuming that $\nu_n \sigma_n = \nu_p \sigma_p$, $\tau_{n_0} = \tau_{p_0}$ and remembering that $\Delta n \ll p_0$, we obtain:

$$\tau = \tau_{n_0}\left(1 + \frac{p_0 + p_1}{p_0 + n_0}\right) \tag{1.23}$$

Considering a further simplification, that is the case of an intrinsic material $n_0 = p_0 = n_i$, equation 1.23 simplifies to:

$$\tau_i = \tau_{n_0}\left(1 + \frac{p_1 + n_1}{2n_i}\right) = \tau_{n_0}\left[1 + \cosh\left(\frac{E_T - E_{Fi}}{kT}\right)\right] \tag{1.24}$$

From equation 1.24 we can deduce that, since the *cosh* function has a minimum when its argument is equal to zero, that in our case is when $E_T = E_{Fi}$, the non-radiative lifetime is minimized when the trap level is near the center of the band gap, and in this case the lifetime is given by $\tau = 2\tau_{n_0}$.

Inspection of equation 1.24 also reveals a temperature T dependence of the non-radiative recombination lifetime, more precisely as T increases the non-radiative recombination lifetime decreases. This implies that, at higher temperature the radiative band-to-band recombination efficiency decreases.

1.2.1 Auger recombination

Another important non-radiative recombination mechanism is Auger recombination. In this type of process, the excess energy due to the electron-hole pair recombination is dissipated through the excitation of a free electron in the conduction band, or a hole in the valence band. This process is reported in Figure 1.3b. The excited carrier will lose its energy by multiple phonon emission, until it will reach the edge of the band. The recombination rates associated

to the Auger process are:

$$R_{Auger} = C_p n p^2 \tag{1.25}$$

in the case of energy given to a hole in valence band (this process is more likely to happen in p-type semiconductors), while:

$$R_{Auger} = C_n n^2 p \tag{1.26}$$

in the case of energy given to an electron in the conduction band (process more likely to happen in n-type semiconductors). From these two equation we can evince that Auger recombination is proportional to the square of the carrier concentration, since we need two carriers of the same type during the process. In general, coefficients C_n and C_p are different due to the different structure of the conduction band and of the valence band.

In high-excitation condition, where the photogenerated carrier concentration is higher than the one of carriers at equilibrium, the two previous equations reduce to:

$$R_{Auger} = (C_p + C_n)n^3 = Cn^3 \tag{1.27}$$

where C is defined as Auger coefficient, and presents typical values around 10^{-28} - 10^{-29} cm^6/s for III-V semiconductors.

Auger recombination reduces the luminescence efficiency in semiconductor only at high excitation intensity or at high injection currents, thus for high carrier concentrations, due to the cubic carrier concentration dependence. At lower carrier concentrations, the Auger recombination rate can be neglected.

1.2.2 Non-radiative recombination at surfaces

Non-radiative recombination can occur also at semiconductor surfaces, that introduce strong perturbation in the periodicity of a crystal lattice. Since the band diagram model is based on the latter, it will need to be modified at the semiconductor surface. This modification includes the addition of electronic states within the band gap of the semiconductor. From a chemical point of view, atoms at the surface cannot have the same bonding structure like the atoms in the bulk due to the lack of neighboring atoms. For this reason, some of the valence orbitals do not form chemical bonds, giving origin to the so-called dangling bonds, partially filled electron orbitals that introduce electronic states within the band gap and act as recombination centers. These states can be as acceptor-like or donor-like states, depending on the charge state of these valence orbitals. It is possible that some of these dangling bonds rearrange themselves and form bonds between neighboring atoms in the same surface plane and cause the formation of new atomic structures with different energy states with respect to those in the bulk. It is difficult to predict the energetic localization of surface states, even with

powerful theoretical models, thus usually phenomenological models of surface recombination are used.

Considering a p-type semiconductor subjected to illumination, it is possible to calculate the effect of surface recombination on the carrier distribution. Assuming a uniform generation rate G, the continuity equation for electrons is given by:

$$\frac{\partial n(x,t)}{\partial t} = G - R + \frac{1}{q}\frac{\partial J_n}{\partial x} \tag{1.28}$$

where J_n is the current density due to the electrons flowing to the surface. In the bulk there is no dependence on space, thus the continuity equation reduces to $G = R$ under steady-state conditions. Since the semiconductor is p-type, the recombination rate is given by:

$$R = -\frac{d\Delta n(t)}{dt} = \frac{\Delta n(x,t)}{\tau_n} \tag{1.29}$$

The excess carrier concentration in the bulk is given by $\Delta n_\infty = G\tau_n$. Moreover, assuming that the current density J_n is a diffusion current density with this form:

$$J_n = qD_n\frac{\partial \Delta n(x,t)}{\partial x} \tag{1.30}$$

and using this in equation 1.28, the continuity equation becomes:

$$\frac{\partial \Delta n(x,t)}{\partial t} = G - \frac{\Delta n(x,t)}{\tau_n} + D_n\frac{\partial^2 \Delta n(x,t)}{\partial x^2} \tag{1.31}$$

At the semiconductor surface, the boundary condition is given by:

$$J_n\big|_{x=0} = qD_n\frac{\partial \Delta n(x,t)}{\partial x}\bigg|_{x=0} = qS\Delta n(x,t)\big|_{x=0} \tag{1.32}$$

where S is the surface recombination velocity (cm/s). This equation shows that carriers recombine rapidly at the surface with velocity equal to S. Finally, assuming a time constant generation rate G, thus the minority carrier concentration has no time dependence, we can find the steady state solution to the continuity equation:

$$n(x) = n_0 + \Delta n(x) = n_0 + \Delta n_\infty\left[1 - \frac{\tau - NS\exp(-x/L_n)}{L_n + \tau_n S}\right] \tag{1.33}$$

where $L_n = \sqrt{D_n\tau_n}$ is the diffusion length of the minority carriers in the semiconductor, that in our case are electrons. Figure 1.4 shows the band diagram and the majority and minority carrier concentrations next to the surface for a p-type semiconductor. For $S \to 0$, the minority carrier concentration at the surface is equal to the bulk value, i.e. $n(0) \to n_0 + \Delta n_\infty$, while for $S \to \infty$ the minority carrier concentration at the surface tends to decrease, approaching the value at equilibrium, $n(0) \to n_0$. Typical value for S in GaN is $5 \cdot 10^4$ cm/s.

Surface recombination causes undesired effects, like the luminescence efficiency reduction and the surface heating. In order to have this process, both carriers are needed. In the realiza-

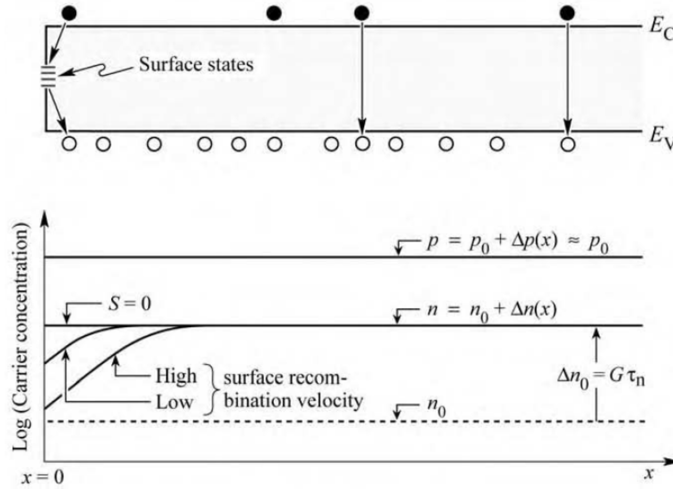

Figure 1.4: Band diagram (top) and minority and majority carrier concentrations near the surface (bottom) assuming uniform carrier generation due to illumination. The excess carrier concentrations are Δn and Δp. [28]

tion of these devices, it is important that the active region, where both carriers are present, be far removed from any surface. Different passivation techniques have been developed in order to reduce this non-radiative recombination mechanism, like treatments with sulfur and other chemicals.

1.3 Internal quantum efficiency

In the previous sections, different non-radiative recombination mechanisms have been presented; though this process can be reduced with different techniques, it is not possible to completely eliminate it. We can define internal quantum efficiency (IQE) the ratio between the number of emitted photons inside the semiconductor and the number of carriers undergoing recombination, that means the probability to have radiative recombination; this efficiency allows us to evaluate the impact of the non-radiative recombination on the radiative one. In order to calculate it, we define τ_r as the radiative lifetime, and τ_{nr} as the non-radiative lifetime. Thus, the total probability of recombination is given by the sum of these two probabilities:

$$\tau^{-1} = \tau_r^{-1} + \tau_{nr}^{-1} \tag{1.34}$$

The internal quantum efficiency is given by:

$$\eta_{IQE} = \frac{\tau_r^{-1}}{\tau_r^{-1} + +\tau_{nr}^{-1}} \tag{1.35}$$

Not all photons emitted internally are able to escape from the semiconductor due to reflection problems and re-absorption mechanisms in the substrate.

In the next section, the electrical properties of LEDs will be presented, in order to better

understand the mechanisms that cause the reduction of the efficiency in these devices.

1.4 Electrical properties of LEDs

The basic structure of an LED is the p-n junction. In this section we will explain the principal optical properties of a diode, analyzing the structure and the current-voltage (IV) characteristic, considering also the non ideal case.

1.4.1 p-n junction

The p-n junction is one of the most important junctions in solid state electronic. It is made by two semiconductors, one of p-type and the other one of n-type, put together. Then, a metal contact is put on both the two semiconductors in order to have the anode and the cathode.

Let's consider an abrupt p-n junction, that means the transition from the n-type material to the p-type material is abrupt, obtained by a step variation in the doping at the junction sides. The donor concentration is N_D and the acceptor concentration is N_A. All dopants are assumed to be fully ionized, thus the free electron concentration is $n = N_D$, while the free hole concentration is $p = N_A$. Finally, is assumed that no compensation of the dopants occurs by unintentional impurities and defects.

The big difference in the electron concentration in the two materials causes the electrons diffusion from the n-side to the p-side and the holes diffusion from the p-side to the n-side. Moving to the material with the opposite doping, carriers leave behind them doping atoms that are not compensated, near the junction, giving birth to the depletion of electrons in this region. This last region is called depletion region. Without electrons in the depletion region, the only present charge is given by ionized acceptor and donor. In this region it is assumed that the semiconductor can be divided in two distinct zone, one on the n-side where donors dispose, the other one on the p-side, where acceptor dispose, like Figure 1.5 reports.

An electric field is associated to the depletion region, called built-in, that creates a potential barrier between the two materials. At equilibrium, the electric field amplitude is such that the electrons trend to diffuse from the n-side to the p-side is balanced from the drift trend of the electrons in the opposite direction under the electric field influence. The built-in electric field generates a voltage defined as built-in voltage, that is given by:

$$V_{BI} = \frac{kT}{q} \ln \frac{N_A N_D}{n_i^2} \tag{1.36}$$

This voltage represents the barrier that the free carriers need to pass in order to reach the neutral region with the opposite conductivity. Figure 1.6(a) reports the band diagram of a p-n junction under zero bias and shows the built-in voltage.

From the built-in voltage, it is possible to extrapolate the width of the depletion region: in fact, these two quantities, together with the charge in the depletion region, are bound together by the Poisson equation. The width of the depletion region is:

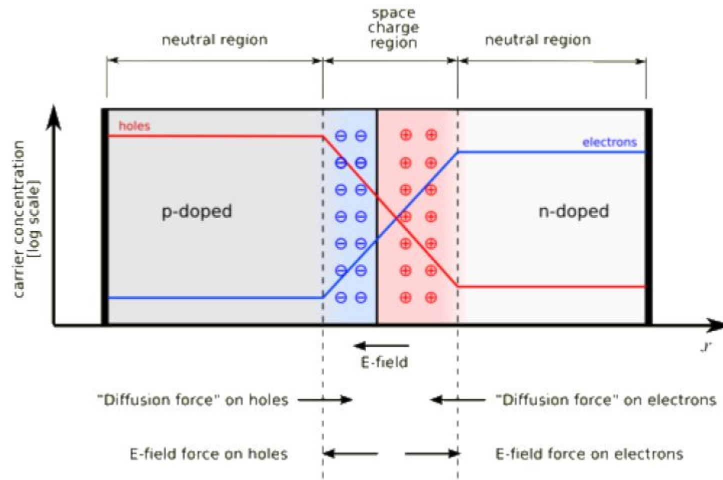

Figure 1.5: p-n junction, where the depletion region is shown. [28]

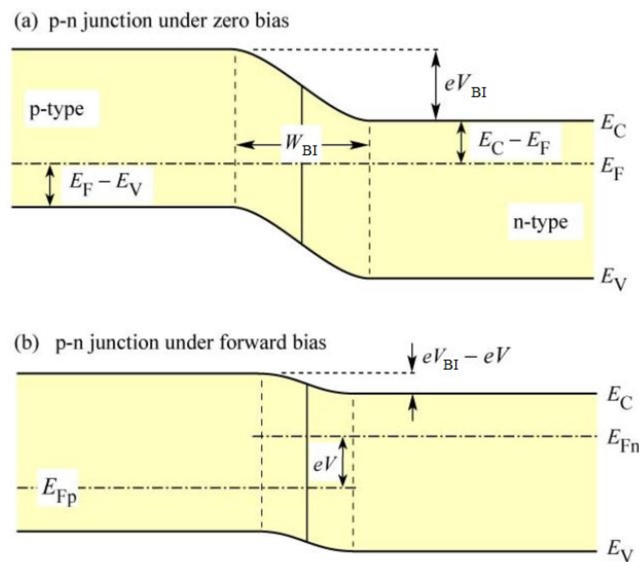

Figure 1.6: Band diagram of a p-n junction under zero bias (a) and under forward bias (b). Under forward bias conditions, minority carriers diffuse into the neutral regions where they recombine. [28]

$$W_D = \sqrt{\frac{2\varepsilon}{q}\left(\frac{1}{N_A} + \frac{1}{N_D}\right)(V_{BI} - V)} \tag{1.37}$$

where $\varepsilon = \varepsilon_r \varepsilon_0$ is the dielectric permittivity of the semiconductor and V is the diode polarization voltage.

In general, two types of currents flow through the diode and these are the drift current and the diffusion current of the electrons and holes. When no voltage is applied, these two currents eliminate each other. In fact, considering as an example the hole current density:

$$J_p(x) = q\left[\mu_p p(x)E(x) - D_p \frac{dp(x)}{dx}\right] = 0 \tag{1.38}$$

where the first term represents the hole drift current, $J_{p_{drift}} = q\mu_p p(x)E(x)$, due to the electric field, instead the second term is the diffusion current, $J_{p_{diff}} = qD_p \frac{dp(x)}{dx}$, due to the hole concentration gradient in the p-type region. Similar considerations can be done for electrons.

If a voltage is applied to the p-n junction, it is possible to observe a potential drop on the depletion region. This region is highly resistive, since it is depleted of free carriers, and for this reason the voltage drop will be entirely on this region. If an external reverse bias voltage is applied, this will cause an increase in the potential barrier, blocking the carrier injection. Instead, applying an external forward voltage (Figure 1.6(b)), the potential barrier will decrease, promoting the carrier injection and causing an increase in the total current. Carriers diffusing in region with opposite type of conductivity will recombine giving place to a photon emission.

1.4.2 I-V characteristic

The first who studied I-V characteristic of a p-n junction was Shockley, from which it derives the equation that describes the diode I-V curve, that is the Shockley equation:

$$I = I_S(e^{qV/kT} - 1) \tag{1.39}$$

where I_S is defined as saturation current

$$I_S = qA\left(\sqrt{\frac{D_p}{\tau_p}}\frac{n_i^2}{N_D} + \sqrt{\frac{D_n}{\tau_n}}\frac{n_i^2}{N_A}\right) \tag{1.40}$$

A is the diode area, while $D_{n,p}$ and $\tau_{n,p}$ are the diffusion constants and minority carrier lifetimes of electrons and holes, respectively. Equation 1.39 can be rewritten:

$$I = qA\left(\sqrt{\frac{D_p}{\tau_p}}\frac{n_i^2}{N_D} + \sqrt{\frac{D_n}{\tau_n}}\frac{n_i^2}{N_A}\right)(e^{qV/kT} - 1) \tag{1.41}$$

Under typical forward bias conditions, where the applied voltage is $V \gg kT/q$ in order to have $[\exp(qV/kT) - 1] \approx \exp(qV/kT)$, equation 1.41 becomes:

$$I = qA\left(\sqrt{\frac{D_p}{\tau_p}}N_A + \sqrt{\frac{D_n}{\tau_n}}N_D\right)e^{q(V-V_{BI})/kT} \tag{1.42}$$

From equation 1.42 we can notice that current increases significantly when the diode voltage is close to the value of the diffusion current, and for this reason it is defined as threshold voltage $V_{th} \approx V_B I$.

Considering the band diagram of the p-n junction under forward bias (Figure 1.6(b)), it is evident the separation of the Fermi level from the conduction and valence band. For this reason, the following sum of energies is zero:

$$qV_{BI} - E_g + (E_F - E_V) + (E_C - E_F) = 0 \tag{1.43}$$

In heavily doped semiconductor this separation is very small with respect to the energy gap and for this reason equation 1.43 becomes:

$$V_{th} \approx V_{BI} \approx \frac{E_g}{q} \tag{1.44}$$

that is an approximate value of the threshold voltage.

Figure 1.7 reports the forward voltage at a current of 20 mA as function of the energy gap for LEDs with different emission wavelength, in the range from the ultraviolet to the infrared. The solid line represents the expected forward diode voltage. Analyzing the figure, it is possible to observe that LEDs based on III-V nitrides do not follow the line. This is caused by different factors: (i) nitride material system presents large band gap discontinuities, which causes an additional voltage drop; (ii) the contact technology is not yet completely mature in nitride-based structures, which causes an additional voltage drop at the ohmic contacts; (iii) the low p-type conductivity in bulk GaN; (iv) it is possible that a negative parasitic voltage drop occurs in the n-type buffer layer.

1.4.3 Non ideality in the I-V characteristic

The Shockley equation gives us the first theoretical I-V characteristic for a p-n junction, but in order to describe the experimentally measured characteristics, the equation becomes:

$$I = I_S e^{qV/(\eta_{ideal} kT)} \tag{1.45}$$

where η_{ideal} is the ideality factor of the diode. For an ideal diode this factor is equal to 1, but for a real diode η_{ideal} can assume values between 1.1 - 1.5, though higher values have been found for III-V arsenide and phosphide diodes (2.0) and for GaN/InGaN diodes (7.0).

Another unwanted effect in a real diode is the presence of parasitic resistances, in particular the series resistance and the parallel resistance. The first one could be ascribed to an excessive contact resistance or the resistance of the neutral regions, instead, the second one can be caused by any parasitic channel through the p-n junction. This last condition can be ascribed

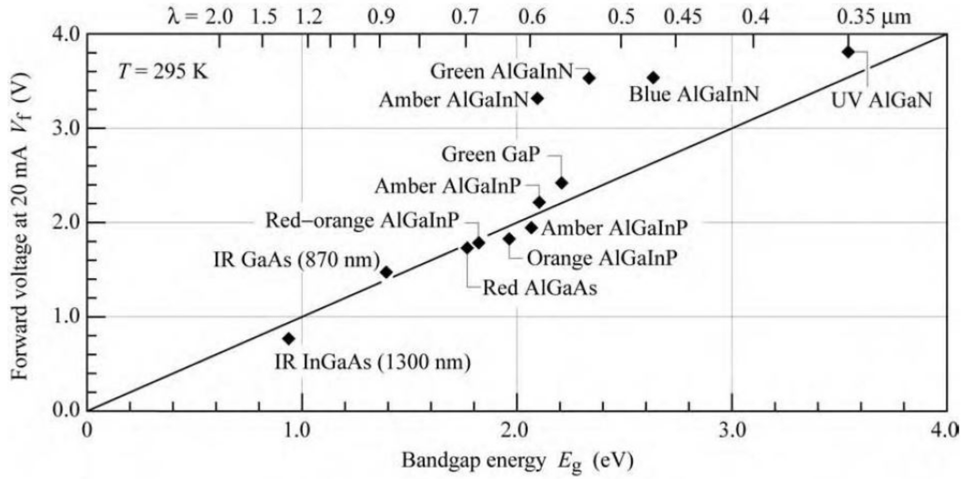

Figure 1.7: Diode forward voltage as function of energy gap for LEDs made by different materials. [28]

to the degradation of the p-n junction or to the generation of surface defects. Figure 1.8 reports the effects on the I-V characteristic due to these parasitic resistances. In order to take in account these, it is necessary to modify the Shockley equation.

Assuming to have a shunt resistance R_P, parallel to the ideal diode, and a series resistance R_S, in series with the ideal diode and R_P, the relation between the current and the voltage becomes:

$$I - \frac{(V - IR_S)}{R_P} = I_S e^{q(V-IR_S)/(\eta_{ideal}kT)} \tag{1.46}$$

There are further deviations of the I-V curve from the ideal conditions, that are not taken into account in equation 1.46. One of this is the abrupt turn-on of the diode, referred as sub-threshold turn-on or premature turn-on: in some conditions, the diode turn-on voltage is distributed over a voltage range instead of having a precise value. In this way, a sub-threshold current is observed before the hypothetic turn-on voltage. This current can be caused by carrier transport through surface states or deep levels in the bulk of the semiconductor.

Carrier generation and recombination in the depletion region are two other important events that can occur in real diodes, due to the presence of trap levels in this region (Figure 1.9). This implies an increase in the current when a forward and a reversed voltage is applied. The recombination current dominates at low voltages and an ideality factor of 2.0 is associated to this current, instead the diffusion current dominates at high voltages and presents an ideality factor equal to 1.0. From Figure 1.10, we can distinguish three main region in the I-V characteristic, from these the two regions related to the generation and recombination current.

When a reverse bias is applied, current is dominated by carrier generation in the depletion region; this current increases if a higher reverse voltage is applied, due to the increase in the

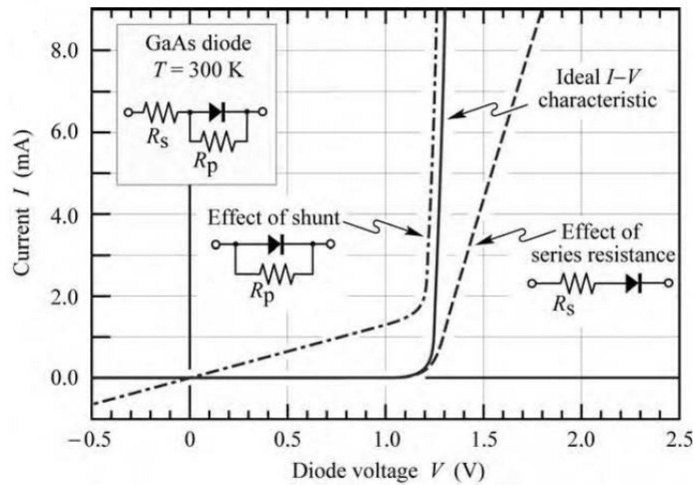

Figure 1.8: Effect of series and parallel resistance on the I-V characteristic.[28]

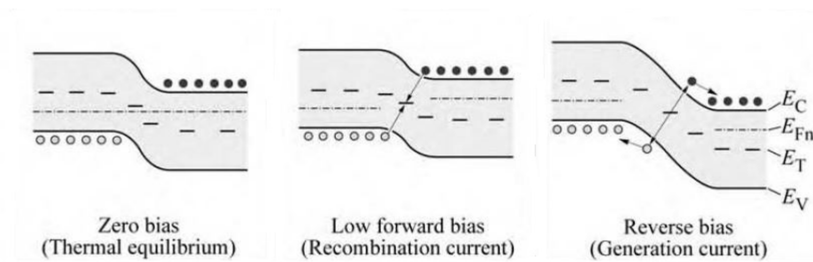

Figure 1.9: Effect of carrier generation and recombination in the depletion region. [28]

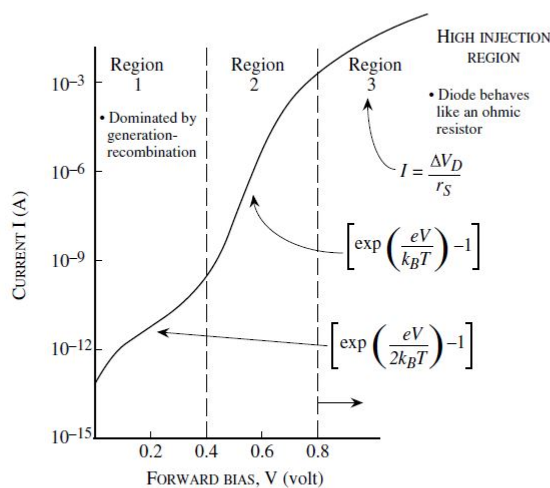

Figure 1.10: Diode current in forward voltage. The generation current dominates in the first region, the diffusion current dominates in the second, instead in the third region the current presents a resistive behavior [32].

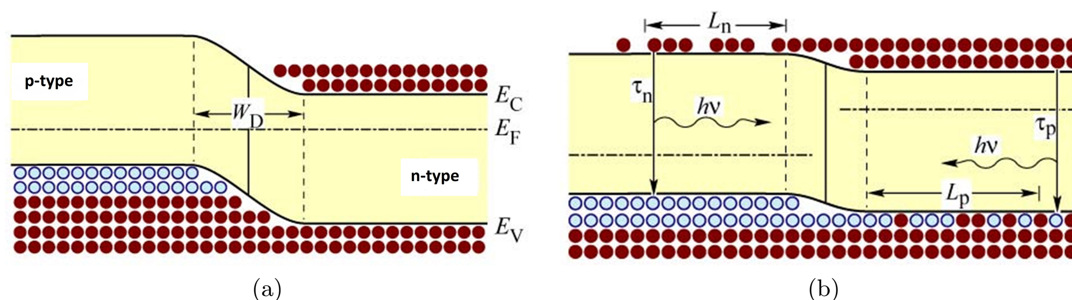

(a) (b)

Figure 1.11: Carrier distribution in a p-n homojunction under zero bias (a) and forward bias (b). [28]

depletion region width.

I-V measurements are carried out in the dark, since light may generate photo-current in the diode. There should be no photo-current in dark conditions, but a very small value is always measured (such 10^{-12} A), due to the limited accuracy of the instruments.

1.4.4 Carrier distribution in homojunction and heterojunction

Until now, p-n homojunction were considered, that means p-n junctions consisting of a single material. In this p-n junctions, the carrier distribution depends on the diffusion constant of carriers, that can be inferred from the mobility thanks to the Einstein relation, which, for a non-degenerate semiconductor is given by:

$$D_n = \frac{kT}{q}\mu_n \quad \text{and} \quad D_p = \frac{kT}{q}\mu_p \tag{1.47}$$

Carriers injected into a semiconductor, with no external electric field applied, propagate by diffusion. Carriers will pass through the depletion region and will reach the region with opposite conductivity where they will eventually recombine. The mean distance a minority carrier diffuses before recombination is the diffusion length. Diffusion lengths for electrons and holes are

$$L_n = \sqrt{D_n \tau_n} \quad \text{and} \quad L_p = \sqrt{D_p \tau_p} \tag{1.48}$$

where τ_n and τ_p are the electron and hole lifetimes, respectively. In typical semiconductors, the diffusion length is in the order of several micrometers, since the minority carriers are distributed in a region several micrometers thick. In Figure 1.11 the carrier distribution in a p-n junction under zero bias (1.11a) and forward bias (1.11b) is shown. Minority carriers are distributed over a large distance, thus recombination occurs over a large region and this is not beneficial for an efficient recombination.

The typical structure used in order to realized high-intensity LEDs is the heterojunction. In these devices two type of semiconductor are used, one with a small bandgap, that will be the active region, and another one with a large bandgap, that will be the barrier region.

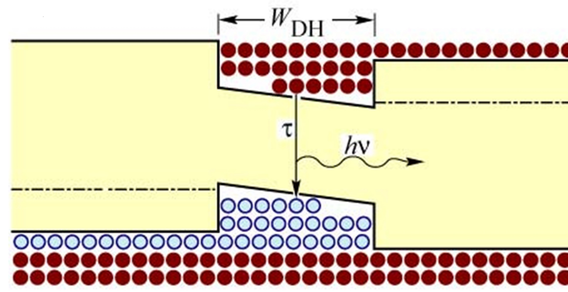

Figure 1.12: Carrier distribution in a double heterojunction under forward bias. [28]

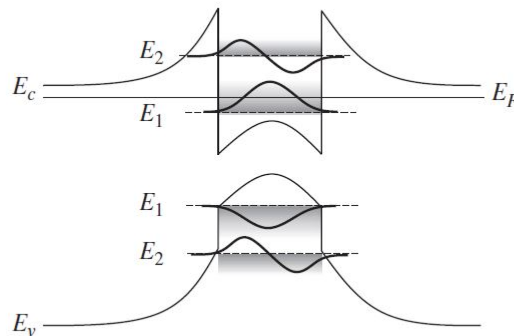

Figure 1.13: Quantized energy level in a quantum well, where the carrier wave functions are shown. [28]

It is possible to realize a structure with two barriers, i.e. an active region enclosed between two large-bandgap semiconductors: in this case the structure is called double heterojunction. Figure 1.12 reports the band diagram of a double heterojunction and its carrier distribution: in this case, the injected carriers are confined within the active region by the barriers. The active region will define the thickness of the region in which carriers recombine, rather than the diffusion length. Usually the length of the active region is smaller than the diffusion length, and this allows an increase in the carrier concentration with respect to the homojunction case. Moreover, since the radiative recombination rate is given by $R = Bnp$, having a high carrier concentration in the active region allows an increase in the radiative recombination rate.

1.4.5 Heterojunctions characteristics

Using heterojunction in order to realize LEDs allows to better improve the performances of these devices, thanks to the carrier confinement in the active region and avoiding the minority carrier diffusion on long distances. The double heterojunction introduces a potential well where carriers are trapped and, if the well is narrow, the allowed energy levels within it are quantized. The structure is called quantum well (QW) (Figure 1.13).

Carriers behavior in QWs is described by Schrödinger equation, whose solution allows to evaluate the energy levels and the sub-bands, giving the potential profile of the well. Despite the heterostructures contribute to the improvement of the LEDs efficiency, however, there

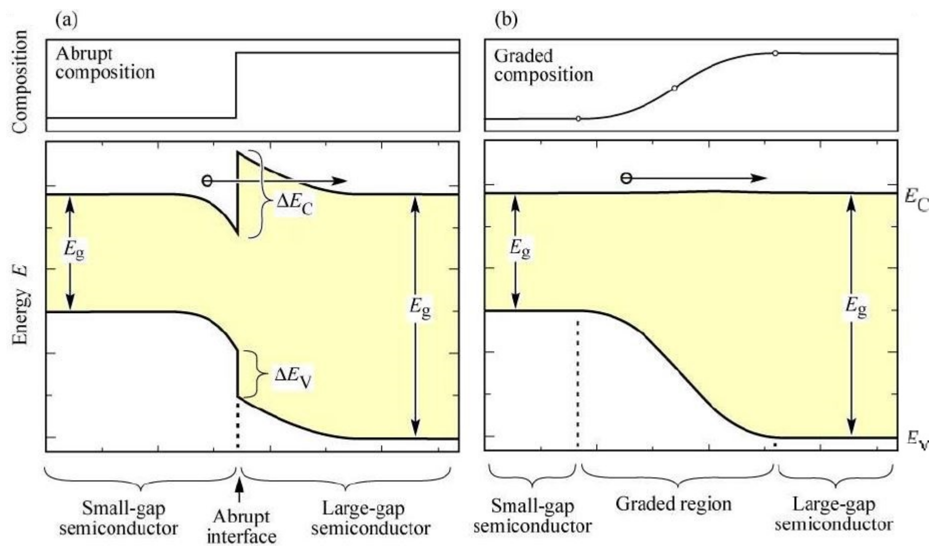

Figure 1.14: Band diagram of an abrupt heterojunction (a) and a graded one (b) of two n-type semiconductors with different bandgap energy. [28]

are still several problems. In the following sections, the main mechanisms that contribute to reducing efficiency and the possible structure optimizations to limit these loss mechanisms are reported.

Effect of heterojunctions on device resistance

As already mentioned before, the employment of heterostructures allows to improve the efficiency of LEDs by confining carriers to the active region. On the other hand, heterojunctions introduce series resistance at the heterostructure interface. In fact, considering a heterostructure made by two semiconductors with different band-gap and assuming both of type n, there will be the diffusion of carriers from the large-bandgap material to the small-bandgap material. As a result of this transfer, an electrostatic dipole will be formed, followed by a band bending, as Figure 1.14(a) shows. Carriers transferring from one semiconductor to the other must overcome this barrier by either tunneling or by thermal emission over the barrier. The thermal power generated from this resistance leads to a reduction in the radiative efficiency, since it causes the heating of the active region.

This kind of issue is obtained when the passage from a material to another is abrupt. To mitigate this effect, graded heterojunctons were introduced, changing the chemical composition of the semiconductor in the proximity of the interface, as shown in Figure 1.14(b). It has been shown that, the shape of the graded region should be parabolic: in this way, the large-bandgap material will be depleted of free carriers due to electron transfer to the small-bandgap material, for this reason the carrier concentration in the first material will be equal to the donor concentration N_D. Assuming that this concentration is constant, the electrostatic potential is:

$$\Phi = \frac{qN_D}{2\varepsilon}x^2 \tag{1.49}$$

The equation shows that the potential depends on the position x with a parabolic shape. In order to compensate for the parabolic shape of the depletion potential, the composition of the semiconductor is varied parabolically as well, so that an overall flat potential results, assuming that the bandgap energy depends linearly on the chemical composition. An approximate design rule for the grading of a heterostructure is given by:

$$x_d = \sqrt{\frac{2\varepsilon\Delta E_C}{q^2N_D}} \tag{1.50}$$

where x_d is the depletion region thickness in the large-bandgap semiconductor and ΔE_C is the discontinuity of the conduction band of the abrupt heterojunction. The heterostructure interface should be graded over the distance x_d in order to minimize the resistance at the interface.

Carrier escape

In an ideal LED, the injected carriers should be confined within the active region thanks to the presence of the lateral barriers. The energy barriers are usually in the order of several hundred meV, i.e. much larger than kT. Despite this, some carriers will be able to escape from the QW, moving in the barrier regions. In fact, free carriers in the active region are distributed according to the Fermi-Dirac distribution, thus some carriers could have higher energy than the height of the confining barrier. This mechanism is shown in Figure 1.15. This carrier escape causes the recombination in the barrier regions, reducing the radiative recombination. The concentration of electrons with energy higher than the barriers is given by:

$$n_B = \int_{E_B}^{\infty} \rho_{DOS} f_{FD}(E)dE \tag{1.51}$$

where ρ_{DOS} is the state density, f_{FD} is the Fermi-Dirac distribution function, and E_B is the height of the barrier.

The electron loss over the barrier generates a leakage current that depends on the carrier concentration at the edge of the barrier. This leakage increases exponentially with the temperature, causing a decrease of the radiative efficiency.

Carrier overflow

Carrier overflow is another loss mechanism, that occurs at high injection current densities. In this way, the carrier concentration in the active region increses followed by an increase in the Fermi level; the latter will rise to the top of the barrier and when it will be within the conduction band, the semiconductor will be in degeneration condition (Figure 1.16). At this

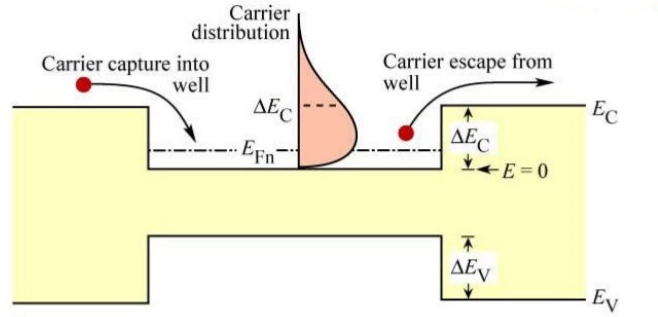

Figure 1.15: Capture and escape of one carrier in a double heterojunction. The figure shows also the carrier distribution in the active region. [28]

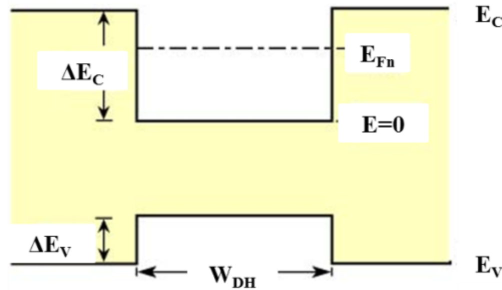

Figure 1.16: Fermi level in a double heterostructure. [28]

point the active region is flooded with carriers, causing a saturation of the optical intensity, since a further increase in injection current density will not increase the concentration in the active region. Carriers are now able to overcome the quantum well.

The current density at which the active region overflows can be obtained as follows. Consider a double heterostructure LED with an active region of thickness W_{DH}, the equation that describes the variation of the electron concentration in the active region is:

$$\frac{dn}{dt} = \frac{J}{qW_{DH}} - Bnp \tag{1.52}$$

This equation is given by two terms, one is due to the electron injection in the active region, the other one is given by the recombination. Solving the equation in steady state conditions, i.e. $dn/dt = 0$, and in high injection conditions, i.e. $n = p$, we obtain:

$$n = \sqrt{\frac{J}{qBW_{DH}}} \tag{1.53}$$

In high-density approximation, the Fermi energy is given by:

$$\frac{E_F - E_c}{kT} = \left(\frac{3\sqrt{\pi}}{4}\frac{n}{N_C}\right)^{2/3} \tag{1.54}$$

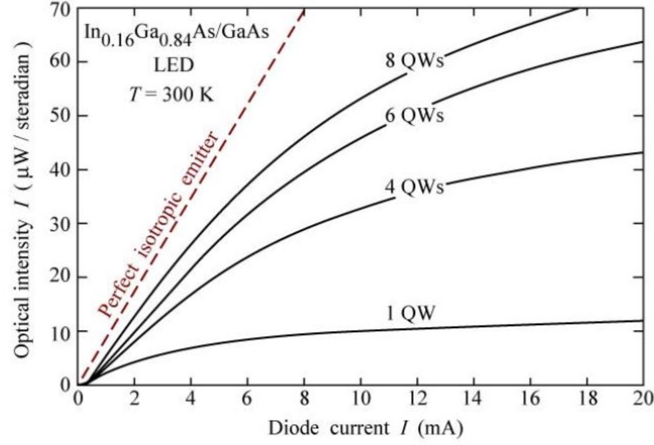

Figure 1.17: Optical intensity as function of the diode current varying the number of quantum wells. [28]

When the Fermi level reaches the top of the barrier, no more carriers will be confined. At that point $E_F - E_C = \Delta E_C$. Using this value, the current density at which the active region overflows is:

$$J = qW_{DH}Bn^2 = \left(\frac{4}{3}\frac{N_C}{\sqrt{\pi}}\right)^2 \left(\frac{\Delta E_C}{kT}\right)^3 qBW_{DH} \tag{1.55}$$

In general this problem is more severe in structures with a small active region volume, like single quantum well structures and quantum dot active regions. A possible solution is the realization of structures with multiple quantum wells (MQWs). In fact, as reported in Figure 1.17, as the number of quantum well is increased, the current level at which saturation occurs is increased, like also the optical saturation intensity.

Another possibility is to increase the height barrier ΔE_C, but this requires the employment of material with appropriate band gap. It is also possible to realized a quantum well with a larger thickness, but this solution is rare.

Electron blocking layer

The carrier escape from the active region has a strong impact in double heterostructures with low barrier height. Moreover, since the diffusion constant of electrons in semiconductor III-V is higher than the one of holes, the electron leakage current will be higher then the hole leakage current. To reduce carrier leakage, carrier-blocking layers are used: these structures are called electron blocking layer (EBL). These layers present a high band gap energy and are located at the confinement-active interface, i.e. at the interface between the active region and the barrier region on the p-side. In order to not obstruct the passage of holes coming from the p-type region, the EBL will be doped. Figure 1.18 shows an example of band diagram of a InGaN-based LED with an AlGaN-based EBL and an active region made by InGaN/GaN

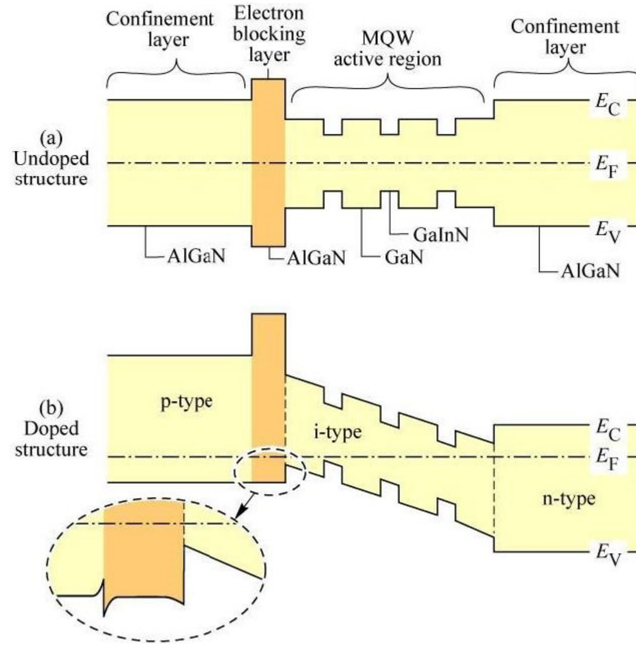

Figure 1.18: Band diagram of an LED with a MQWs structure, with (a) and without (b) doping. [28]

MQWs. The insert shows the presence of a potential spike (hole depletion layer in the electron blocker) and notch (hole accumulation layer in the p-type confinement layer), forcing holes to tunnel through the potential spike in order to reach the active layer. The valence band edge can be completely smoothed out by compositional grading at the interface between the EBL and the barrier layer so that the EBL does not impede the hole flow. The total band discontinuity is located in the conduction band, that means

$$\Delta E = E_{C,confinement} - E_{C,active} + \Delta E_g \tag{1.56}$$

where ΔE is the barrier height for electrons and ΔE_g is the difference in band gap energy between the barrier layer and the EBL.

Diode voltage

When an electron is injected, its energy is converted into optical energy upon electron-hole recombination. The drive voltage or forward voltage is given by the ratio between the band gap energy and the elementary charge

$$V = h\nu \approx E_g/q \tag{1.57}$$

There are some mechanisms that can cause a voltage variation. A first mechanism is the presence of a series resistance: this can be caused by contact resistance, by abrupt heterostructures and by bulk resistance, occurring particularly in materials with low carrier concentration

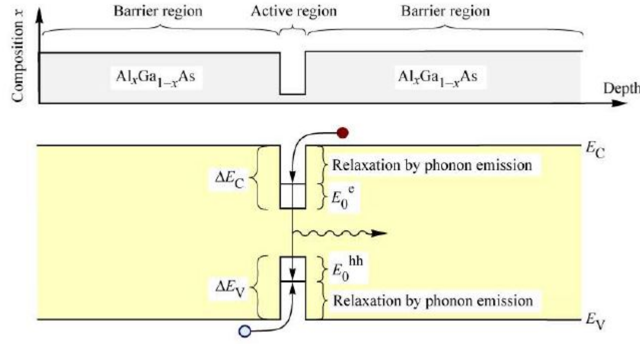

Figure 1.19: Chemical composition and band diagram of a quantum well structure. The figure shows the energy loss of carriers as they are captured into the quantum well. [28]

or low carrier mobilities. A second mechanism is related to the energy loss of carriers due to non-adiabatic injection, as shown in Figure 1.19. An electron injected in the quantum well can lose an energy equal to $\Delta E_C - E_0$, where ΔE_C is the band discontinuity and E_0 is the energy of the lowest quantized state in the conduction band. Similar consideration can be made for holes.

The total voltage drop across the LED is:

$$V = \frac{E_g}{q} + IR_S + \frac{\Delta E_C - E_0}{q} + \frac{\Delta E_V - E_0}{q} \tag{1.58}$$

where E_g/q is the theoretical voltage minimum, IR_S is the contribution due to the series resistance and $(\Delta E_C - E_0)/q + (\Delta E_V - E_0/q)$ is the contribution due to the adiabatic injection.

1.5 Optical properties of LEDs

In this section, the optical properties of LEDs will be discussed. In particular, the emission spectrum, the optical power-current characteristic and different ways in order to improve the light extraction will be discussed. First, it is important to define the efficiencies in a LED.

1.5.1 LED efficiency

The internal quantum efficiency is defined as the ratio between the number of photons emitted from the active region per second and the number of injected electrons per second, that means:

$$\eta_{IQE} = \frac{P_{int}/h\nu}{I/q} \tag{1.59}$$

where P_{int} is the optical power emitted from the active region and I is the injected current. An ideal LED has unity internal quantum efficiency, since each injected electron produces a photon. In a real LED, this is not possible, due to the presence of non-radiative recombination processes, already explained.

The extraction efficiency is defined as the ratio between the number of photons emitted outside the LED per second and the number of photons emitted from the active region per second:

$$\eta_{ext} = \frac{P/(h\nu)}{P_{int}/(h\nu)} \tag{1.60}$$

where P is the optical power emitted into free space. In an ideal LED, all the photons emitted from the active region are able to escape from the LED die, having an unity extraction efficiency. In a real LED not all the power emitted from the active region is emitted in the free space: in fact, some photons may not escape from the semiconductor due to several loss mechanisms, that will be discussed in the next paragraphs. In general, the extraction efficiency can strongly limit the LED performances.

The external quantum efficiency (EQE) is defined as the ration between the number of photons emitted outside the LED per second and the number of electrons injected into the LED per second:

$$\eta_{EQE} = \frac{P/(h\nu)}{I/q} = \eta_{IQE} \cdot \eta_{ext} \tag{1.61}$$

The power efficiency is defined as:

$$\eta_{power} = \frac{P}{IV} \tag{1.62}$$

where IV is the electrical power provided to the LED.

1.5.2 Emission spectrum

The spontaneous recombination of electron-hole pairs is the physical mechanism responsible for the light emission from the LED. The energy obtained from this process is transfered to a photon. The optical properties of LEDs are determined by the physical mechanism of spontaneous emission. Figure 1.20 reports a schematic of the electron-hole pair recombination process. The electron and hole energy distributions are defined by the Fermi statistic: at a temperature above the absolute zero, electrons and hole will occupy a certain number of energy state higher than the minimum value. Electrons and holes are assumed to have a parabolic dispersion relation:

$$E = E_C + \frac{\hbar^2 k^2}{2m_e^*} \tag{1.63}$$

for electrons, instead

$$E = E_V - \frac{\hbar^2 k^2}{2m_h^*} \tag{1.64}$$

for holes. m_e^* and m_h^* are defined as the effective masses of electron and hole, respectively,

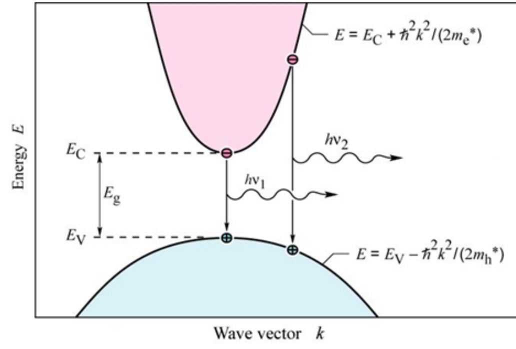

Figure 1.20: Parabolic dispersion relation for electrons and holes: figure shows the vertical recombination between an electron and a hole with the emission of a photon.[28]

$\hbar$ is the Planck constant divided by 2π, k is the carrier wave number, and E_C and E_V are, respectively, the conduction and valence band edges.

Energy conservation is required and for this reason the photon energy will be given by the difference between the electron energy E_e and the hole energy E_h. Electrons and holes present an average kinetic energy equal to kT and since $kT \ll E_g$, the photon energy will be approximately equal to the bandgap energy E_g:

$$h\nu = E_e - E_h \approx E_g \tag{1.65}$$

For this reason, the emission wavelength of a LED is determined by choosing a semiconductor material with an appropriate band gap energy.

Together with energy conservation, momentum conservation is required. Comparing the momentum of a photon, $p = \hbar k = h\nu/c = E_g/c$, with the average carrier momentum, $p = \sqrt{2m^* kT}$, yields that the carrier momentum is orders of magnitude larger than the photon momentum. In this way, during a transition from the conduction to the valence band, the electron momentum does not change significantly. The transitions are therefore "verticals", i.e. electrons will recombine only with holes that have the same value of k. Assuming that electrons and holes momentum are equal, the photon energy can be rewritten as:

$$h\nu = E_C + \frac{\hbar^2 k^2}{2m_e^*} - E_V + \frac{\hbar^2 k^2}{2m_h^*} = E_g + \frac{\hbar^2 k^2}{2m_r^*} \tag{1.66}$$

where m_r^* is the reduced mass given by:

$$\frac{1}{m_r^*} = \frac{1}{m_e^*} + \frac{1}{m_h^*} \tag{1.67}$$

Equation 1.66 is defined as joint dispersion relation and using it, the joint density of states can be calculated:

$$\rho(E) = \frac{1}{2\pi^2}\left(\frac{2m_r^*}{\hbar^2}\right)^{3/2}\sqrt{E - E_g} \tag{1.68}$$

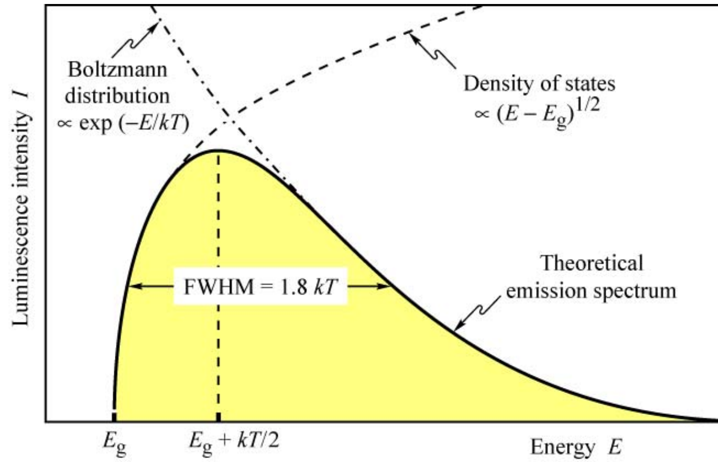

Figure 1.21: Theoretical emission spectrum of an LED. [28]

The Boltzmann distribution is used to determine the distribution of carriers in the allowed bands:

$$f_B(E) = e^{-E/(kT)} \tag{1.69}$$

The emission intensity of an LED as function of the energy (Figure 1.21) is proportional to the product of equations 1.68 and 1.69:

$$I(E) \propto \sqrt{E - E_g}\, e^{-E/(kT)} \tag{1.70}$$

From Figure 1.21 it is possible to observe that the maximum emission intensity occurs at:

$$E = E_g + \frac{1}{2}kT \tag{1.71}$$

and the full-width at half maximum (FWHM) of the emission is:

$$\Delta E = 1.8kT \tag{1.72}$$

or, in terms of wavelength:

$$\Delta\lambda = \frac{1.8kT\lambda^2}{hc} \tag{1.73}$$

The line width of an LED is relatively narrow compared with the range of the entire visible spectrum, even narrower than the spectral width of a single color as perceived by the human eye. For this reason, the LED emission is perceived by the human eye as monochromatic.

1.5.3 L-I characteristic

The optical power-current characteristic will be analyzed. Knowing the connection between this two magnitudes is useful in order to obtain information regarding recombination mecha-

nisms at a certain current level. Using the ABC model, where

- B is the bimolecular recombination coefficient;
- A is the non radiative recombination coefficient due to SRH processes;
- C is the Auger recombination coefficient;

under steady state conditions, the rate equation for the LED is:

$$\frac{dn}{dt} = \frac{J}{qd} - (Bnp + AN_T n) = 0 \tag{1.74}$$

where J is the current density through the active region, d is the active region width, N_T is the density of non-radiative recombination centers, and p and n are the electron and hole concentrations in the active region, respectively.

Under high injection conditions, where $n \gg N_a, N_d$, the previous equation becomes:

$$Bn^2 + AN_T n - \frac{J}{qd} = 0 \tag{1.75}$$

In case the radiative recombination dominates on the non-radiative recombination processes, i.e. $AN_T n \ll Bn^2$, we get

$$L = Bn^2 \approx \frac{J}{qd} \tag{1.76}$$

where L is the light intensity, since Bn^2 is related to the radiative recombination. In the other case, where the non-radiative recombination processes dominates on the radiative recombination, i.e. $AN_T n \gg Bn^2$, we get

$$AN_T n = \frac{J}{qd} \tag{1.77}$$

In this case, since n is proportional to the injected current, the light intensity (Bn^2) is proportional to the square of the injected current ($L \sim J^2$).

Figure 1.22 reports the L-I characteristic, where we can distinguish two regions:

- in the first region, the non-radiative recombination dominates; the light intensity has a square dependence on current, but since the latter is very low, the emitted light is low;
- in the second region, the radiative recombination dominates, and the relation between the optical power and the current is linear.

For very high current levels, the relation between the light intensity and the current will result in a sub-linear trend, since the Auger recombination will start to partecipate.

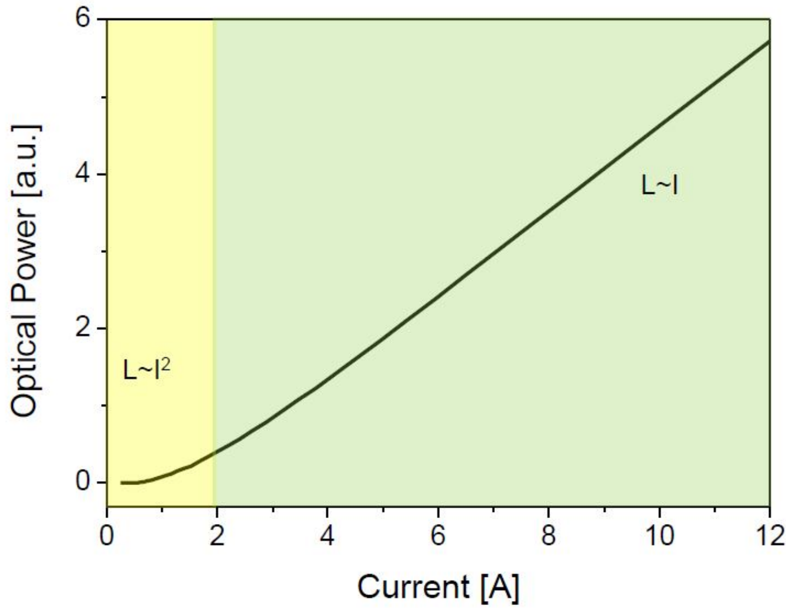

Figure 1.22: L-I characteristic of an LED. [28]

1.5.4 Light extraction

As already explained, the photon extraction can be a limiting factor for LEDs performances, if no good encapsulations are realized. Considering an LED with a simple planar heterostructure, photons are emitted from the active region with different angles of incidence. If the angle of incidence is close to normal incidence, light can escape from the semiconductor. However, if a photon arrives at the semiconductor-air interface with oblique or grazing-angle incidence, total internal reflection can occur, which reduces significantly the external efficiency, in particular for LED made with high-refractive-index materials.

Defining ϕ the angle of incidence in the semiconductor at the semiconductor-air interface, by means of the Snell law, the angle of incidence of the refracted ray Φ can be inferred:

$$\bar{n}_s \sin\phi = \bar{n}_{air} \sin\Phi \tag{1.78}$$

where $\bar{n}_s$ and $\bar{n}_{air}$ are the refractive indexes of the semiconductor and air, respectively. The critical angle for total internal reflection is defined as the angle beyond which the photons are completely reflected, as shown in Figure 1.23(a). In order to calculate it, we set $\Phi = 90°$ in the Snell law

$$\sin\phi_c = \frac{\bar{n}_{air}}{\bar{n}_s} \sin 90° = \frac{\bar{n}_{air}}{\bar{n}_s} \tag{1.79}$$

from which we obtain:

$$\phi_c = \arcsin\frac{\bar{n}_{air}}{\bar{n}_s} \approx \frac{\bar{n}_{air}}{\bar{n}_s} \tag{1.80}$$

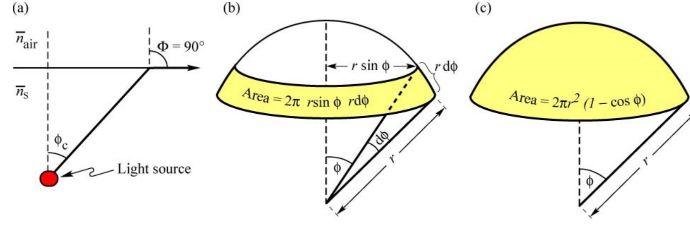

Figure 1.23: Definition of the critical angle (a), area element dA (b), and area of calotte-shaped section of the sphere (c). [28]

where this last approximation is valid since the refractive indexes of semiconductors are quite high (for example GaAs has a refractive index of 3.4).

The angle of total internal reflection defines the light escape cone: light emitted into the cone can escape from the semiconductor, whereas light emitted outside the cone is subject to total internal reflection. It is possible to calculate the number of photons that are able to escape from the semiconductor, that means the total fraction of light emitted into the light escape cone. The escape cone is projected in three dimensions: the spatial distribution of photons can be represented by means of a semi-spherical surface with amplitude lower than the critical angle. Figure 1.23(c) shows the surface area of the semi-spherical surface, defined as:

$$A = \int dA = \int_{\phi=0}^{\phi_c} 2\pi r \sin(\phi) r d\phi = 2\pi r^2 (1 - \cos\phi_c) \tag{1.81}$$

In order to calculate the emission efficiency, it will be necessary to calculate the ration between the area of the semi-spherical section of the sphere and the total area of the sphere. Assuming that light is emitted from a point-like source in the semiconductor with a total power of P_{source}, then the power that can escape from the semiconductor is given by:

$$P_{escape} = P_{source} \frac{2\pi r^2 (1 - \cos\phi_c)}{4\pi r^2} \tag{1.82}$$

where $4\pi r^2$ is the entire area of the sphere with radius r.

The fraction of light emitted that can escape from the semiconductor is:

$$\frac{P_{escape}}{P_{source}} = \frac{1}{2}(1 - \cos\phi_c) \tag{1.83}$$

The cosine term can be expanded into a power series, since the critical angle of total internal reflection for high-index materials is relatively small. Neglecting higher-than-second-order terms we obtain:

$$\frac{P_{escape}}{P_{source}} \approx \frac{1}{2}\left[1 - \left(1 - \frac{\phi_c^2}{2}\right)\right] = \frac{1}{4}\phi_c^2 \approx \frac{1}{4}\frac{\bar{n}_{air}^2}{\bar{n}_s^2} \tag{1.84}$$

In many semiconductors, the refractive index is > 2.5, thus it is high enough so that only a small percentage of the light generated by the semiconductor manage to get out.

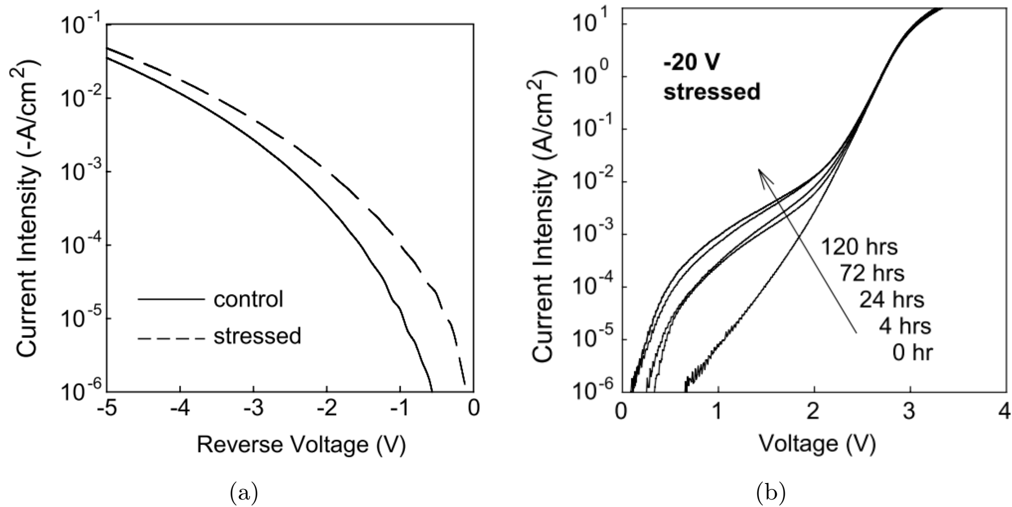

(a)

(b)

Figure 1.24: (a) reverse and (b) forward IV characterizations of LEDs submitted to constant reverse bias stress [34].

1.6 Reverse bias conduction mechanisms

The understanding of the conduction mechanisms in reverse bias is fundamental to analyze the degradation mechanisms of LEDs. In fact, the conduction in such bias condition is strongly correlated with the degradation of those devices.

When a light-emitting-diode is polarized in reverse bias conditions, a non-negligible leakage current can be detected. The intensity of such current suggests that the conduction cannot be related to the classic carriers diffusion mechanism into the semiconductors or to generation and recombination processes [33]. The conduction of leakage current in reverse bias condition is strongly correlated to the presence of leakage paths generated by the defects in the lattice, which can be emit light when the device is reversely polarized [16].

The defects that are already present in the lattice are able to propagate, giving birth to a threading dislocation: in the neighborhood of a dislocation, with the aim of reduce the mechanical strains, the lattice bonds gradually break, generating further defects. If a threading dislocation is close to the active region, it could act as efficient non-radiative recombination center: in fact, carriers can bypass the junction without recombine in the quantum wells, reducing the quantum efficiency and eventually inducing the failure of the device. The leakage conduction increase can be observed in the evolution of the IV characterization during a constant reverse bias stress: in figure 1.24b can be observed as the constant stress influences the conduction mechanisms at low forward bias conditions, inducing the leakage current increase. Being that increase proportional with the stress-time, the generation of defects in the lattice is a gradual mechanisms. At higher forward bias conditions, the IV characteristics do not show significant variations, suggesting that the deep levels assisted conduction saturates and the diffusion becomes the dominant conduction mechanism. The same leakage increase can

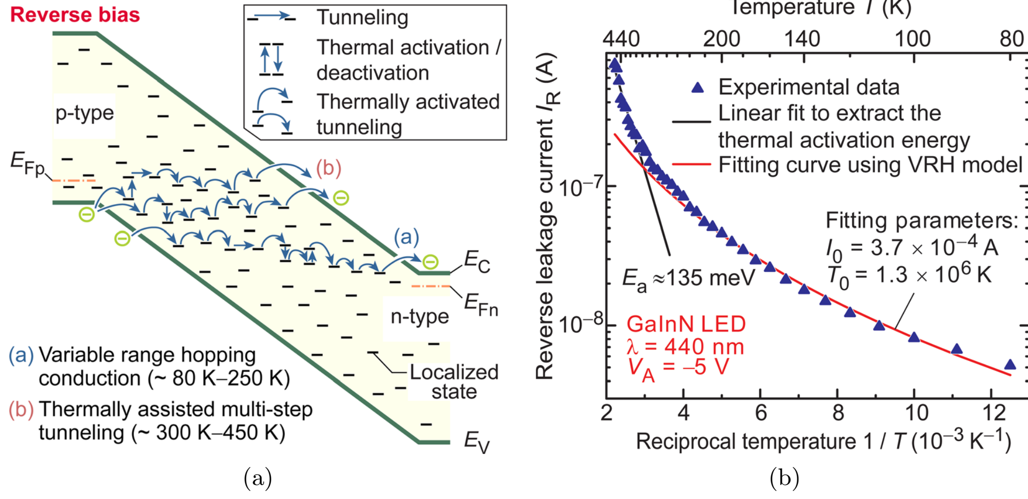

(a) (b)

Figure 1.25: (a) Schematic diagram of hopping conduction and thermally assisted multi-step tunneling [37]. (b)Arrhenius plot of the reverse leakage current at -5V of a GaInN LED. A VRH conduction model is used to fit the experimental data in the range of 80–250 K. The thermal activation energy is extracted from data in the temperature range 300–450 K [37].

be observed in the reverse IV characterization, reported in figure 1.24a.

Generally, the conduction in reverse bias conditions is related to the Mott's hopping model [35] and tunneling, but the specific type of conduction is strongly related to the operating conditions of the device:

- at low temperatures (below 250K) the conduction in reverse bias is described by the *variable range hopping* (VRH) [36], in which the conduction through the depleted region is assisted by deep levels, see figure 1.25a
- at high temperature the *thermally assisted multi-step tunneling* become the dominant conduction mechanism [37], in which the carrier pass through the potential barrier by a series of tunneling events, assisted by deep levels.

Variable range hopping According to he Mott model, in amorphous materials the VRH conduction is described by

$$I(T) \propto e^{-\left(\frac{T_0}{T}\right)^{-\frac{1}{4}}} \tag{1.85}$$

where T_0 is the characteristic temperature of the material. The model can be extended to semi-insulator crystalline materials , like the GaN at low temperatures: the p-n junction in reverse bias conditions can be assumed as an insulator submitted to a strong electric field. In this condition, at low temperatures, the VRH is the dominant conduction mechanism: considering the electric-field-enhanced hopping conduction model, the current can be expressed as

$$I = I_0 exp\left[-C\left(\frac{T_0}{T}\right)^{-\frac{1}{4}}\left(1 - C'\frac{F^2}{T^{\frac{1}{2}}}\right)\right] \tag{1.86}$$

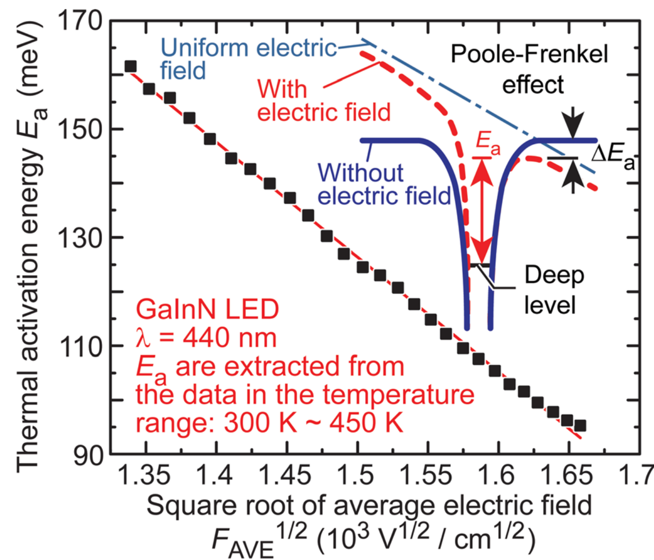

Figure 1.26: Thermal activation energy as a function of the square root of the average internal electric field in the depletion region for a GaInN LED; the inset shows the schematic diagram of the Poole-Frenkel effect. [37].

where C and C' are constants and F is the electric field [37]. The temperature dependence is limited then, if the applied voltage is constant, the model can be ascribed to the Mott model. The comparison of the model with experimental data can be observed in figure 1.25b., where a InGaN LED is biased at -5V at low temperatures.

Thermally assisted multi-step tunneling From the Arrhenius graph in figure 1.25b can be obtained the activation energy of the reverse bias (-5V) conduction mechanism in a InGaN LED, which is equal to 135meV. The activation energy related to the common drift and diffusion transport mechanisms and related to the generation and recombination of carriers into the depleted region are usually higher, several eV, comparable to the energy gap of the material. Thus, the conduction mechanism observed at temperatures higher than 250K, which is thermally activated, can be ascribed to the thermal excitation of the electrons through deep centers or from deep centers to the conduction band in the reverse-bias depletion region (or the corresponding process in the valence band) [37]. Then, the leakage current in the high temperature range can be explained by the thermally assisted multi-step tunneling. In this model, electrons transition from the valence band of p-type GaN to the conduction band of n-type GaN by multi-step tunneling and thermal activation, as reported in figure 1.25a. The deep centers enabling the reverse leakage current could be due to diffused Mg, dangling bonds, or Ga-Ga bonds occurring at dislocations [37].

Poole-Frenkel effect The aforementioned mechanisms are influenced by the electric field within the active region of the material. In fact, the band bending induced by the electric field may encourage the overcome of the potential barriers, as can be observed in the inset of the figure

1.26. This effect, called Poole-Frenkel, induces the actual reduction of the activation energy of a deep level [38]. The impact of this reduction can be expressed as

$$\Delta E_a = \beta_{PF} F^{(1/2)} = \left(\frac{e^3}{\pi \epsilon_0 \epsilon_r} \right)^{\frac{1}{2}} F^{\frac{1}{2}} \tag{1.87}$$

where β_{PF} is the Poole-Frenkel coefficient and F the applied electric-field, defined as

$$F = \frac{V_{BI} - V}{W_d} \tag{1.88}$$

where V_{BI} is the built-in potential and W_d the length of the depleted region measured at 0V (can be measured with a capacitance measurement, being $C = \epsilon / W_d$).

Direct tunneling In case of high intensity fields (above $8 \cdot 10^7$V/cm for the devices measured by Kim et al. in [38]) the direct tunneling prevails on the other conduction mechanisms. In this case, the electron does not need energy to overcome the potential barrier, but it moves through it. The current density related to this effect can be written as

$$J = \int f(E) g(E) T(E) dE \tag{1.89}$$

where $f(E)$ is the Fermi-Dirac distribution, $g(E)$ the density of states and $T(E)$ the tunneling probability.

1.7 Degradation mechanisms

The improvement of the substrates and the evolution of the epitaxial growth techniques, in which the fundamental contribute of Akasaki, Amano and Nakamura must be highlighted, allowed to achieve better GaN with lower defect density. These improvements allowed to reduce the impact of the gradual degradation mechanisms, bringing to the development of novel high power LEDs with operation junction temperatures above 150°C and lifetimes beyond the 40000 hours. Despite this, LEDs still show vulnerability to extrinsic phenomena, like electrical over stresses, which are able to induce the sudden failure of the device.

1.7.1 Gradual degradation mechanisms

Gradual degradation means the worsening of the electo-optical performance of the device triggered by specific physical mechanisms that can be enhanced by the device temperature and the bias condition and that can be, eventually, lead to the catastrophic failure of the device. The main gradual degradation mechanisms are usually related to

- generation of defects within the active region
- passivation of the acceptor dopants

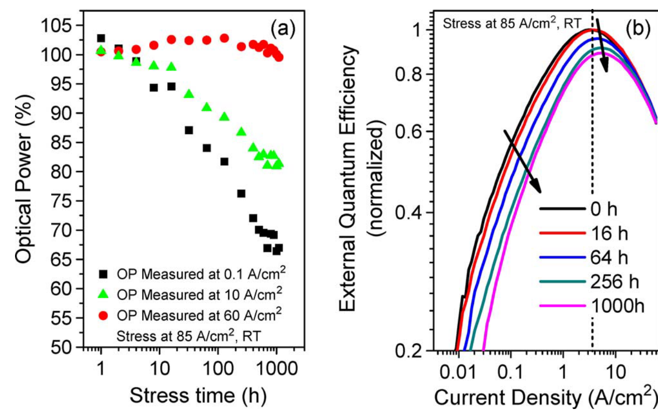

Figure 1.27: (a) Optical power decrease measured (at three different current density levels) during stress of one of the analyzed samples. (b) Efficiency versus injected current characteristics measured during stress of one of the analyzed samples (all the curves were normalized to the peak efficiency measured before stress). Stress conditions are 85 A/cm^2, RT. [11].

- ohmic contact degradation
- package-related worsening of the optical properties

Generation of non-radiative recombination centers The increase of the defect density in the active region is related to the worsening of the internal quantum efficiency, with the related decrease of the optical power. In fact, defects locally perturb the lattice periodicity, inducing the creation of allowed states inside the energy gap: those allowed states, if electrically active, may become non-radiative recombination centers. This effect is evident for low injection levels.

in figure 1.27 are reported the evolution of the optical power and the external quantum efficiency at different injection levels during a constant current stress [11]: a stronger decrease of the quantum efficiency at low current densities can be noticed. This effect can be ascribed to the generation of non-radiative recombination centers into the active region: at low injection levels, those centers can capture the carriers and induce the non-radiative recombination; at high injection levels, those centers are saturated due to the high density of carriers and they cannot reduce significantly the external efficiency of the device. Other physical mechanisms related to the efficiency drop at high injection levels can play a role.

Some of the main physical origin of non-radiative recombination centers are the propagation of threading dislocations, the diffusion of Mg atoms and the generation of nitrogen vacancies.

Degradation induced by reverse bias The main effect induced by the reverse bias conditions is the increase of the leakage current. As mentioned above, the defects already present within the lattice induce the generation of leakage paths across the junction: the gradual increase of the leakage current during a reverse bias constant stress is related to the generation of

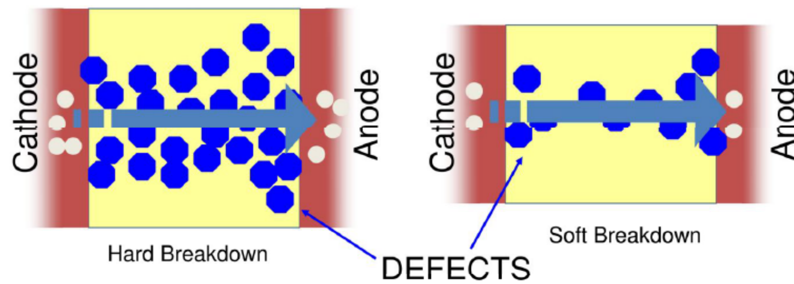

Figure 1.28: Graphical description of the hard and soft breakdown.

nano-metrical conductive paths, which expansion can be ascribed to two main mechanisms:

- *impact ionization* carriers are accelerated by the high electric field within the depleted region and acquire enough energy to induce a further lattice deformation during the impact with an atom [34]
- *self-heating* the conduction across submicro-metrical paths induce the local increase of the lattice temperature, enhancing the degradation kinetics and lead, eventually, to the melting of the material.

The gradual increase of the leakage current leads to a soft-breakdown (see figure 1.28) of the junction: during this phase, the spatially-resolved analysis of the electro-luminescence of the device allows to detect bright spots, generated by the recombination within the leakage paths. The expansion of those paths is related also to the increase of their optical emission, due to the increase of the localized carriers density. If the reverse bias condition is maintained for a long time, the breakdown may become a hard one: the expansion of the leakage paths induces the shorting of the junction and, then, the catastrophic failure of the device.

In the last moments before the failure, a sudden increase of the optical power from a single spot is typically be observed. The power dissipation across that path lead to the localized melting of the semiconductor, which could observed after the failure.

Ohmic contact and p-type region degradation Extremely high current densities and the related increase of the junction temperature may lead to the increase of the operating voltage, typically related to the optical power drop and the current crowding effect (CCE) [11], which consists in a non-uniform optical emission due to the concentration of the carriers in the region close to the metal contacts. The current spreading across the area of the device is a crucial factor for the optical performance of the device, because several works demonstrated the correlation between CCE and the efficiency drop [39, 40]. The onset of this phenomenon is related to the shape of the metal contacts and to their chemical composition and could be enhanced by high current densities, which may induce the worsening of the current spreading layer (layers with low resistivity) that has the aim to optimize the distribution of carriers.

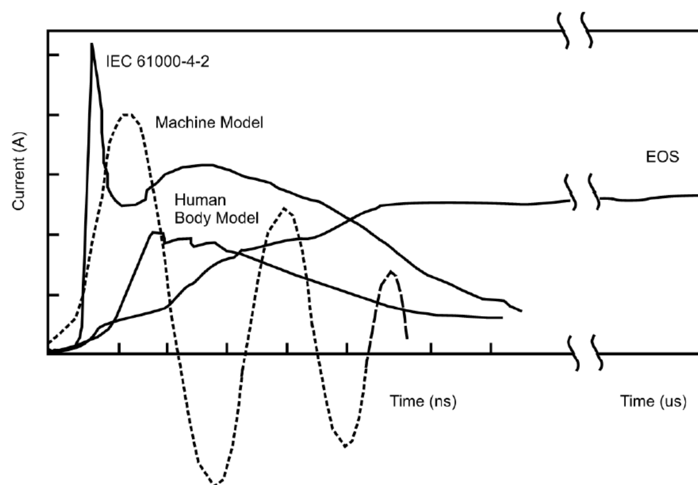

Figure 1.29: Waveforms comparison of different ESD models and EOS [41].

This kind of degradation process is manly related to the interaction between magnesium (acceptor dopant) and hydrogen in the p-type. The formation of Mg-H complexes induces

- the decrease of the active dopant density
- the resistivity increase of the metal-semiconductor contact and the p-type region
- the non-uniform distribution of carriers into the active region (CCE).

1.7.2 Catastrophic degradation

When an optoelectronic device is submitted to extrinsic events like electro-static discharges (ESD) or electrical over stresses (EOS), the failure of the device can happen immediately (catastrophic damage) [13]. In case of a general EOS, the device is submitted to a bias condition that excesses the nominal values of voltage and current that such device is able to sustain. A particular category of EOS are the ESD, which are characterized by voltage pulses of tens of KV that can last tens of nanoseconds [22]. On the other hand, a EOS (properly so called) is commonly characterized by voltages not above several tens of volts and last more than tens of microseconds. The differences between these categories are mainly related to the physical origin of those events: EOS events are generally caused by switch on and off transients of power supplies and by power lines instabilities, whereas ESD events are related to the accumulation of electrostatic charge which can be generated during the processes of manufacturing and packaging and during the handling by operators and machinery [14].

Depending on the physical origin, different models are described to simulate the ESD waveforms: human body model, machine model, charge device model. Despite this, ESD events are considered aperiodic and non repeatable. On the other hand, EOS events do not have a specific waveform but, due to their physical origin, they can be repeatable and periodic (see figure 1.29). The main physical origins of EOS events are:

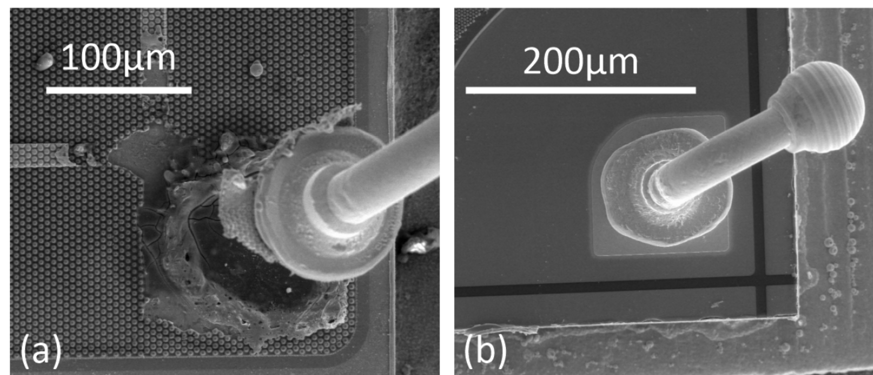

Figure 1.30: SEM images of catastrophic failures induced by EOS events on GaN based high power LEDs: (a) bonding wire detachment, (b) melting of the bonding wire. [42]

- in rush current: current overshot that may happen during the turn-on transient
- hot-plugging: connection of the device to a driver already biased
- pulsed over-current and overdrive DC of the device.

The electrical over-stress can be divided in two families [20]:

- *electrical over-current* can induce self-heating due to power dissipation (Joule effect), worsening of the material properties and lead to the melting
- *electrical over-voltage* can induce the breakdown of the semiconductor, dielectric and/or metal layers.

The impact of the EOS events are typically related to the power dissipation level on the device, like:

- bonding wire detachment (see figure 1.30a)
- melting of the bonding wire (see figure 1.30b)
- bonding pad delamination
- electro-migration
- chip cracking
- via failure (in case of flip-chip devices)

Chapter 2

Advanced characterization techniques

In this chapter, some of the advanced characterization techniques exploited in this paper will be presented. Mainly, the discussion will focus on the methods that are useful to identify the defect density in the lattice and their physical origin. The first technique is the Capacitance-Deep Level Transient Spectroscopy (DLTS) technique, that allows to measure the concentration of defects in a pn junction and to extract the signature of these defects, namely their activation energy and capture cross-section. It consists in applying a voltage pulse to the device under test and measure the associated capacitance transients over time, iterating the procedure at different temperatures. The second technique is the Deep Level Optical Spectroscopy (DLOS) technique, that allows to excite carriers, with a monochromatic light, trapped in deep levels in the bandgap, and detect the capacitance transient on the device electrodes.

2.1 Deep Level Transient Spectroscopy (DLTS)

The DLTS techniques was developed in 1974 by D.V. Lang [43] and allows to study the deep energy levels in semiconductors. In the following section, we will analyze this measurement technique, starting from the basic theoretical principles and then describing the experimental procedure.

2.1.1 Capacitance Transient

For simplicity, we will consider a p^+n-junction; the results are the same for the case of a n^+p-junction, with only trivial changes in the notation. For this reason, in our discussion we will consider only those traps in the low-doped n-side of the junction.

Figure 2.1 is a schematic summary of the emission and capture processes which characterize a particular trap. The capture and thermal emission rates for minority carriers, that in our case are holes, are c_p and e_p, respectively. Instead, for the majority carriers, in our case

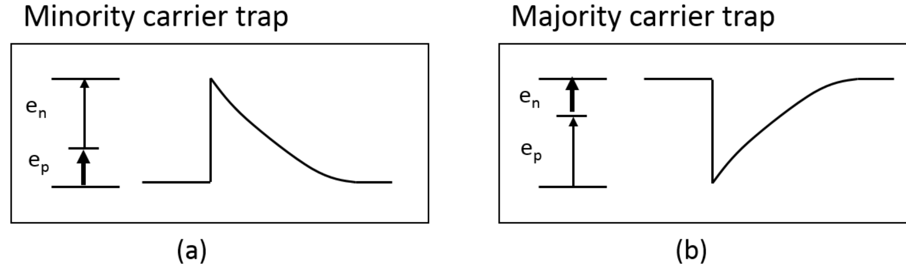

Figure 2.1: Capacitance transients in a p^+n junction in case of (a) minority-carrier traps and (b) majority-carrier traps. The larger arrows indicate that emission is the dominant process during the transient.

electrons, are c_n and e_n, respectively. The occupation state of a deep level can be described by a differential equation that takes into account the capture/emission processes:

$$\frac{\partial n_T}{\partial t} = (c_n n p_T - e_n n_T) - (c_p p n_T - e_p p_T) \tag{2.1}$$

where n_T and p_T indicate the concentration of traps filled with an electron and a hole, respectively, n and p are the electrons and holes density. By defining the total concentration of traps at the considered energy level $N_T = n_T + p_T$, the previous equation can be rewritten as:

$$\frac{\partial n_T}{\partial t} = (c_n n + e_p)(N_T - n_T) - (c_p p + e_n)n_T \tag{2.2}$$

which is a first-order differential equation on n_T. Under quasi-equilibrium conditions the carriers density is constant and one can obtain:

$$n_T(t) = n_T(0)e^{-t/\tau} + \frac{(c_n n + e_p)N_T}{c_n n + e_p + c_p p + e_n}(1 - e^{-t/\tau}) \tag{2.3}$$

where $n_T(0)$ is the initial density of occupied trap states and τ is defined as:

$$\tau = \frac{1}{c_n n + e_p + c_p p + e_n} \tag{2.4}$$

The density of states filled with an electron in steady-state is:

$$n_T(t = \infty) = \frac{c_n n + e_p}{c_n n + e_p + c_p p + e_n} N_T \tag{2.5}$$

The latter expression can be further simplified by considering than in a reverse biased p-n junction, the carrier concentration is low, therefore capture events are unlikely. This allows to rewrite the previous equation in a more usable form:

$$n_T(t = \infty) = \frac{e_p}{e_p + e_n} N_T \tag{2.6}$$

We define an electron trap as one which tends to be empty ($n_T = 0$) of electrons and thus capable to capture them. Likewise, a hole trap is one which tends to be full ($n_T = N_T$) of electrons and thus capable of having a trapped electron recombine with a hole, i.e. capture a hole. The emission rates of electrons and holes are proportional to the Boltzmann factor, which is defined as the ratio of probabilities of the two states involved in the carrier emission and depends on the states' energy difference:

$$\frac{p_1}{p_2} = exp\frac{\varepsilon_2 - \varepsilon_1}{kT} \tag{2.7}$$

where p is the probability of the state and ε is its energy. Thus, the emission rates strongly depend on the position of trap level with respect to the conduction and valence band. In case of an electron trap at energy E_T located in the upper half of the bandwidth, $|E_t - E_C| < |E_t - E_V|$ and therefore $e_p \ll e_n$. Instead, for a hole trap $e_n \ll e_p$. If the initial density of traps occupied by electrons is $n_T(0)$, the under reverse bias conditions 2.2 becomes:

$$\frac{dn_T}{dt} = -e_n n_T \tag{2.8}$$

which has solution

$$n_T(t) = n_T(0)e^{-e_n t} \tag{2.9}$$

Once electrons are emitted from the deep level, the strong electric field inside the space charge region (SCR) pushes them towards the n-side of the junction. Each electron emission, therefore, corresponds to a net increase of the total store charge. To maintain the total charge constant (the external bias is constant), the SCR shrinks and this results in an increase in the capacitance. The relationship between the junction capacitance and the density of occupied traps in the case of an ideal junction can be written as:

$$C = \epsilon A \left[\frac{q(N_D - n_T)}{2\epsilon(V_{bi} - V_R)} \right]^{1/2} \tag{2.10}$$

where A is the junction area, V_{bi} and V_R the built-in and bias voltage, respectively, N_D the n-type dopant concentration and the ϵ the dielectric constant. The previous equation can be rewritten as:

$$C = C_\infty \left(1 - \frac{n_T(t)}{N_D} \right)^{1/2} \quad , \quad C_\infty = \epsilon A \left[\frac{qN_D}{2\epsilon(V_{bi} - V_R)} \right]^{1/2} \tag{2.11}$$

where steady-state capacitance C_∞, i.e. the capacitance value after any detrapping process occurred, is decoupled. This expression can be further simplified by considering that the defect density is much lower than the dopant concentration, i.e. $n_T \leq N_T \ll N_D$. Under this condition, using the approximation $(1+x)^n \approx 1 + nx$ which is valid for $x < 0.1$, one obtains:

$$C(t) = C_\infty\left(1 - \frac{n_T(t)}{2N_D}\right) = C_\infty\left(1 - \frac{n_T(0)}{2N_D}\exp\left(-\frac{t}{\tau_n}\right)\right) \quad (2.12)$$

where $\tau_n = 1/e_n$ is the trap's emission time constant of electrons. This formula shows that the capacitance transient due to the emission of trapped electrons is an exponential function with a time constant equal to the inverse of the emission rate. Similar considerations can be used to analyze the case of hole traps, obtaining an exponential capacitance transient having time constant $\tau_p = 1/e_p$.

The sign of the capacitance change depends on whether the electron occupation of the trap had been increased or decreased by the bias pulse given in order to cause the capacitance change. An increase in trapped minority carriers, that in our case means holes, causes an increase in the junction capacitance (the total charge in the SCR decreases). As shown in Figure 2.1, the shape of the capacitance transient is an indicator of the type of traps under investigation: capacitance transient due to a minority carrier trap is always positive, whereas the transient due to a majority-carrier trap (electrons) is always negative.

The concentration of the trap can be obtained directly from the capacitance change. Assuming $n_T(0) = N_T$ and $n_T(\infty) = 0$, one obtains:

$$\frac{C_\infty - C(0)}{C_\infty} = \frac{n_T(0) - n_T(\infty)}{2N_D} = \frac{N_T}{2N_D} = \frac{\Delta C}{C} \quad (2.13)$$

where ΔC is the capacitance change at $t = 0$. Therefore, the concentration of defects is:

$$N_T \approx 2\frac{\Delta C}{C}N_D \quad (2.14)$$

This estimation of the defect density could lead to inaccurate results for small values of the reverse bias V_R, as will be discussed later in this section. However, in practical applications, this approach is often preferred over more accurate methods whose application is not trivial. Moreover, most of the times the effective dopant concentration N_D is not precisely known, thus further justifying a simpler approach for the defect density estimation.

2.1.2 Bias Voltage Pulses

By applying the adequate filling voltage pulses it will allow the traps to capture carriers. There are two main types of filling pulses, namely, a minority-carrier pulse, which momentarily drives the diode into forward bias and injects minority carriers into the region of observation, and a majority-carrier filling pulse, which momentarily reduces the diode bias and introduces only majority carriers into the region of observation. As Figure 2.2 shows, we start applying a reverse bias voltage V_R at the beginning; after that, the majority-carrier filling pulse V_f, where $|V_f| < |V_R|$, is applied for a certain time t_{FP}. After the filling pulse, the voltage returns to V_R in order to observe the capacitance transient. As a result, the SCR shrinks and some of the traps previously located inside of it are now in the quasi-neutral region, where the free-carrier

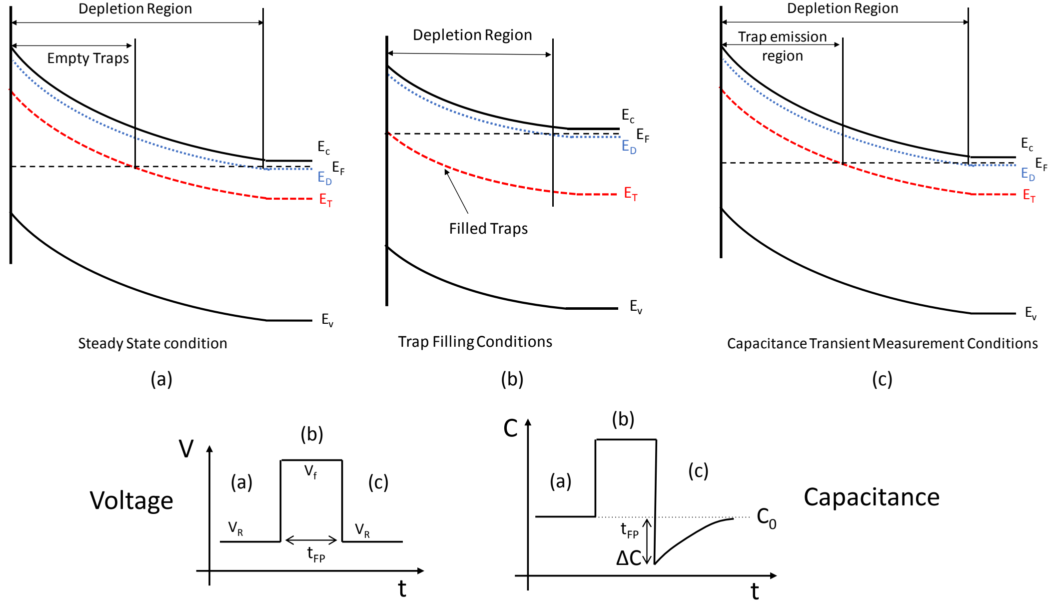

Figure 2.2: Evolution of band diagram during the capacitance transient measurement for a p^+n junction characterized by the presence of a majority-carrier trap localized at the energy level E_T in the bandgap. The figure shows only the band diagram of the n-side.

concentration n is high. As a consequence, the capture process dominates and the traps can be filled with electrons. The total amount of captured carriers depends on the duration of the filling pulse t_{FP}: a longer pulse will result in a higher number of filled traps. As already mentioned before, after the filling pulse, the voltage returns to V_R and the SCR width increases. However, due to the presence of trapped carriers, the initial width of the SCR will be different from its steady-state value and this difference corresponds to the initial capacitance peak ΔC introduced in the previous paragraph. The subsequent emission of trapped carriers gives rise to the capacitance transient previously discussed.

In order to study a minority-carrier defects, it is necessary to previously fill it with carriers and this is achieved by applying a positive filling pulse. However, during such pulse, both minority and majority carriers are flowing through the junction, therefore the initial occupation state of the traps will be a function of both the capture rates c_n and c_p.

2.1.3 DLTS measurement procedure

The DLTS measurement apparatus consists in a temperature-controlled cryostat, where the sample is mounted, connected to a capacitance monitor and a waveform generator. The latter applies the reverse bias V_R and the filling pulse V_f for a certain period, while the capacitance meter records the capacitance transient. The measurement is then repeated for several times by changing the temperature. One important feature of the DLTS technique is the ability to set an emission rate window such that the measurement apparatus only

responds when it sees a transient with a rate within this window. Thus, if the emission rate of a trap is varied by varying the sample temperature, the instrument will show a response peak at the temperature where the trap emission rate is within the window. These emission rates are thermally activated and, considering an electron emitted by a deep level located at $(E_C - E_t)$ eV below the conduction band, the emission probability is given by:

$$e_n = \upsilon_{th}\sigma_n N_C \exp\left[\frac{E_t - E_C}{kT}\right] \tag{2.15}$$

where υ_{th} is the thermal velocity, σ_n is the capture cross section of the deep level, N_C is the effective density of states, k is the Boltzmann constant, T is the temperature, E_t and E_C are the energies of the deep level and the conduction band, respectively. An exactly similar equation holds for e_p. Neglecting the capture of a hole from the valence band, which is unlikely inside the SCR, the emission time constant $\tau_n = 1/e_n$ is therefore an exponential function of temperature. Thermal velocity and density of states are also temperature-dependent and for this reason the 2.15 can be rewritten as:

$$\tau_n T^2 = \frac{\exp[(E_C - E_t)/kT]}{\gamma\sigma_n} \quad , \quad \gamma = \left(\frac{\upsilon_{th}}{T^{1/2}}\right)\left(\frac{N_C}{T^{3/2}}\right) \tag{2.16}$$

Applying the logarithm, the previous equation becomes:

$$\ln(\tau_n T^2) = (E_C - E_t)\frac{1}{kT} - \ln(\sigma_n\gamma) \tag{2.17}$$

A standard means of characterizing the depth of a trap is to construct a plot $\ln(\tau_n T^2)$ vs $1/kT$, that means the emission time constant of each recorded transient, along with the corresponding temperature, represents a data point of an Arrhenius plot. The slope of the resulting linear fit represents the distant between the conduction band and the deep level, called activation energy, while the capture cross section can be extracted from the intercept value b, that is:

$$b = \ln\left(\frac{1}{\gamma\sigma_n}\right) \quad , \quad \sigma_n = \frac{1}{\gamma e^b} \tag{2.18}$$

The very same arguments still apply in case of a hole trap, but the activation energy indicates the distance $E_t - E_V$ and γ parameter needs to be recalculated properly.

2.1.4 The dual-gate integrator (double boxcar)

The DLTS apparatus presented here makes use of a dual-gate integrated method, also called double boxcar, to determine the emission rate window and to provide signal averaging capability to enhance the signal-to-noise ratio for the detection of low-concentration traps. The use of a double boxcar to select the rate window is illustrated in Figure 2.3. According to this method, each capacitance transient is sampled at two times t_1 and t_2 after the filling pulse.

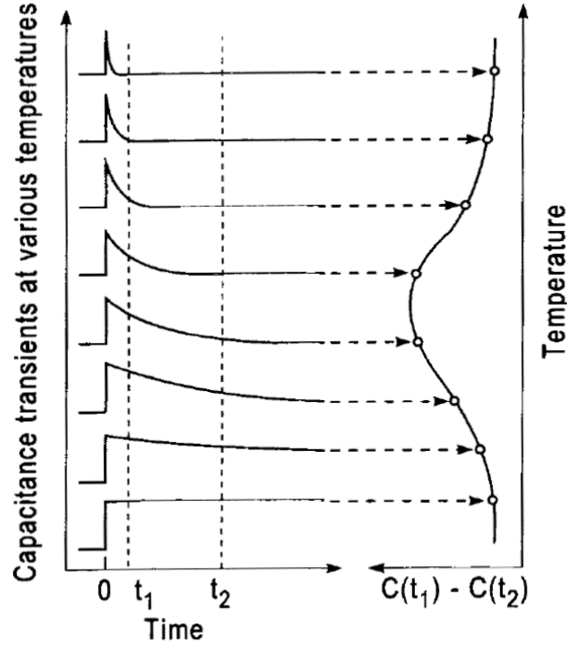

Figure 2.3: Illustration of how a dual-gate integrator (or double-boxcar integrator) is used to define the rate window. The left-hand side shows the capacitance transients at different temperatures, and the right-hand side shows the corresponding DLTS signal resulting from using the double boxcar to display the difference between the capacitance at t_1 and the capacitance at t_2 as function of temperature.

The difference between the capacitance values at these two times, $C(t_1) - C(t_2)$, gives the so-called DLTS signal. This quantity goes through a maximum when the time constant of the transients becomes comparable with the time interval $t_2 - t_1$. Instead, the signal will be negligible for both very fast and slow transients, corresponding to high and low temperatures, respectively, as shown in Figure 2.3.

It is possible to derive the relationship between τ_{max}, the value of τ at the maximum of the DLTS signal for a particular trap, and the position of the two times t_1 and t_2. The parameter that we called rate window is now defined to be τ_{max}^{-1}. Let's define the normalized DLTS signal $S(T)$ as:

$$S(T) = [C(t_1) - C(t_2)]/\Delta C \tag{2.19}$$

where ΔC is the capacitance change due to the pulse at $t = 0$, already introduced in paragraph 2.1.1. Assuming exponential capacitance transients:

$$S(T) = \exp(-t_1/\tau) - \exp(-t_2/\tau) = \exp(-t_1/\tau)[1 - \exp(-\Delta t/\tau)] \tag{2.20}$$

where $\Delta t = t_2 - t_1$. The relationship between τ_{max} and t_1 and t_2 is simply determined by differentiating $S(T)$ with respect to τ and setting the result equal to zero. The final result is:

$$\tau_{max} = (t_1 - t_2)[\ln(1_1/t_2)]^{-1} \tag{2.21}$$

Thus, the temperature that corresponds to the peak in the DLTS signal together with the corresponding time constant τ_{max} may be used in constructing the semilog activation energy plot as expressed by equation 2.17. Other data points can similarly be obtained from other scans made by varying the sampling instants t_1 and t_2 and finding the temperatures that maximize the corresponding DLTS signals.

2.1.5 Trap concentration profile

Another important information that we can obtain from the capacitance transient is the trap concentration as function of the position inside the SCR. We suppose that in an asymmetric p^+n junction the space-charge region has width W when all traps are empty. Consider an interval between x and $x+\Delta x$ having $n(x)$ electrons trapped in a deep level, where $0 < x < W$. Assuming that Δx is small, the trapped negative charge will cause an increase in the space-charge width ΔW and a consequent variation in the electric field ΔE. The latter consists in two terms, one related to the new ionized donors $\Delta E'$ and one related to the trapped electrons $\Delta E''$:

$$\Delta E' = \frac{q}{\epsilon} N_D \Delta W \quad , \quad \Delta E'' = -\frac{q}{\epsilon} n(x) \Delta x \tag{2.22}$$

From the Poisson equation, each contributions leads to a voltage drop variation equal to:

$$\Delta V' \approx \frac{q}{\epsilon} N_D \Delta W (W + \Delta W) \approx \frac{q}{\epsilon} N_D W \Delta W \quad , \quad \Delta V'' = -\frac{q}{\epsilon} n(x) x \Delta x \tag{2.23}$$

The total voltage variation is expressed as:

$$\Delta V = \frac{q}{\epsilon} [N_D W \Delta W - n(x) x \Delta x] \tag{2.24}$$

Since we are interested in capacitance changes at constant bias, we set $\Delta V = 0$ and thus:

$$\frac{\Delta W}{W} = \frac{n(x) x \Delta x}{N_D W^2} \tag{2.25}$$

Knowing the expression of the junction capacitance under reverse bias, $C = \epsilon A/W$, we finally obtain:

$$\left[\frac{\Delta C}{C}\right]_x \approx \left[-\frac{\Delta W}{W}\right]_x = -\frac{n(x)}{N_D W^2} x \Delta x \tag{2.26}$$

It is interesting to observe that the sensitivity of the junction to trapped charge varies linearly from zero at the junction ($x = 0$) to a maximum at the edge of the depletion region ($x = W$). This means that capacitance measurements are very insensitive to traps located at the junction

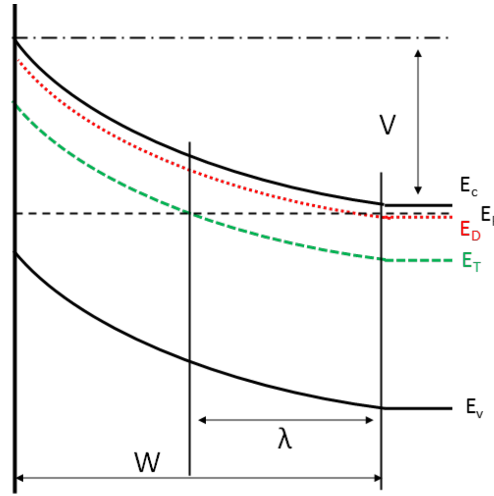

Figure 2.4: Band diagram of a $p^{+}n$ junction showing the parameter λ.

or at the surface of the semiconductor for the Schottky barrier diode.

In order to calculate the capacitance transient amplitude ΔC, we must integrate equation 2.26 over the region of the space-charge layer where emission takes place, that is the region where the traps are filled during the filling pulse. Figure 2.4 shows the band diagram for a $p^{+}n$ junction having a uniformly doped n region with a deep level located at E_T. The space charge region can be divided into two sections: the central region closest to the junction, where both the shallow donors and the deep levels lies above the Fermi level, that is depleted; the second region, defined from the point where the Fermi level crosses the trap energy level to the edge of the depletion region, where all the traps are filled with electrons. The width of this region, called "edge region", is defined as:

$$\lambda = \sqrt{\frac{2\epsilon(E_F - E_T)}{q^2 N_D}} \tag{2.27}$$

which does not depend on the polarization voltage, but on the energy difference between the Fermi level E_F and the trap level E_T. Although there are sufficient carriers in the edge region to affect the trap occupation and so the capacitance transient amplitude, there are not enough to affect the band bending and they can be ignored in the calculation of the depletion width. This approach can be justified since the error in the depletion width W is negligible [43]. The total signal $\Delta C/C$ produced by a filling voltage pulse V_{FP} long enough to fill all the traps is obtained integrating 2.26 between $W(V_{FP} - \lambda)$ and $W(V_R) - \lambda$:

$$\frac{\Delta C}{C} = -\frac{N_T}{2N_D}\left[1 - 2\frac{\lambda}{W(V_R)}\left(1 - \frac{C(V_R)}{C(V_{FP})}\right) - \left(\frac{C(V_R)}{C(V_{FP})}\right)^2\right] \tag{2.28}$$

If the edge region is neglected ($\lambda = 0$), like also the quadratic term, this equation simplifies in:

$$\frac{\Delta C}{C} \approx -\frac{N_T}{2N_D} \tag{2.29}$$

and therefore we can obtain the usual equation for the defect concentration:

$$N_T \approx \left| 2\frac{\Delta C}{C} N_D \right| \tag{2.30}$$

This equation is the same obtained in 2.14, which was calculated neglecting the edge region. We still have to neglect the quadratic term in order to obtain the same result, since equation 2.14 assumes that the filled traps are distributed along the whole extension of the SCR, which corresponds to perform the integration from 0 instead of $W(V_{FP})$. Applying this, at $W = 0$ the capacitance will be $C = \infty$, the quadratic term is zero and we obtain again 2.14. However, neglecting the edge region may cause significant underestimation of the trap concentration, especially at low reverse bias voltages.

Knowing the variation of the depletion width with applied bias, we are able to estimate the deep level concentration profile. Basically, the concentration profile of a trap can be determined by using the difference in transients that result from two slightly different filling pulses. The difference between the transient amplitude measured at two filling pulse voltages is a measure of the trap concentration from the region corresponding to the deep level depletion at each of the filling pulses. We assume that during the filling pulse all traps get filled. Starting from the equation 2.26, the total capacitance variation can be written as:

$$\frac{\Delta C}{C} = \int_{z_n}^{W} -z\frac{N_T(z)}{N_D W^2} dz \tag{2.31}$$

where z_n is the width of the SCR during the filling pulse V_{FP}. Differentiating the latter equation leads to:

$$\delta\left(\frac{\Delta C}{C}\right) = \frac{N_T(z_n)}{N_D W^2} z_n \delta z_n \tag{2.32}$$

with δz_n defined as the variation of the SCR edge induced by a variation of the filling pulse δV_{FP}. Using the relation $C(z_n) = \epsilon A/z_n$ and taking into account the definition of capacitance:

$$C(z_n) = \left.\frac{dQ}{dV_{FP}}\right|_{W(V_{FP})=z_n} = \frac{qAN_D(z_n)dz_n}{dV_{FP}} \tag{2.33}$$

we obtain that the incremental change in the relative capacitance signal, due to the traps filled by the small change in voltage δV_{FP} is:

$$\delta\left(\frac{\Delta C}{C}\right) = \frac{N_T(z_n)}{N_D(z_n)}\left(\frac{\epsilon}{qN_D W^2}\right)\delta V_{FP} \tag{2.34}$$

where W is the depletion width where $V = V_R$, $N_D(z_n)$ is the dopant concentration at position z_n and N_D is the average dopant concentration. $N_D(z_n)$ is typically measured using C-V profiling methods, that means measuring the capacitance-voltage characteristics and then

extracting the apparent charge profile along the depletion width, assuming an asymmetric junction.

Basically, during this measurement a reverse bias voltage V_R is applied in order to determine the steady-state depletion width W. After that, the filling pulse voltage V_{FP} is varied of an amount equal to δV_{FP}, starting from a minimum value grater or at least equal to V_R, and a measurement of $\Delta C/C$ is performed. Usually, δV_{FP} is kept constant between measurements. Finally, the defect concentration profile can be estimated as:

$$N_T(z_n) = N_D(z_n)\left(\frac{qN_D W^2}{\epsilon}\right)\frac{\delta(\Delta C/C)}{\delta V_{FP}} \tag{2.35}$$

2.1.6 Capture process characterization

There are different types of defects in semiconductor. We can divide these in two principal categories: point-defects and extended defects. Studying the capture kinetic behavior allows one to distinguish what kind of defect is under investigation

Comparison of the pulse width dependence of the capacitance transient amplitude to the expected behavior for various capture mechanisms will show what the closest match is for the trapping process. In other words, the analysis consists in measuring the initial ΔC capacitance peak at varying filling pulse duration t_{FP}, while keeping the sample at the temperature corresponding to the peak in the DLTS signal associated to the deep level that we want to study. A capture process at a simple point defect is described by the following equation:

$$\Delta C(t_p) = \Delta C_{max}(1 - \exp(-n\sigma_n \upsilon t_{FP})) \tag{2.36}$$

where ΔC_{max} is the amplitude of the transient, n is the shallow carrier concentration, υ is the thermal velocity, σ_n is the capture cross section and t_{FP} is the filling pulse width.

Capture by a point defect with a fixed capture barrier modifies the capture process by introducing an exponential term to the capture cross section according to:

$$\Delta C(t_{FP}) = \Delta C_{max}(1 - \exp(-c_n t_{FP})) \quad , \quad c_n = \upsilon n \sigma_n^{\infty} \exp\left(\frac{-\Delta E_b}{kT}\right) \tag{2.37}$$

where the terms are the same as before, except σ_n^{∞} is the high temperature capture cross section, and ΔE_b is the capture barrier energy. A capture barrier is shown schematically in Figure 2.5, where the red line represents the capture barrier.

A third possibility is that the trap is related to a dislocation. Charge build-up along a dislocation line produces a Coulombic repulsion, resisting capture of further charges, described by:

$$n_T(t_{FP}) = \sigma_n \upsilon \tau n N_T \ln\left(\frac{t_{FP} + \tau}{\tau}\right) \tag{2.38}$$

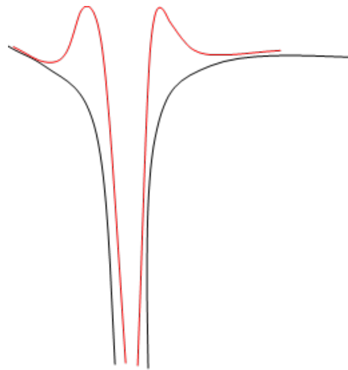

Figure 2.5: Energy pit due to a point defect (black line) with the presence of the capture barrier (red line).

where N_T is the trap concentration, τ is the inverse of the capture rate ($n\sigma_n v$) scaled by he ratio of the equilibrium trap occupation to the barrier energy, where the barrier energy is proportional to the trap occupation.

Plotting the transient amplitude ΔC as function of the natural log of the filling pulse width will show that, in case of linearly arranged extended defect, the dependence will be linear: this means that we have a slow increase in occupied traps with increase in filling pulse, consistent with trapping along a dislocation.

2.2 Deep Level Optical Spectroscopy

The main limitation of the DLTS technique is that only deep levels with activation energy lower than 1 - 1.5 eV can be effectively detected. In order to thermally activate traps with higher activation energy, the devices should be heated up to temperature levels that would likely damage them. Deep level optical spectroscopy (DLOS) is a technique that overcome this limits, allowing the detection of traps across the whole bandgap. The main drawbacks of this method, compared to the standard DLTS, are its increased complexity and the much longer time required for the measurement.

The DLOS techniques was developed in 1980 by A. Chantre, G. Vincent and D. Bois [44] and this also allows to study the deep energy levels in semiconductors in a similar way the DLTS does. In particular, the DLOS techniques exploits a monochromatic excitation to induce the detrapping of carriers in the depleted region. In the following section, we will analyze this measurement technique, starting from the basic theoretical principles and then describing the experimental procedure.

2.2.1 The working principle

When photons are sent into the depletion region of a junction, the deep-level occupancy can be changed by the optically induced emission of carriers, leading to a change of the capacitance of the junction. This is the basic idea of either steady-state or transient photo-capacitance

measurements. If temperature is low enough so that thermal release of trapped carriers can be neglected, the evolution of the occupancy of the level under illumination is given by the classical differential equation

$$\frac{dn_t}{dt} = -\sigma_n^0 \Phi n_t + \sigma_p^0 \Phi p_t \tag{2.39}$$

where n_t and $p_t = N_t - n_t$ are the concentrations of electrons and holes trapped on the level, σ_n^0 and σ_p^0 the optical cross sections for the emission of electrons in the conduction band and holes in the valence band, respectively, and Φ is the intensity of the incident light. At time t = 0, equation 2.39 can be simplified by choosing an initial condition such that only one of the two terms remains.

(i) If, at time $t = 0$, all the centers are filled with electrons, $n_t(0) = N_t$ and $p_t(0) = 0$, 2.39 becomes

$$\left(\frac{dn_t}{dt}\right)_0 = -\sigma_n^0 \Phi N_t \tag{2.40}$$

N_t being a constant and $\Phi(h\nu)$ given by a previous calibration of the monochromator output; the $\sigma_n^o(hv)$ spectrum can be obtained by measuring the initial derivative of the capacitance transient $[(d\Delta C/dt)_0 \propto (dn_t/dt)_0]$ just after the beginning of the illumination.

(ii) On the other hand if, at time $t = 0$, all the centers are filled with holes, $p_t(0) = N_t$ and $n_t(0) = 0$, then the same measurement will lead to the $\sigma_p^o(hv)$ spectrum, according to the relation

$$\left(\frac{dn_t}{dt}\right)_0 = -\sigma_p^0 \Phi N_t. \tag{2.41}$$

Taking into account this so-called "transition" region, 2.39 must be rewritten, in each point x of the depletion region, as (n-type material)

$$\frac{dn_t}{dt}(x,t) = -\sigma_n^0 \Phi n_t(x,t) + [\sigma_p^0 \Phi + C_n n(x)] p_t(x,t) \tag{2.42}$$

where C_n is the electron capture rate of the level and n(x) represents the free-carrier tail in the depletion region. Equation 2.42 shows that, in the case of initial condition (i) (all centers filled with electrons), this transition region has no influence, since $p_t(x,0) = 0$ for whatever values of x. The situation is different in the case of conditions (ii), because within the transition region, the centers cannot be filled with holes, due to the presence of the free-carrier tail [$n_t(x,0) \neq 0$ in this region], so that some contribution of σ_n^0 might be expected in the derivative of the photo-capacitance transient. In fact, such a perturbation arises only at the edge of the transition region, i.e., next to that point where the Fermi level crosses the level; deeper in the material, where $C_n n(x)$ is much larger as compared to the optical emission rates, the occupancy of the level remains unchanged under illumination. This "edge" region thus concerns only a limited number of trap centers and its effect can be neglected as soon as a large enough (a few volts) reverse bias and not too high a photon flux are used.

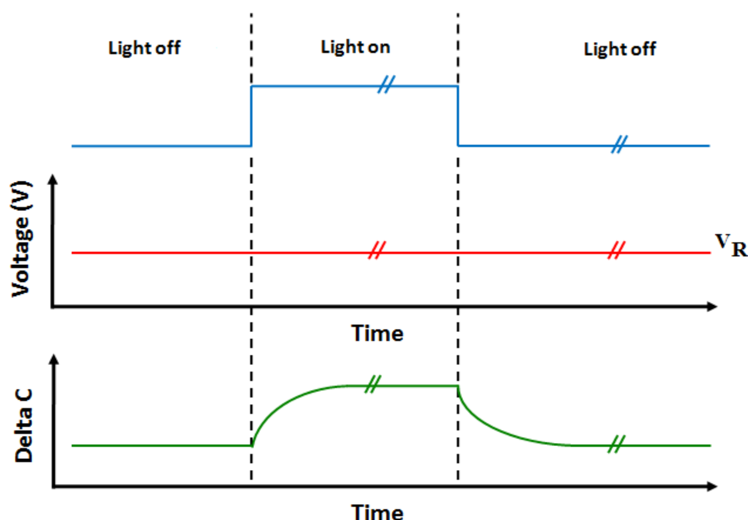

Figure 2.6: Schematic representation of a DLOS measurement.

2.2.2 The experimental procedure

The device under test is biased with a reverse voltage V_R, whose magnitude is chosen depending on which region of the junction has to be observed. At a certain instant t the LED surface is illuminated with a monochromatic light: as a consequence, electrons or holes trapped in a deep level will be excited in the conduction or valence band by the absorption of photons, resulting in a variation in the junction capacitance. As in a DLTS measurement, the capacitance will increase or decrease depending on the type of the trap. A positive variation of the capacitance corresponds to the emission of majority carriers from trap levels, while a negative variation corresponds to the emission of minority carriers. After the capacitance under illumination reaches the steady-stave value, the light source is turned of and the capacitance starts to return to its initial value. A schematic representation of the temporal evolution of a DLOS measurement is shown in figure 2.6. In the following treatment, we will refer to a p+n junction with a majority carrier trap localized in the n-side. Like for DLTS, the results can be easily extended to a minority carrier trap or to a p-type semiconductor with minor notation adjustments. Figure 2.7 describes how the band diagram of the n-side of the junction changes during the several steps of a DLOS measurement. With reference to the figure, E_D represents the energy of a donor level, E_T the energy of a majority carrier trap level within the bandgap and E_{Fn} is the quasi- Fermi level on the n-side. The trap is supposed to be neutral when occupied by electrons, positively charged when empty and located below the Fermi level far from the junction. With these assumptions, the band diagram evolves as follows:

- At the beginning, in figure 2.7a, the light is of and the capacitance is at its steady state value. Both the donors and the trap states located above E_{Fn} are empty, as indicated with the "+" symbols, and the depletion region edge is at the edge of the empty donors.
- At a certain instant the light is turned on, figure 2.7b. The incident light is absorbed

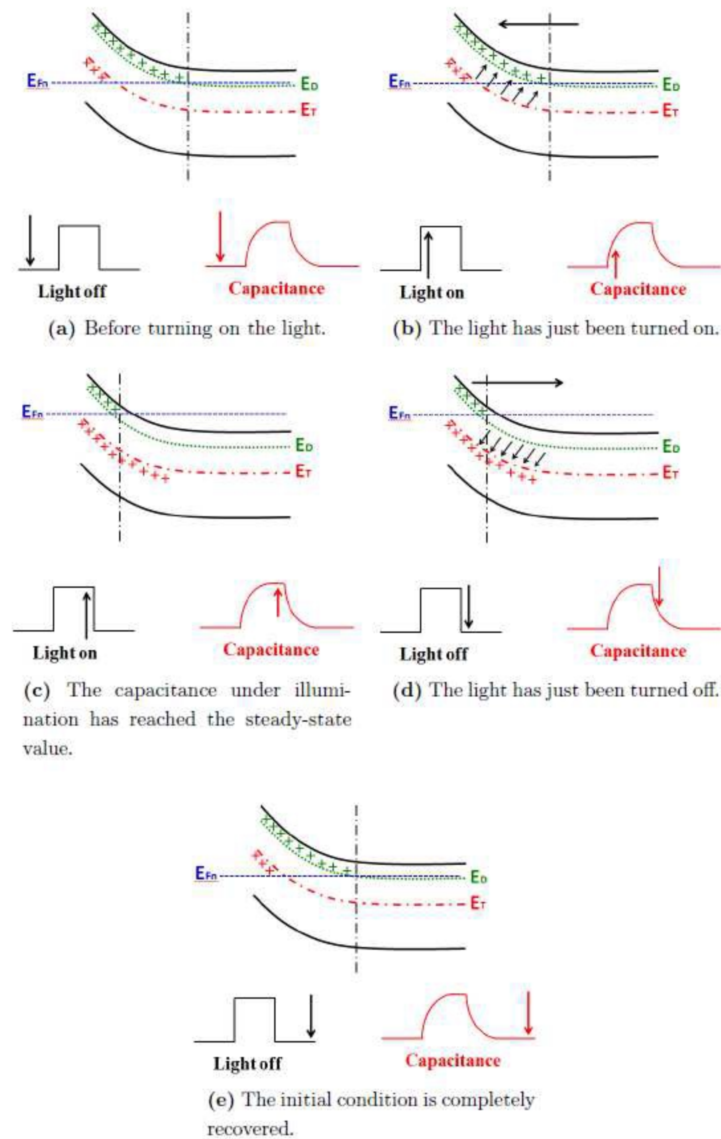

(a) Before turning on the light.

(b) The light has just been turned on.

(c) The capacitance under illumination has reached the steady-state value.

(d) The light has just been turned off.

(e) The initial condition is completely recovered.

Figure 2.7: Band diagram of a p+n junction during the various steps of a DLOS measurement. A majority carrier trap is supposed to be localized E_T eV below the conduction band. Only the n-side of the junction is shown.

by the semiconductor causing the photo-excitation of some of the trapped electrons, which are then excited in the donor level or in the conduction band. Assuming that the optical emission rate of electrons from trap states is much larger than the capture rate, to maintain the charge neutrality the quasi-Fermi level increases and the space-charge region shrinks. As a consequence, the capacitance increases.

- After a certain period, the system reaches the steady-state condition under illumination and the capacitance stops increasing (figure 2.7c).
- When light is turned of, figure 2.7d, the system is in a non-equilibrium condition: some of the empty trap states starts to capture electrons and, correspondingly, more donors are going to be ionized to maintain the charge neutrality. As a consequence, the capacitance decreases. However, being the trap levels located deeply inside the band gap, this capture process requires a certain amount of time, which results in a capacitance transient that depends on the trapping kinetics of the defects.
- Eventually, the initial steady-state conditions are restored and the capacitance stops decreasing, figure 2.7e.

In all DLOS measurements presented in this thesis, the monochromatic light was generated by means of a 50 W quartz-halogen lamp, providing an illumination range spanning from the near- IR to visible, connected to a monochromator. Higher order modes were cut out by means of an automated optical filter wheel, to avoid possible further excitation of electrons from the trap states that could influence the measurements. Finally, a lens system focused the light on the sample. The latter was mounted on a thermally controlled stage. This allowed us to simultaneously avoid measurement errors due to temperature fluctuations and to speed up the recovering capacitance transients, thus reducing the overall measurement time (higher temperatures corresponds to faster capture kinetics). The excitation period (i.e. when the light is turned on) and the recovering period (i.e. light is turned of) duration were dynamically adjusted based on the incident wavelength, in order to always allow the capacitance to reach the steady-state value under illumination and to fully recover to its initial value after that. The correct amount of time required was determined manually by observing the transients at some representative wavelengths.

2.2.3 Steady-State Photo-Capacitance

The more straightforward analysis that can be performed with a DLOS setup is the spectral dependence of the Steady-State Photocapacitance (SSPC), which allows to estimate the trap density N_T . To obtain the SSPC spectrum, the capacitance variation ΔC (or alternatively the normalized value $\Delta C/C$) due to the optical excitation (see figure 2.8a) is measured for each wavelength. Then, these values are plotted versus their respective wavelength, obtaining a chart similar to that in figure 2.8b. With varying incident light energy, several changes in the slope of the SSPC can be observed. Each of them corresponds to the onset of emission

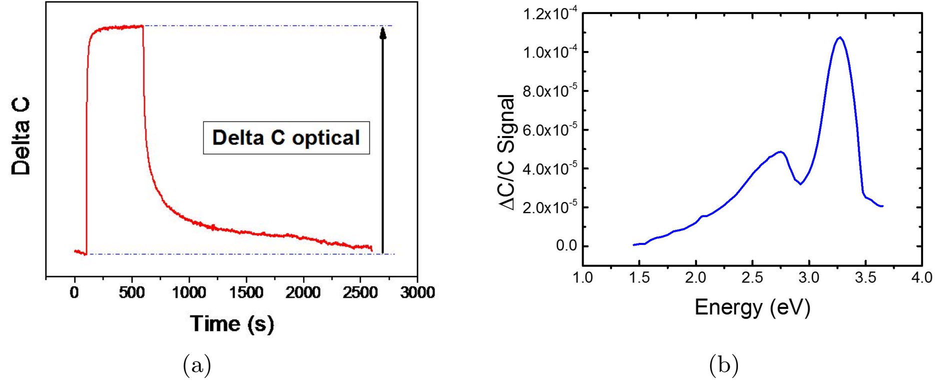

(a) (b)

Figure 2.8: (a) Typical capacitance transient obtained using a given wavelength of monochromatic incident light during a DLOS measurement. (b)Typical steady-state photo-capacitance spectrum.

of carriers from a deep level. However, these onsets are not located at the optical ionization energy E_0 of the deep level, but in proximity of the energy $h\nu = E_0 - d_{FC}$, where the latter term d_{FC} is called Franck-Condon energy [45]. E_0 is the minimum energy required for a photon to promote an electron or hole from a localized bandgap state to a delocalized state upon absorption. Very deep traps, on the other hand, may strongly couple to the lattice and relax to a new atomic configuration upon carrier capture or emission. The Franck-Condon term d_{FC} represents the energy released in the form of multi-phonon excitation as the local bonding configuration relaxes around a defect center immediately after a photoabsorption or photoemission event. As a consequence, it is not possible to determine the position of deep levels from the SSPC spectrum only, without the prior knowledge of the Franck-Condon energy. Figure 2.8b also shows a rapid decrease in the SSPC signal for high incident energies. Such behavior can be explained by considering the absorption of light from the GaN material, preventing the photons from reaching the active region of the LED. The concentration of trap states N_T for a n-type semiconductor can be expressed by [45]

$$\frac{\Delta C}{C} \approx \frac{N_T}{2N_D} \frac{\sigma_n}{\sigma_n + \sigma_p} \tag{2.43}$$

where $\Delta C/C$ can be extracted from the SSPC data, N_D is the donor concentration, and σ_n (σ_p) is the capture-cross section for electrons (holes). This expression is evaluated for the value of $h\nu$ that yields the largest photocapacitance response, and its applicability is limited to the case where $\Delta C \ll C$, corresponding to a moderate defect concentration. The optical ionization and the Franck-Condon energies of a deep level can be determined using a theoretical model that requires the knowledge of the spectral dependence of its photoionization optical cross-section (PCS) σ_0. The latter can be expressed as

$$\sigma_0(h\nu) = \frac{1}{\Phi(h\nu)\tau(h\nu)} \tag{2.44}$$

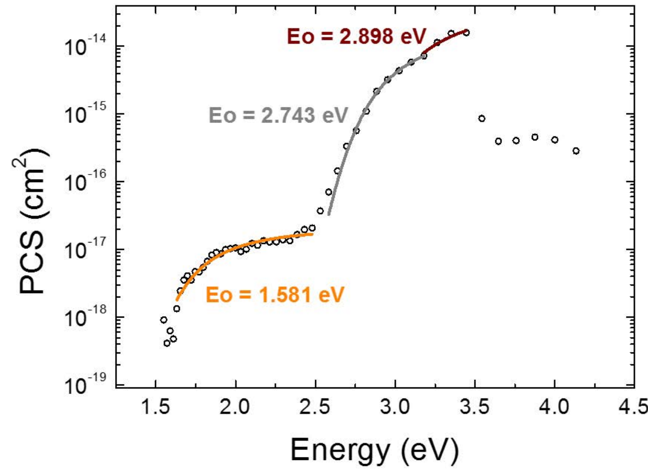

Figure 2.9: Example of optical photoionization cross-section (empty dots). Each transition in the PCS curve corresponds to the presence of a deep level and has been fitted with the Passler model (solid lines). Only the optical ionization energy of the identified levels is shown.

where $\Phi(h\nu)$ is the photon flux emitted by the lamp, expressed as photons/cm^2·s and $\tau(h\nu)$ is the carrier lifetime of the deep level. The photon flux can be easily measured by placing a calibrated photodetector at the output of the monochromator. To determine the carrier lifetime the optical transients, such that in figure 2.8a, have to be fitted at the beginning of the excitation phase with a first order exponential function [46]:

$$\Delta C(t) = \Delta C_0 \left(1 - e^{-t/\tau} \right). \tag{2.45}$$

The above equation describes the capacitance change induced by a single deep level under optical excitation. If more than one deep level contribute to the transients, a deviation from this ideal behavior may occur. Fitting the transients at the very beginning of the illumination period minimizes the contribution of multiple deep levels. The estimation of E_0 and d_{FC} can be obtained by fitting the PCS curve with a theoretical model proposed by Passler in [47]. A typical PCS plot looks like the one in figure 2.9 and is characterized by several different regions, having a parabolic-like behavior. Each of these regions corresponds to a deep level and shall therefore be fitted with the Passler model, using E_0 and d_{FC} as fitting parameters. The empty dots in figure 2.9 are the experimental PCS data, indicating the presence of three different deep levels. The solid lines are the obtained fittings evaluated with the Passler model, along with the estimated optical ionization energy. Generally, the thresholds in the PCS and SSPC spectra exhibit close agreement. However, phonon-assisted photoionization from lattice-coupled deep levels may result in a temperature dependent broadening of the PCS characteristic, leading to absorption thresholds for $h\nu < E_0$ and larger d_{FC} energies [45]. In such cases, sensible differences between the PCS and the SSPC thresholds can occur.

Chapter 3

Effects of growth parameters of GaN-based LEDs on the ESD robustness

Electrical Over-Stress (EOS) refers to a condition whereby the device is biased above the absolute maximum electrical value specified by the manufacturer. Since the EOS is a very broad concept, many are the possible sources, including power-on and power-off transients, inrush and hot plugging currents, latch-up conditions and device overdriving [14]. A specific group of EOS events can be defined as Electro-Static Discharges (ESD). An ESD and a generic EOS mainly differ for the time duration: the very ESD has a duration that spreads from ns to the μs whereas an EOS can reach the order of seconds [20].

In this part, a comparison among growth parameters, DC and pulsed characterization results and ESD stability will be presented. The aim of this work is to analyze the degradation processes responsible for the LEDs failure and identify which growth parameters are giving the most robust samples. This activity was carried out in collaboration with an industrial partner: due to the confidentiality of the presented data, the nature of the growth parameters and their actual values will be not specified.

3.1 Variations on n-side

The samples analyzed in this work are state-of-art high power blue GaN-based LEDs with a surface area of 1x1 mm^2 circa. The epitaxial parameters will be mentioned as parameters "A" and "B" and they refer to thickness of layers on the n-side. Their numerical values are only a relative reference to the aim of the comparison.

All the samples were submitted to capacitance-voltage (C-V), DC and pulsed current-voltage (I-V) and electro-luminescence (L-I) characterizations performed with experimental setups. The pulsed characterization was carried out with a custom high power pulser based on a capacitor and high power MOSFET. In this setup, the capacitor is pre-charged by a power supply, then a micro-controller enables the MOSFET, allowing the discharge of the capacitance through the device under test. The voltage and current waveforms are recorded

by two differential voltage probes, connected to a 500 MHz 2-channel oscilloscope. To measure the current waveform, a small resistor was placed in series to the device under test: measuring the voltage drop across the resistor we were able to calculate the amount of current that was flowing through the sample. As result, the waveform data were collected with a 4-wire configuration. The ESD tests were performed with a commercial setup able to generate discharges with a duration of 50ns.

3.1.1 DC and pulsed characterization

In order to understand the effects of the different parameters on the device characteristics, the different families of samples are shown gathered together when only one parameter is varying.

Sample	Par. A	Par. B
J	0	0
H	0	0.5
F	0	1
D	0	2

in figure 3.1 are reported the relevant correlations obtained from the measurements on the analyzed families of samples. The increase of the parameters B is related to a worsening of the ESD robustness, leading to a decrease of the average current required to reach the failure of the device. in figure 3.1a is shown the correlation between the depletion charge of the device, calculated as the integral of the capacitance within the voltage range of the CV characterization, and the average failure current: the least robust devices are the ones with a higher level for the B parameter and higher depletion charge. The high depletion charge is also related to a leakage current measured at -50V and -60V (figure 3.1b and -e) in pulsed conditions. Pulsed IV characterization are shown also at -50V due to the impossibility to reach the -60V with the D sample. By the way, the correlation at -50V are showing weaker correlations than the -60V ones, due to competing conduction mechanisms which gives noisy IV curves and a lower SNR. Leakage current and reverse bias electro-luminescence measured at such high reverse voltages are compared with average breakdown current in figure 3.1b, d and f: data suggest that weaker devices, with higher B parameter, have higher leakage current and, therefore, higher electro-luminescence in reverse bias. The higher leakage current could be ascribed to a higher concentration of defects in the structure and the related weakness to reverse ESD discharges.

A second set of families was gathered with the aim of the comparison. Here is reported the list of the different parameters.

Sample	Par. A	Par. B
J	0	0
S	1	0
A	4	0

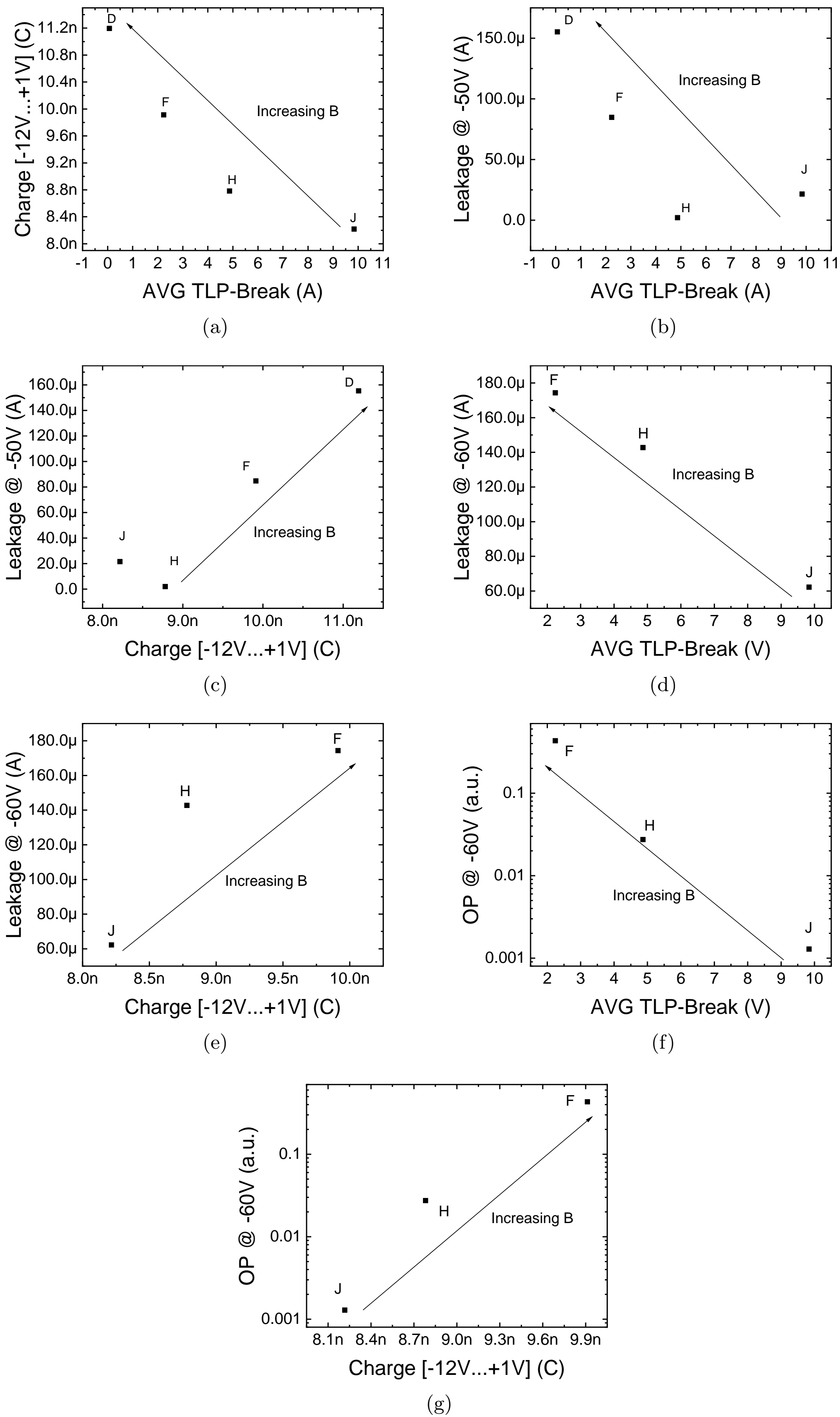

Figure 3.1: Correlations among device characteristics carried out with DC and pulsed measurements: families J, H, F and D.

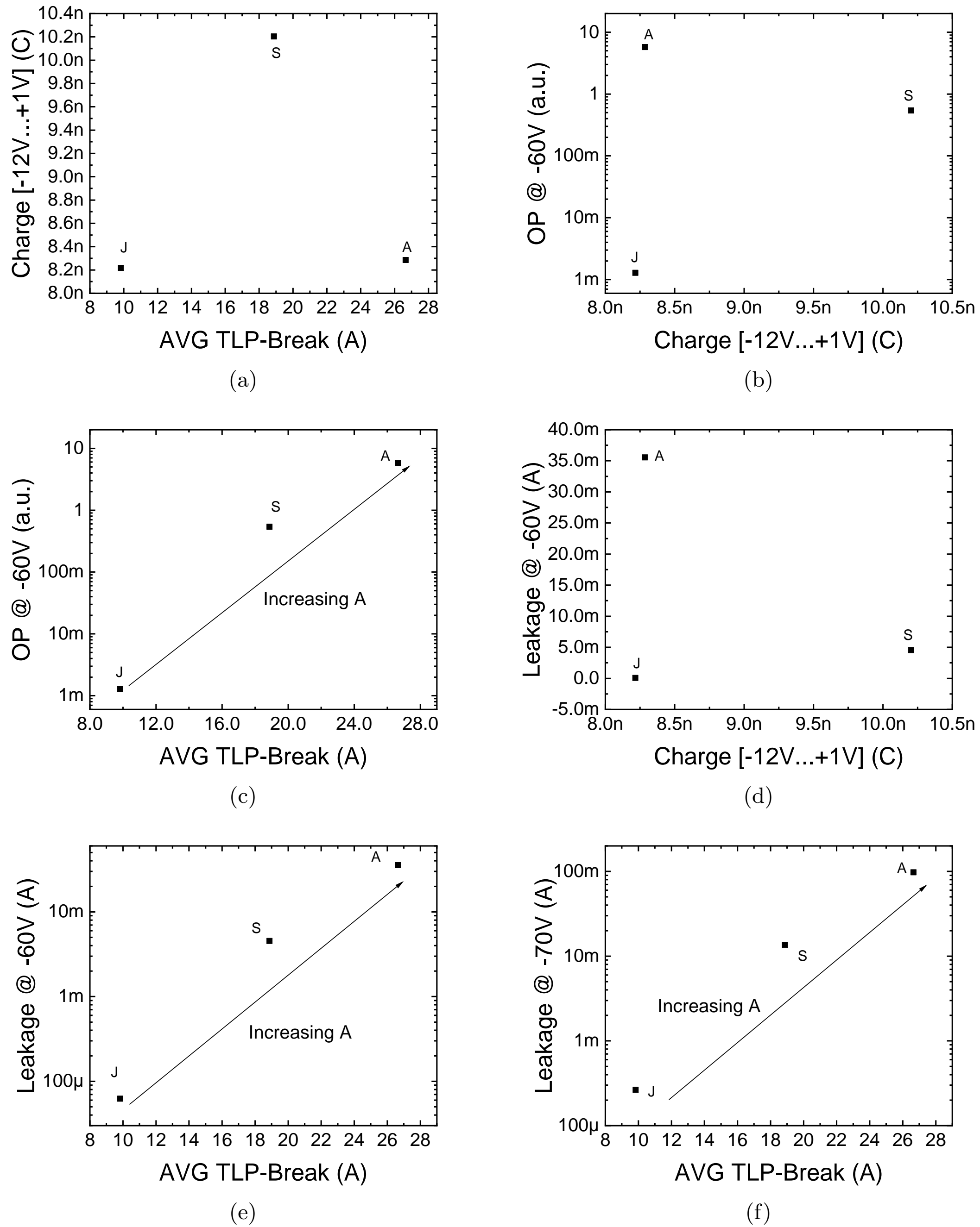

Figure 3.2: Correlations among device characteristics carried out with DC and pulsed measurements: families J, S and A.

in figure 3.2 are reported the relevant correlations obtained from the measurements on the analyzed families of samples. No apparent correlations are observed between leakage current and depletion charge (figure 3.2a, b and d). Samples of all these three families are able to sustain high reverse TLP currents, reaching -70V during pulsed IVs. From the data reported in figure 3.2c, e and f, a higher parameter A is related to higher robustness to TLP discharges but also to higher leakage current and optical power. In the first set of families, where B parameter is increasing and A one is fixed at 0, J sample is the most robust, whereas here J is the weakest. This suggests that the impact of the parameter B on the ESD robustness is weaker than the parameter A one.

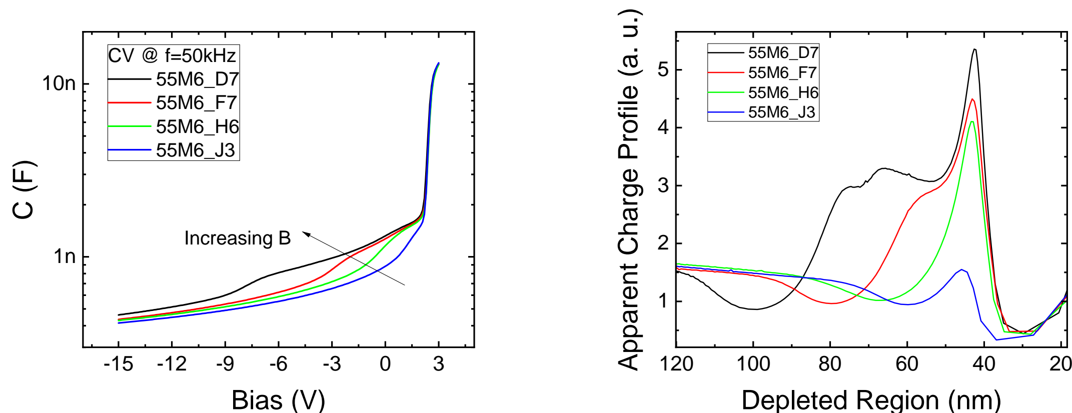

(a) *CV characterization at 50kHz of the four analyzed families.*

(b) *Comparison among the apparent charge profiles over the depleted region of the analyzed samples.*

Figure 3.3: Comparison among devices that differs in the value of B parameter.

3.1.2 Capacitance DLTS measurements

In order to achieve a deeper understanding of the physical cause of the different ESD robustness of devices belonging to different families, capacitance DLTS measurements were carried out. As preliminary characterization, capacitance-voltage (CV) measurements at the frequency of 50kHz were performed. The results are reported in figure 3.3a: the increase of the B parameter results in a shift of the bending point in the CV. Apparent charge profiles were calculated (figure 3.3b) starting from the CV characterization data: the modification into the epitaxial structure related to the variation of the B parameter is more evident.

Starting from the data reported in figure 3.3b, the different samples were analyzed with an extensive C-DLTS characterization. Some relevant C-DLTS characterizations are presented in figure 3.4. Since the doping level of the p-side is, in general, significantly higher than the n-side one, the depleted region is assumed to be the n one. Starting from this assumption, in figure 3.4b a trap for holes (minority carrier) can be identified in the F7 sample. The trap is active at low temperatures with low re-emission time constant. About the D7 sample, two electron-related traps can be identified (majority carrier) in figures 3.4c and d. On the 4 analyzed groups, only D and F samples (samples with higher B) describe useful data, and DLTS peak (even if noisy) decreases in magnitude from D to F, therefore with lower values of B. For this reason, only from D and F data is possible to obtain the Arrhenius plot: activation energies of analyzed deep levels are distributed into a range between 140m and 390meV. Such values of activation energy in the InSL region are compatible with the ΔE_g on the conduction band, assuming an In concentration of $5 : 10\%$ in the In-containing superlattice. For this reason, C-DLTS characterization are might be measuring a shallow trap related to SL, rather than a defect.

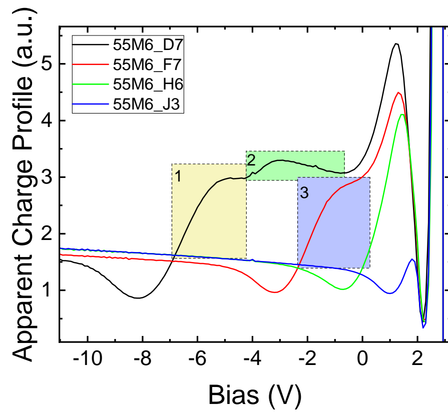

(a) *Comparison among the apparent charge profiles over the applied voltage of the analyzed samples. Analyzed regions are highlighted and numbered.*

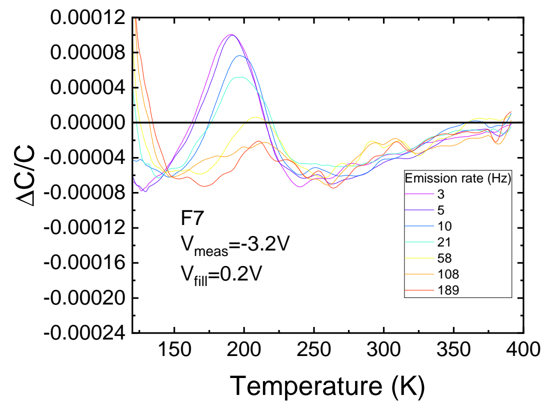

(b) *C-DLTS characterization of samples F7 in the region 3.*

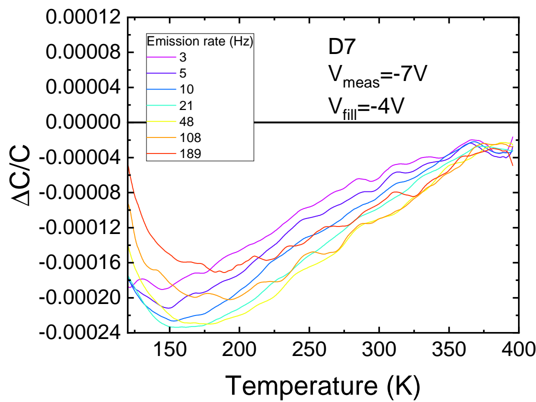

(c) *C-DLTS characterization of samples D7 in the region 1.*

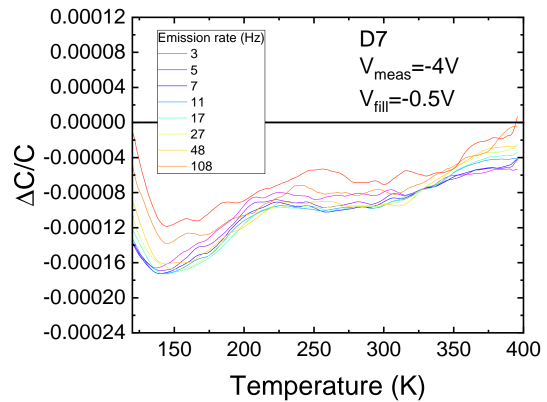

(d) *C-DLTS characterization of samples D7 in the region 2.*

Figure 3.4: C-DLTS results of the different analyzed regions.

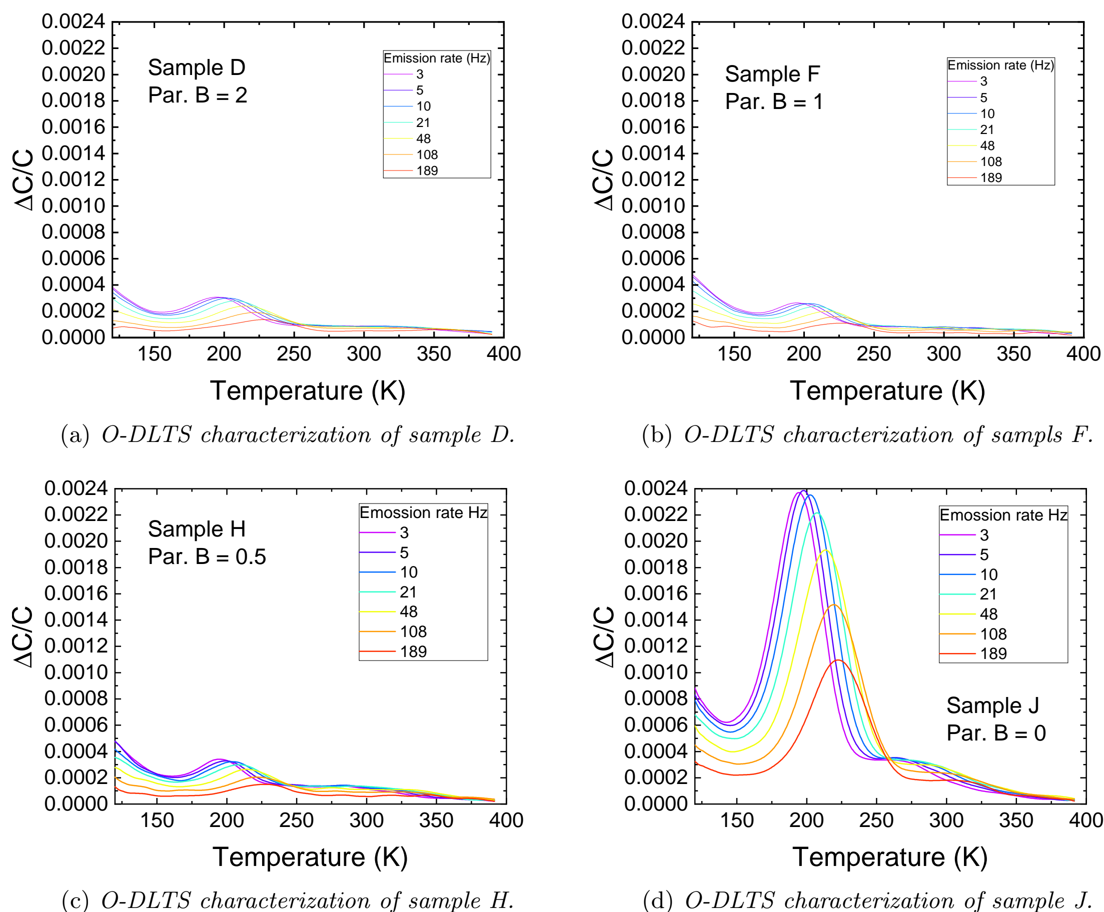

(a) *O-DLTS characterization of sample D.*

(b) *O-DLTS characterization of sampls F.*

(c) *O-DLTS characterization of sample H.*

(d) *O-DLTS characterization of sample J.*

Figure 3.5: O-DLTS results: applied voltage is different among different samples in order to fix the scanned region.

3.1.3 Optical DLTS measurements

In order to detect defects located at deeper energies, Optical-DLTS measurements were carried out. The measure voltage is now variable among the different families, with the aim to investigate the very same region close to the QWs in the different samples. Starting from the data extrapolated by the CV measurements in figures 3.3b and 3.4a, the voltage setpoints were chosen to deplete the structures till the peak in the apparent charge profile located around the 40nm.

The results of the O-DLTS characterization are reported in figure 3.5: the B increase is related to defect density decrease. Despite this, the most robust devices are the ones with the smaller B. For higher B values, the defect density in the region close to the QWs is lower. But defect density in the QWs region is not critical for the robustness of those devices to ESD discharges.

The deep levels detected with DLTS measurement were analyzed with Arrhenius analysis, detecting activation energy of traps and comparing them with the data available in the scientific literature. The comparison is visible in figure 3.6 and the results are summarized in the fol-

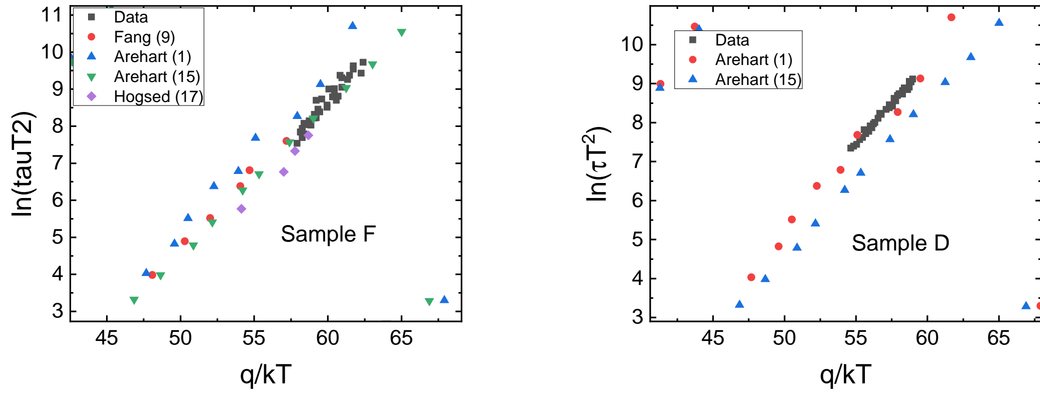

(a) *Arrhenius comparison with defects detected in sample F.*

(b) *Arrhenius comparison with defects detected in sample D.*

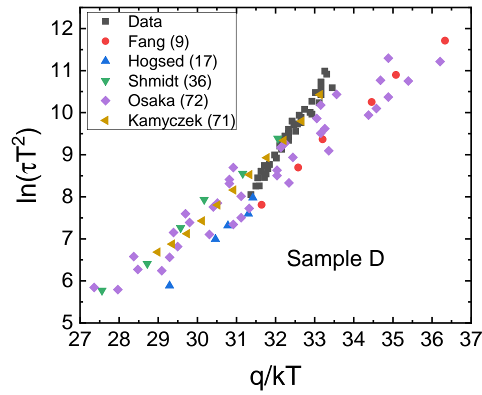

(c) *Arrhenius comparison with defects detected in sample D.*

Figure 3.6: Arrhenius analysis on the defects detected with DLTS characterization.

lowing table: according to the literature, the defects seem correlated mainly to nitrogen vacancies.

Legend	Paper	Physical origin
Fang (9)	[48]	Unknown
Arehart (1)	[49]	Unknown
Arehart (15)	[50]	Vacant nitrogen sites
Hogsed (17)	[51]	Unknown
Shmidt (36)	[52]	Unknown
Osaka (72)	[53]	N-related point defects or antisite N
Kamyczek (71)	[54]	Gallium vacancy related defect

3.2 Variations on p-side

The samples analyzed in this work are state-of-art high power blue GaN-based LEDs with a surface area of 0.5 mm^2 circa. The epitaxial parameters will be mentioned as parameters “C”, “D” and “E” and they refer to thickness and doping of layers on the p-side. Their numerical values are only a relative reference to the aim of the comparison.

As already presented for the study on the effect of n-side parameters, all the samples were submitted to capacitance-voltage (C-V), DC and pulsed current-voltage (I-V) and electro-luminescence (L-I) characterizations performed with experimental setups.

3.2.1 DC and pulsed characterization

The analysis of the role of the different parameters will be analyzed separately, in order to focus the attention on a single parameter at time.

Parameter C

The role of the C parameter will be analyzed with 2 series of families which have common D and E parameters. The first series is represented by the families H, I and J, which values of D and E are common and equal to 2 and 2.8, respectively, as reported in the following table.

Sample	Par. C	Par. D	Par. E
H	2.4	2	2.8
I	2.8	2	2.8
J	4	2	2.8

In this first set of samples, the higher values of C are related to more robust devices, with higher average breakdown current and lower leakage current in pulsed condition, as shown in figure 3.7. The lower leakage is also related to a lower electro-luminescence in pulsed reverse conditions. No other relevant correlations were detected.

Being the only comparison with more than two families, also the spatially resolved electro-luminescence in reverse bias is here analyzed. In figure 3.8 the false-color maps reveal the quantity of electro-luminescence signal, mapping the higher signal locations with red and the lower ones with blue: the sample with the highest C parameter (J) shows the most resistive behavior and the most uniform electro-luminescence pattern. This suggests that a lower C parameter may influence the density of conductive path into the device, promoting the leakage throughout the junction, the presence of bright emitting spots in reverse bias conditions and, then, the failure of the device via shorting of such leakage paths.

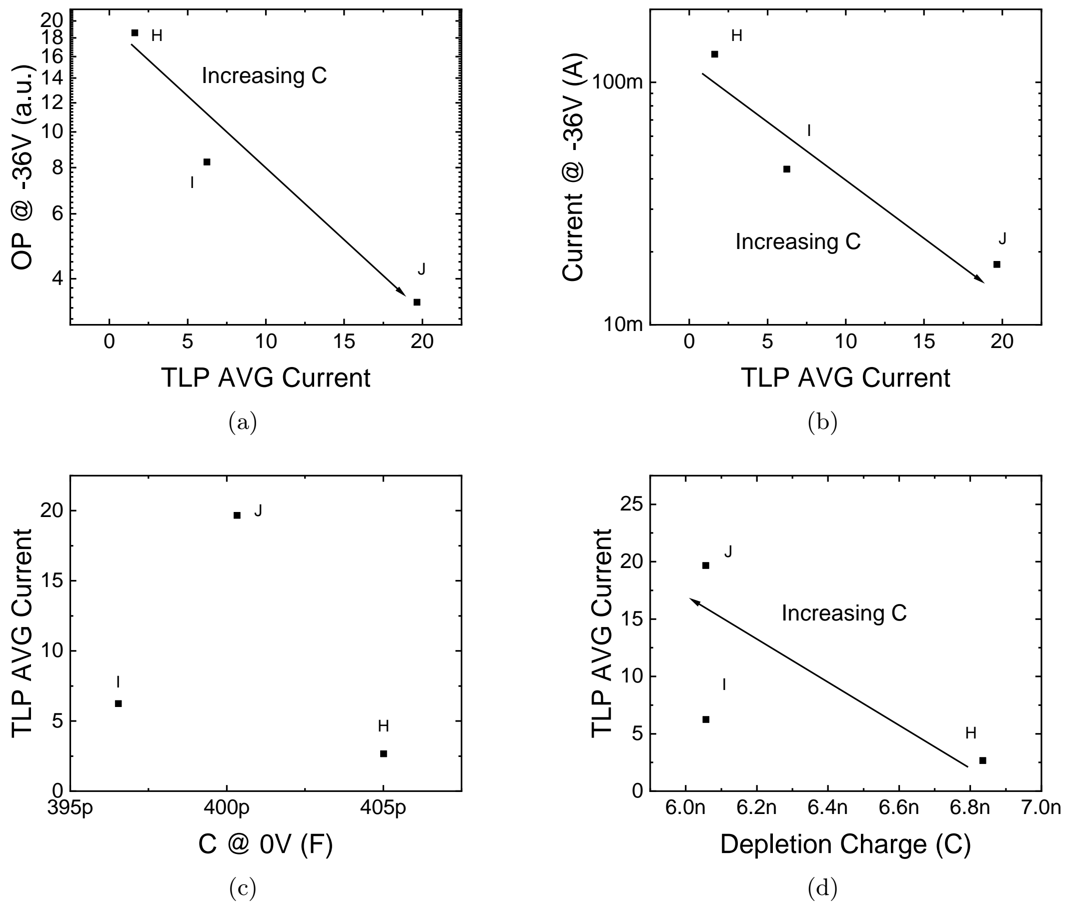

Figure 3.7: Correlations among device characteristics carried out with DC and pulsed measurements: families H, I and J.

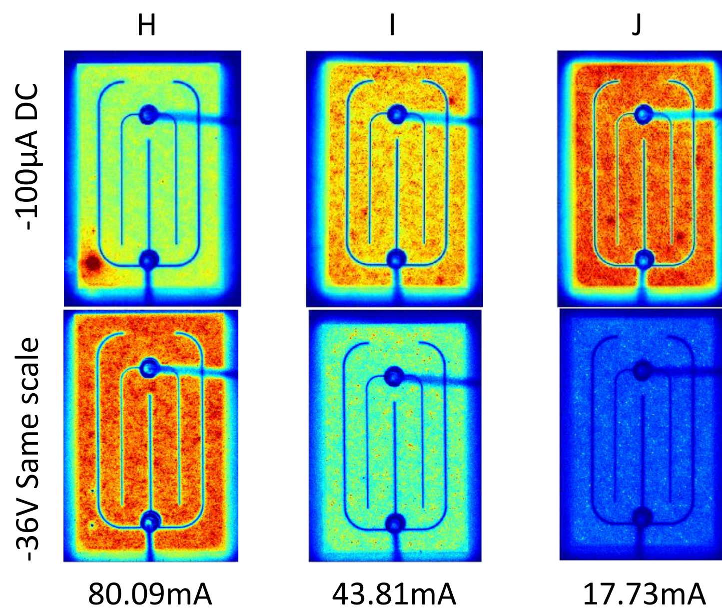

Figure 3.8: Spatially resolved electro-luminescence in reverse bias conditions: images are taken at fixed DC current (-100μA) and fixed pulsed reverse voltage (-36V). The values of current in the bottom refer to the fixed voltage condition. The amount of signal coming from bright spot in the bottom-left corner of the H sample is enough to induce the saturation of the EMCCD detector. For this reason, in the -36V image, the same spot appears as a dark spot.

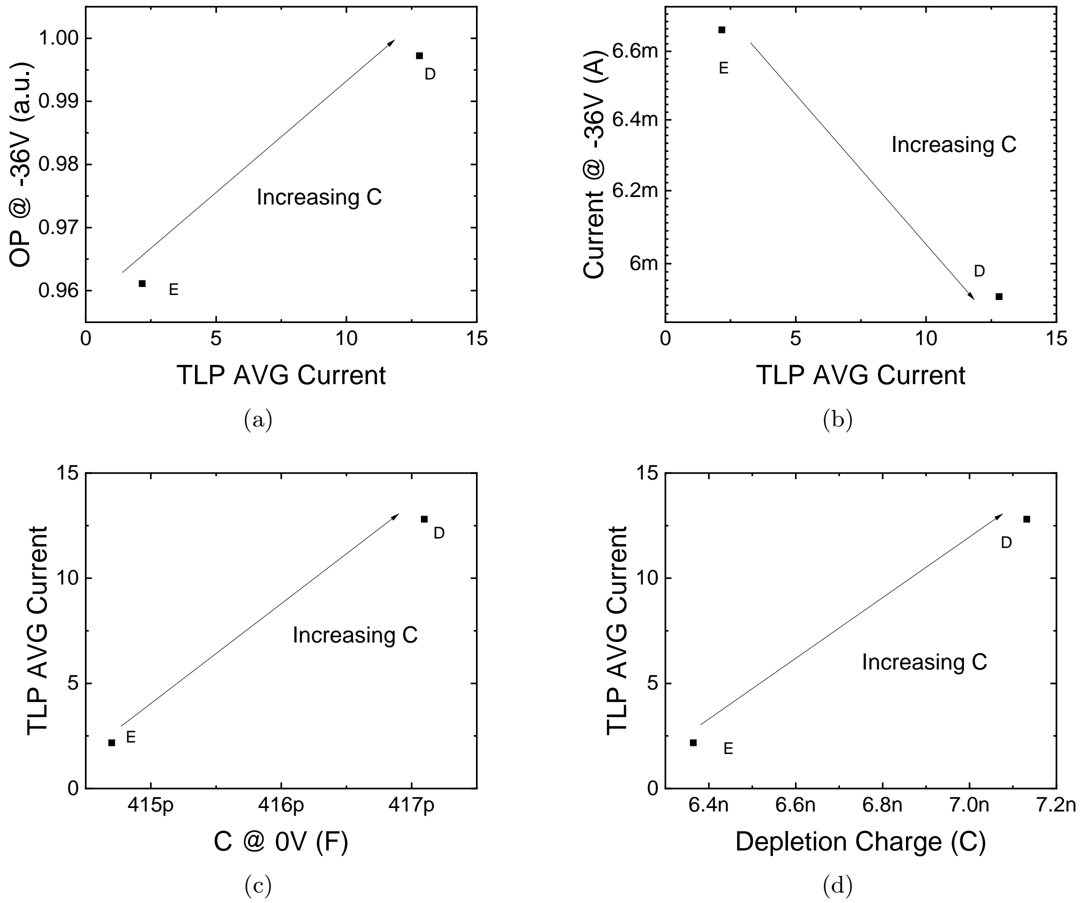

Figure 3.9: Correlations among device characteristics carried out with DC and pulsed measurements: families D and E.

A second set of samples, D and E, is useful for the study of the effects of the parameter C.

Sample	Par. C	Par. D	Par. E
D	4	1	2
E	2.8	1	2

Correlations among DC and pulsed measurements are shown in figure 3.9: higher values of C parameter are still resulting in more robust devices and lower leakage, possibly ascribed to the lower density of defects. On the other hand, the most robust device is now emitting less light than the other one: non-radiative recombination in leakage paths may play a role. Higher values of parameter C is also related to a higher capacitance of the device and a higher depletion charge.

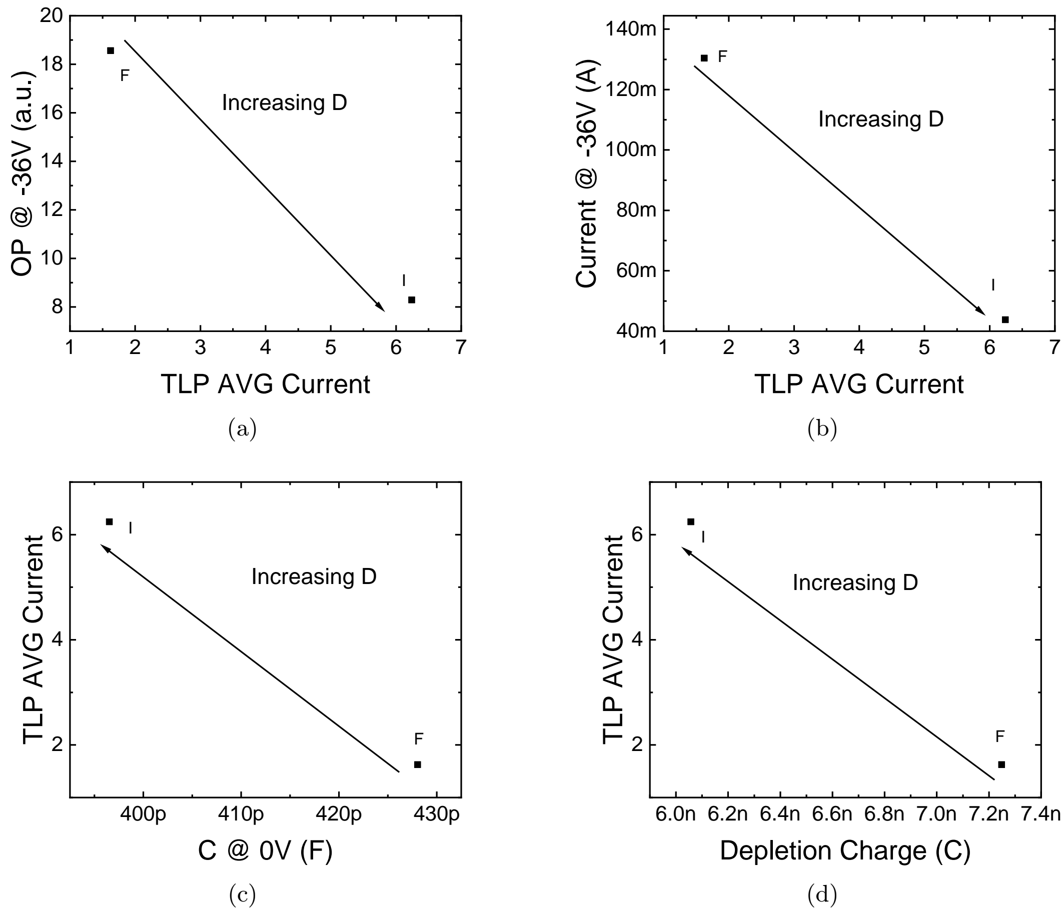

Figure 3.10: Correlations among device characteristics carried out with DC and pulsed measurements: families F and I.

Parameter D

The interesting samples for the study of the effect of the parameter D belong to the F and I families. The values of the analyzed parameters are reported in the following table.

Sample	Par. C	Par. D	Par. E
F	2.8	1	2.8
I	2.8	2	2.8

In this case, the role of the D parameter is to improve the robustness to ESD discharges when its value is higher (figure 3.9). Moreover, the device with the lowest value of D demonstrate a lower leakage current and lower electro-luminescence when submitted to reverse bias, which is possibly ascribed to the role of the D parameter in the limitation of the defect density.

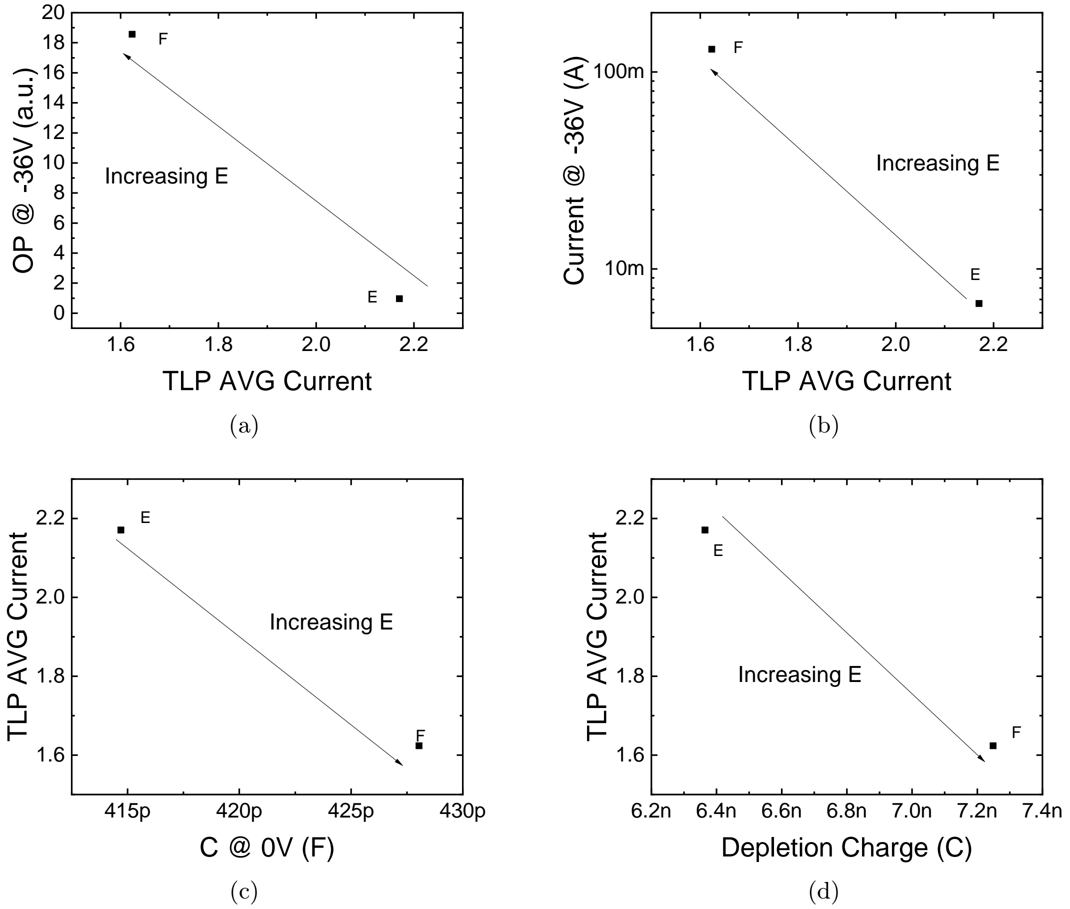

Figure 3.11: Correlations among device characteristics carried out with DC and pulsed measurements: families F and E.

Parameter E

Two sets of samples are interesting for the study of the effects of the parameter E. The first set includes samples E and F, which correlations are reported in figure 3.11: a higher parameter E is related to less ESD robust device, less leakage current and less electro-luminescence in reverse bias conditions. The reduction of reverse leakage current and electro-luminescence signal could be ascribed to the reduction of the defect density, related to the increase of the analyzed parameter. The increase of the same growth parameter is also related to a depletion charge and device capacitance increase.

Sample	Par. C	Par. D	Par. E
F	2.8	1	2.8
E	2.8	1	2

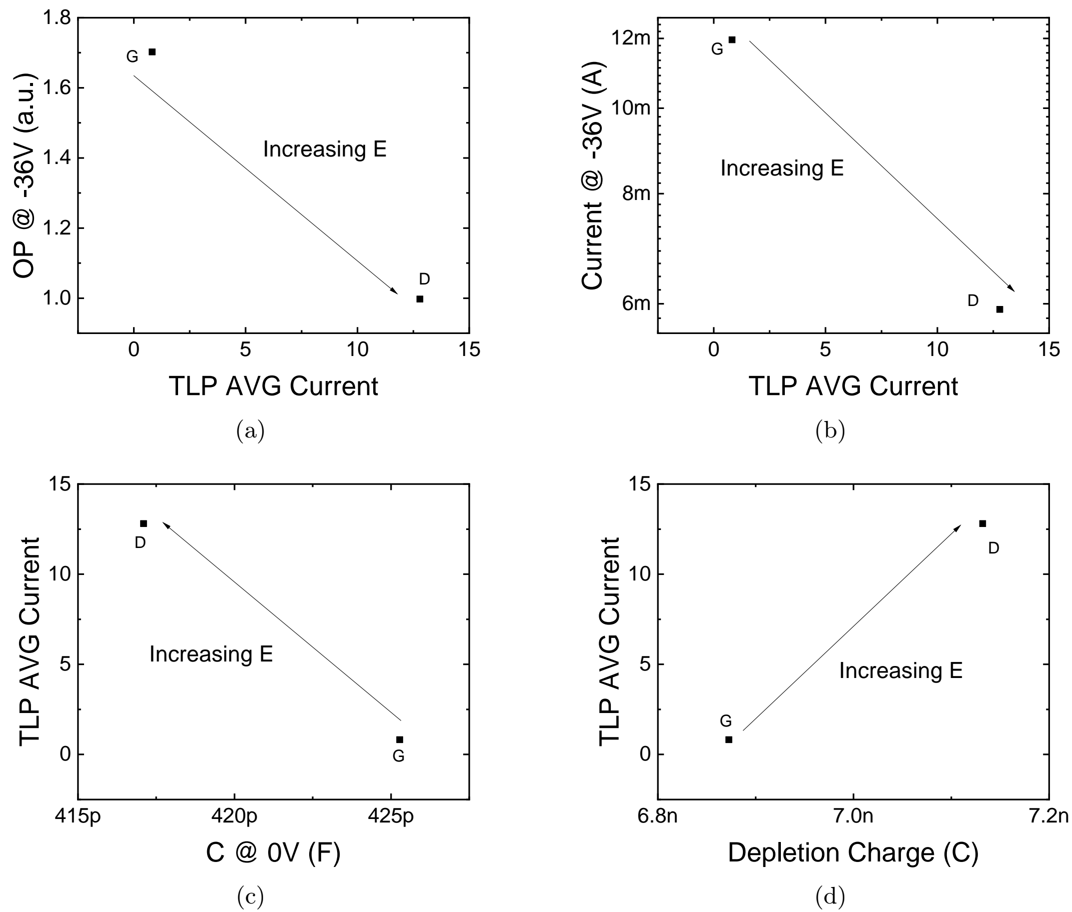

(a) (b) (c) (d)

Figure 3.12: Correlations among device characteristics carried out with DC and pulsed measurements: families D and G.

Also the samples D and G are useful for the analysis of this growth parameter, which characteristics are summarized in figure 3.12. Contrary to the previous case (when D=2.8), parameter E increase is correlated to ESD robustness and leakier and emitting samples in reverse bias conditions. This suggests that also the other parameters impact on the measured characteristics. The increase of this parameter is also related to a depletion charge increase (like in the D=2.8 case).

Sample	Par. C	Par. D	Par. E
D	4	1	2
G	4	1	0.8

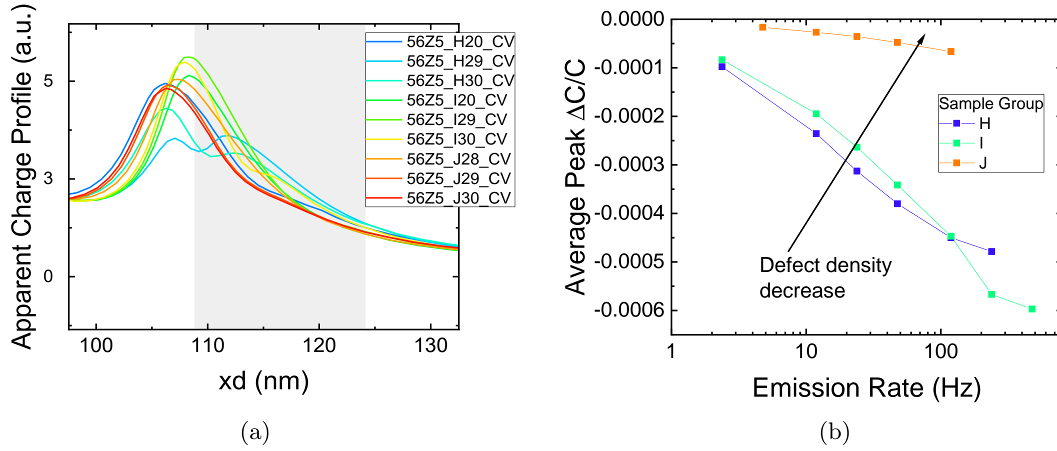

Figure 3.13: (a) Apparent charge profiles of the analyzed samples. The grayed region highlight the DLTS investigated region expressed in nanometers. (b) Defect density over the analyzed time range of the different families.

3.2.2 Capacitance DLTS characterization

Capacitance DLTS characterizations were carried out on the devices belonging to the families compared in the previous section to analyze the role of the defects present in the semiconductor material. In order to achieve a higher statistical significance, three samples for every family were analyzed. Then, the DLTS data was post-elaborated to show in a quicker way the results: the peak corresponding to each emission rate (i.e. the amount of defects which de-traps with that emission rate) is averaged with the same peaks of the other samples of the same family. Different families were tested keeping constant the depleted region explored (looking to the N-xd profile), by varying the applied voltages.

Parameter C

The first C-varying set of samples analyzed in this section are the families H, I and J, which have the C parameter equal to 2.4, 2.8 and 4, respectively. The results of the analysis are reported in figure 3.13: all the samples were investigated in the very same region, according to data reported in 3.13a. Defect density significantly decreases with the increase of parameter C: J sample is noticeably detached by the H and I samples and close to the detection limit of the DLTS system (figure 3.13b). Lower DLTS signal confirms the lower defect concentration, related to a lower reverse leakage current and to a higher ESD robustness.

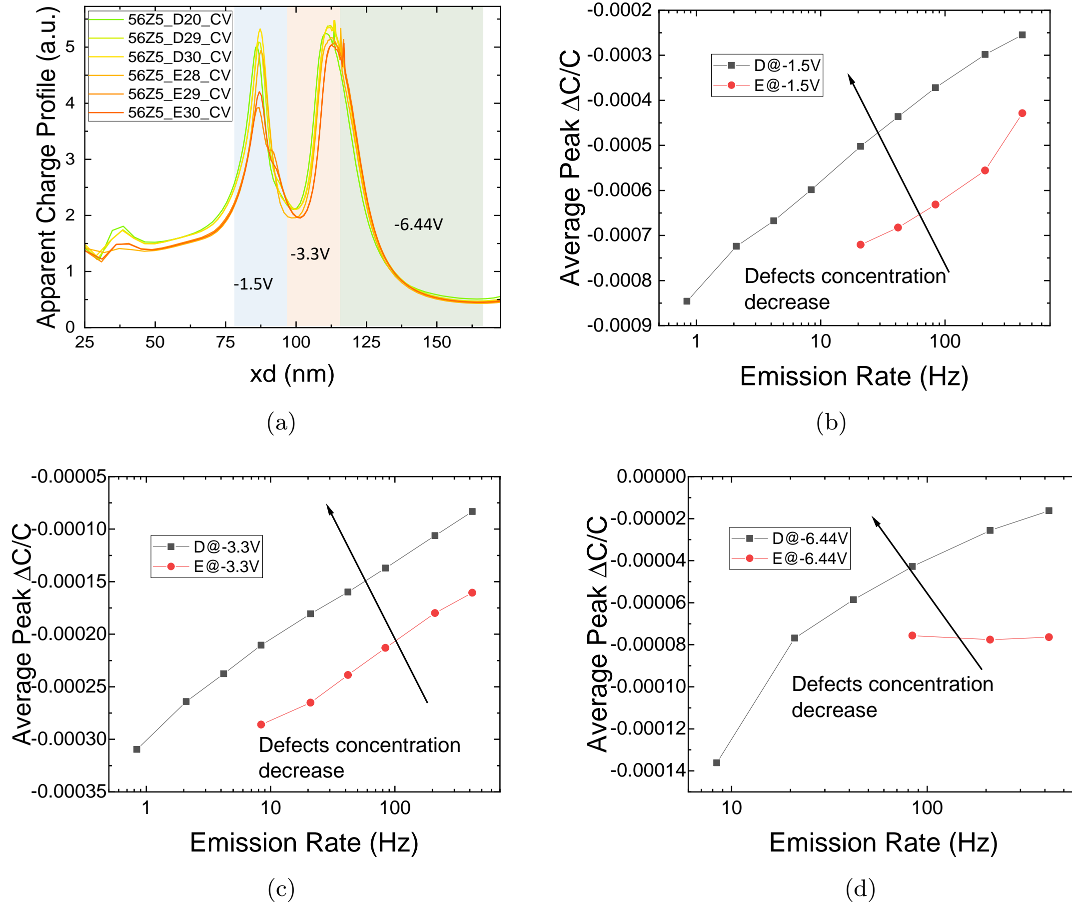

Figure 3.14: (a) Apparent charge profiles of the analyzed samples. The different investigated DLTS region are highlight with different colors. (b) $V_{fill} = -1.5V$. (c) $V_{fill} = -3.3V$. (c) $V_{fill} = -6.44V$.

Similar results can be noticed in the comparison of families D and E, in which the parameter C is varying: higher values of this growth parameter are related to a lower DLTS signal, suggesting the lower presence of defects in the epitaxial structure, a lower reverse current leakage and a higher robustness to ESD events. Such conclusions are confirmed in all the three investigated regions reported in figure 3.14.

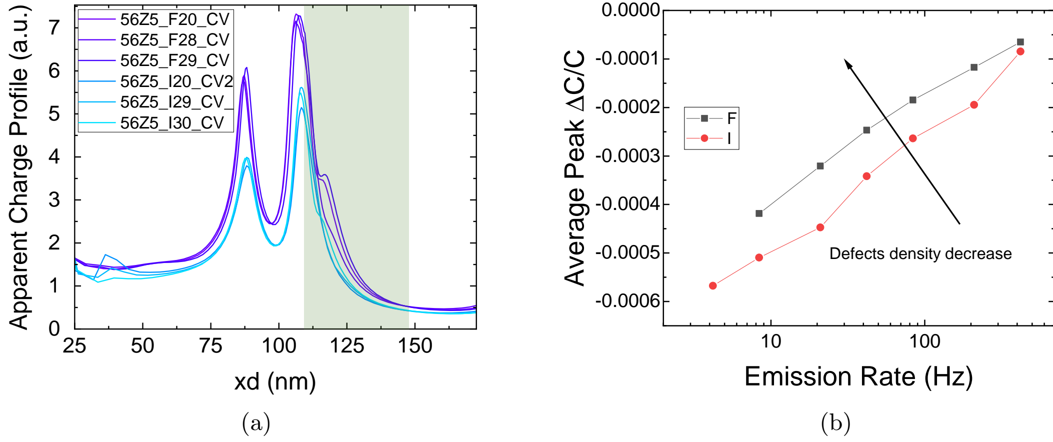

Figure 3.15: (a) Apparent charge profiles of the analyzed samples. The grayed region highlight the DLTS investigated region expressed in nanometers. (b) Defect density over the analyzed time range of the different families.

Parameter D

The only families useful for the study of the impact of the D parameter are F and I, where that parameter values 1 and 2, respectively. Results from the DLTS characterization are reported in figure 3.15: in this case, the impact of a higher growth parameter is still related to a higher robustness to ESD events, but the defect density is now enhanced by that.

Parameter E

The third growth parameter analyzed in this work is the E: families D and G have values of 2 and 0.8, respectively. DLTS results are reported in figure 3.16: in this case, the role of the E parameter is to reduce the defect density when it is higher, resulting also in a stronger robustness to ESD events.

Also the families E and F are useful for the investigation of the impact of parameter E on the epitaxial structure. The value of the growth parameter is 2 for E and 2.8 for F series. Results are reported in figure 3.17: in this case, the lowest is the E parameter and higher is the robustness to ESD events.

This opposite behavior can be ascribed the different impact of the parameter C on those families. In fact, among the families (D, G) and (E, F) the value of C is not constant. According to the value of C, the E increase induces opposite impacts on the robustness of the device. Moreover, the difference in ESD robustness in the C=2.8 case is less pronounced than the C=4 case.

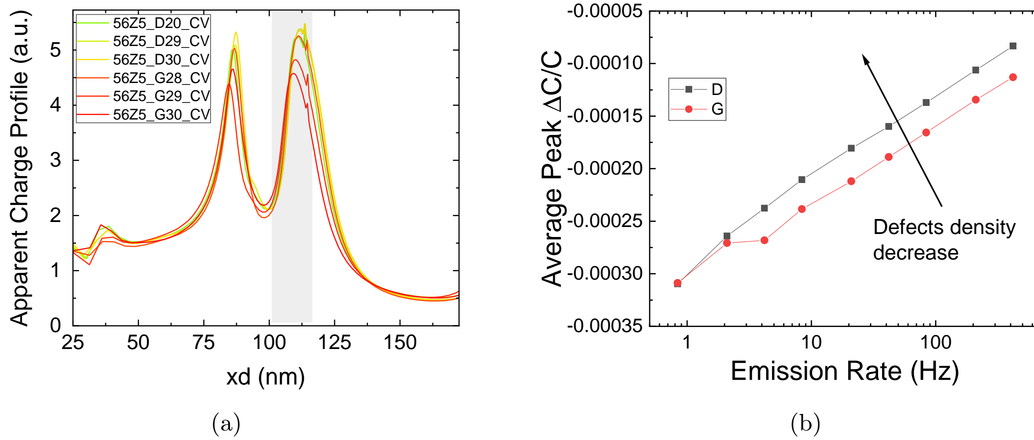

Figure 3.16: (a) Apparent charge profiles of the analyzed samples. The grayed region highlight the DLTS investigated region expressed in nanometers. (b) Defect density over the analyzed time range of the different families.

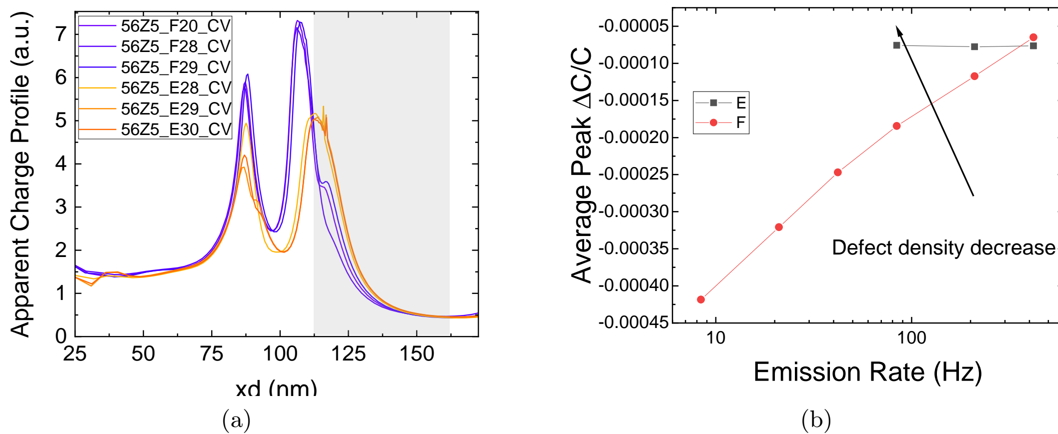

Figure 3.17: (a) Apparent charge profiles of the analyzed samples. The grayed region highlight the DLTS investigated region expressed in nanometers. (b) Defect density over the analyzed time range of the different families.

3.2.3 Global comparison

All the results about leakage current, defect density and ESD robustness are here grouped in the following table.

Parameter	defect density	Leakage current	ESD robustness
Higher C	Less	Less	More
Higher D	More	Less	More
Higher E (C=2.8)	More	More	Less
Higher E (C=4)	Less	Less	More

The differences among the roles of the analyzed parameters is here more evident: in general, the increase of the growth parameters within the analyzed range is related to more robust LEDs and less leakage current in reverse bias. Less evident is the correlation with the defect density, which could be ascribed to the fact that defects identified by DLTS characterization are not the only ones responsible for the leakage conduction in reverse bias nor for the ESD robustness.

3.2.4 Arrhenius analysis of identified defects

The deep levels detected with DLTS measurement were analyzed with Arrhenius analysis, detecting activation energies of traps and comparing them with the data available in the scientific literature. The results are summarized in the following table: according to the literature, the defects seem correlated mainly to nitrogen atoms.

Paper author	Paper	Physical origin
Kindl	[55]	Point defects
Shmidt	[52]	Unknown
Osaka	[53]	N-related point defects or antisite N
Zhang	[56]	Unclear
Arehart	[50]	Impurities or dislocation-point defects
Johnstone	[57]	Unknown
Hacke	[58]	N-related defects
Arehart	[59]	Intrinsic N-related defects
Wang	[60]	Native defect in GaN

3.3 Closing remarks

In this chapter, an extensive analysis aimed to correlate the epitaxial growth parameters and LEDs ESD robustness was presented. The analysis investigated separately the roles of the epitaxial features on the n- and p-side by means of DC and pulsed characterizations and Deep Level Transient Spectroscopy technique. Due to the confidentiality of the presented data, the nature of the growth parameters and their actual values were not specified.

The results about the investigation on the n-side suggest the strong importance of the parameter A (when B=0) in the robustness to ESD events, as reported in figures 3.2e and -f, where the sample with the highest value of this growth parameter is the most robust among all the devices tested (with n-side variations). The very same sample is also the one with the highest reverse leakage current, suggesting that the defects involved in the reverse conduction are not critical for the robustness to ESD events.

On the other hand, the parameter B increase is related to less robust and leakier devices, as demonstrated by the pulsed IV reported in figure 3.1b. This behavior could be ascribed to the higher concentration of defects in the structure and to the related weakness to reverse ESD discharges. In order to clarify the role of these defects, capacitance DLTS measurements were carried out on the B-varying samples: deep levels were detected only on the samples with higher B (see figure 3.4). Arrhenius analysis suggested that C-DLTS is might detecting shallow traps related to In-containing superlattice, rather than a defect. Then, optical DLTS measurements were carried out to identify defects located at deeper energies: as reported in 3.5, the strongest sample (with the lowest B) is also the sample with the highest traps density, suggesting that defect density in the QWs region is not critical for the robustness of those devices to ESD discharges. In figure 3.6, the comparison of those defects with the data available in the literature suggests the role of nitrogen vacancies as physical cause of them.

The investigation on the p-side suggests the strong importance of the parameter C in the improvement of the robustness to ESD events, as reported by the correlations in figures 3.7a and -b. Spatially resolved electro-luminescence measurements on these samples reveal that leakage paths in the epitaxial structure could limit the robustness to ESD events. In figure 3.8 the most uniform and the least bright sample is the one with the highest C parameter: the leakage paths that act as radiative recombination sites in reverse bias conditions could be responsible for the failure of the device, via shorting of the junction. The same behavior can be identified in the second set of C-varying samples (see figure 3.9), in which leakage paths may act also as non-radiative recombination sites. C-DLTS characterizations on those samples in figures 3.13 and 3.14 confirm the impact of C parameter in the reduction of defect density in the epitaxial structure.

Also the parameter D has a significant impact on the robustness to ESD events, but limited if compared to the C one. The increase of D parameter is still related to the improvement of the LED robustness, as displayed by the pulsed characterization in figures 3.10, but according to the C-DLTS results in figure 3.15 it is also related to a higher density of defects, which are

possibly not critical for the global structure robustness.

The last analyzed parameter, E one, has a limited impact on the ESD robustness of devices and its role is strongly related to the value of parameter C. The very same pulsed characterizations reported in figures 3.11 and 3.12 show different results, according to the value of C: in the first case, when C = 2.8, higher E is related to less ESD robustness, whereas in the second one, when C = 4, the opposite. The same happens looking at the C-DLTS data in figures 3.16 and 3.17: according to the value of C, the defect density is different, but the most robust devices still remain the ones with a lower defect density.

The comparison with literature of C-DLTS identified traps suggest that nitrogen atoms may play a role as physical cause of those defects.

In the following table are reported the significance of the impact of the different growth parameters on the robustness to ESD events and which value, within the analyzed range, is the best one to ensure device robustness.

Region	Parameter	Significance	Best Value
n-side	A	High	High
n-side	B	Medium	Low
p-side	C	High	High
p-side	D	Medium	High
p-side	E	Low	High

Chapter 4

Failure limits and electro-optical characteristics of GaN-based LEDs under electrical overstress

This work presents the analysis of the degradation mechanisms and of the electro-optical characteristics of light emitting diodes (LEDs) submitted to electrical overstress. The analysis was carried out by a custom-setup, that allows us to measure the current-voltage (I-V) and electro-luminescence curves of the devices while pulsing the devices with increasing voltages, up to failure. The aim of this work is to analyze and characterize the degradation mechanisms induced by the extremely high current densities reached during the EOS events, through specific experimental setups and procedures. We investigate a) the dependence of failure current/power on pulse duration, b) the dependence of the electrical characteristics on temperature, and c) the optical characteristics of the devices under overstress conditions, by presenting original data on the topic.

The results provide information on (i) the dependence of failure voltage/power level on pulse duration; (ii) on the temperature-dependence of the pulsed I-V characteristics; and (iii) on the changes in electrical and optical properties reached at extremely high current densities. The results presented within this work provide relevant information on the characteristics of the devices in this extremely high stress regime.

The relevant outcomes of this work were published in the paper “Failure limits and electro-optical characteristics of GaN-based LEDs under electrical overstress” on the scientific journal *Microelectronics Reliability* in 2018, reference [26].

4.1 Experimental details

The devices studied in this work are commercial low-power blue surface mount device (SMD) LEDs: the LED structure consists of a vertical epitaxial structure, with InGaN quantum wells and dominant wavelength at 470 nm. In order to achieve the best statistical significance, all

the devices analyzed in this work belong to the same production lot.

The devices, which have a nominal operating current of 30 mA and a chip-area of 2.3×10-4 cm2, were submitted to a pulsed forward I-V characterization until failure is reached. The experiment was performed by using a custom setup capable of generating pulses up to 2 A. The setup is based on a commercial high power pulser (HP8114A) as power source, and on a 500 MHz 2-channel oscilloscope to record the voltage and current waveforms. To measure the current waveform, a small resistor was placed in series to the device under test: measuring the voltage drop across the resistor we were able to calculate the amount of current that was flowing through the sample. As result, the waveform data were collected with a 4-wire configuration. Different pulse widths were exploited to carry out the pulsed current voltage (I-V) characterizations, while keeping constant the duty cycle, fixed at 0.5%. For the 10 s pulse, a DC source-meter was used. The electrical characteristics were measured at room temperature (RT), of 25 °C.

To achieve a deeper understanding of the degradation mechanisms, further experiments were carried out. Several pulsed I-V characterizations were performed by varying the sample temperature, using a Peltier cell and a temperature controller. Moreover, a camera equipped with a cooled charge-coupled device (CCD) sensor was used to carry out spatially resolved electroluminescence analysis. Optical spectroscopy measurements were performed with a compact array spectrometer.

4.2 Failure modes analysis

The graph in 4.1a shows the results of pulsed I-V characterization, performed at five different pulse widths, from 1 ms to 10 s. The electrical quantities are extrapolated from the current and voltage waveforms acquired during the pulse. The values reported into the graphs are calculated as average of the current and voltage values into the measurement window (M.W.). In order to avoid the possible ringing and achieve a strong repeatability, the measurement windows are placed over the last portion of each pulse, in which the waveform is in the most stable condition (see 4.1b). As result, voltage and current readings are influenced by device self-heating during the pulse. As shown in 4.1b, the voltage waveforms of the three shortest pulse widths overlap, confirming that the LED voltage drop during the pulse is related to the lattice temperature increase. Therefore, due to the strong self-heating, the LED operating and failure voltages drops at the longest pulse widths, inducing the leftwards shift of the IV curves and a decrease in the failure voltage.

To support this hypothesis, the 4.1c displays the pulsed IVs obtained by the same device, but placing the measurement window at the beginning of the waveform. In this case, the measure is not influenced by the device self-heating and, as result, the IV curves are overlapped. Moreover, in absence of significant thermal effects, the behavior of the pulsed IV is almost linear. Therefore, for high but non-destructive current densities the sample acts as an equivalent resistor: this is in agreement with diode theory, where conduction is dominated

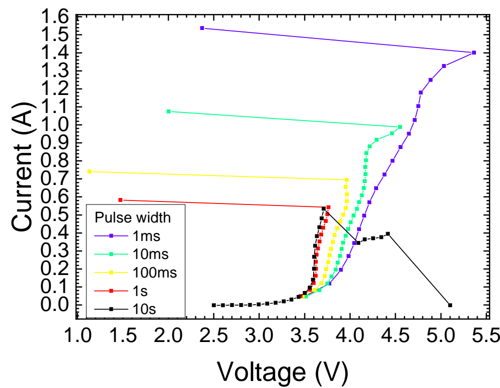

(a) *Pulsed I-V characterization carried out with different pulsed widths, but same duty cycle.*

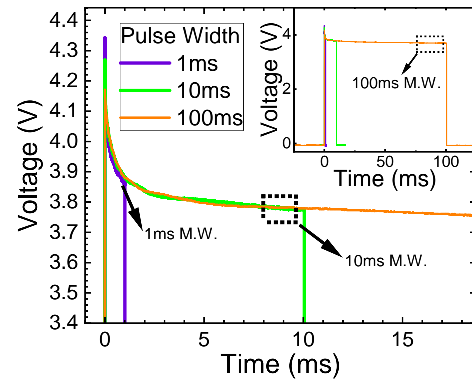

(b) *Voltage waveforms of three different pulses with the shortest pulse widths. 1s and 10s pulses are not displayed because the samples do not reach this voltage range. Measurement windows (M.W.) are chosen at the end of every pulse.*

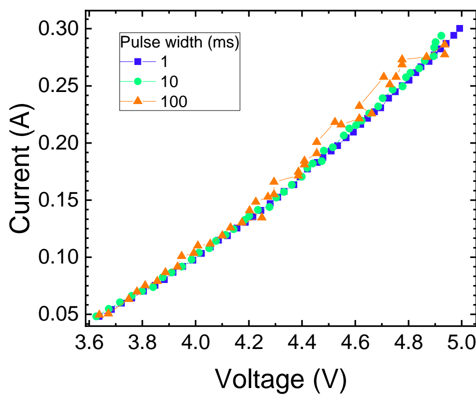

(c) *Pulsed I-V characterization calculated with the measurement window placed at the beginning of the pulse. 1s and 10s curves are not displayed because the samples reached the failure before covering the whole voltage range.*

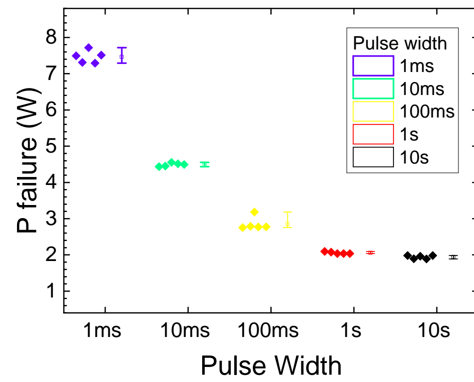

(d) *Statistical distribution of the failure power at the analyzed pulse widths, five sample for every pulse width.*

Figure 4.1: Pulsed current-voltage characteristics of GaN based LEDs in forward bias condition and statistical description of the failure points. [26].

by resistive effects for extremely high current levels (these devices are rated for 30 mA max, therefore currents above 50-100 mA are extremely high).

The statistical description of the failure events is reported in the 4.1d. Five samples for every pulse width were characterized, maintaining constant the duty cycle at 0.5%. As predicted by the comparison in 4.1a, by increasing pulse width from 1 ms to 10 s a significant drop in the power to failure value is observed. This suggests that the failure event is enhanced by the temperature of the sample: due to the strong self-heating, the power dissipation required to reach the failure condition is less if the biasing time is longer. Moreover, the pulse width increase is also related to different failure modes: for longer pulse width, a higher number of devices showed an open-like failure (see for instance the 10s IV in the 4.1a). This can be ascribed to the amount of energy delivered to the sample, which is able to induce damages to the package, such as the melting of the bonding wire and of the encapsulant. On the other hand, for shorter pulse widths, a short-like failure was found to dominate, indicating a damage of the chip.

4.3 Temperature varying and spectral analysis

To achieve a deeper understanding, further experiments were performed, in which the pulse width was fixed at 1 ms. Consecutive non-destructive pulsed I-V characterizations, carried out on the same device, showed that no significant degradation is detected below the 1.2 A limit. For this reason, the temperature analysis reported in 4.2a was stopped before reaching that current value. By increasing temperature, the pulsed IV showed a leftwards shift (4.2a), that can be ascribed to the energy gap shrinking due to the temperature, because the Varshni's law, or to the temperature-related change of the diode saturation current. On the other hand, the slight slope change in the region below 4.2 V (4.2a) can be ascribed to a thermally-assisted conduction mechanism, which saturates at higher current densities. In fact, the slope in the region around 4.2V is the similar for all temperatures. The different behavior for voltages higher than 4.2 V can be noticed also in 4.2b, which describes the pseudo external quantum efficiency (EQE), calculated as optical power-current ratio. The change of slope suggests the onset of a dominant process at the higher current densities. Moreover, a global decrease of the pseudo EQE is detected as temperature increases. In agreement with the diode theory, this behavior can be ascribed to the enhancing of the non-radiative recombination promoted by the higher junction temperature.

In 4.2c we report the correlation between peak wavelength and pulsed IV and, in addition, the behavior of the peak optical power. The analysis of those curves allow us to define four different regions. In region A, self-heating is not dominant, as suggested by the fact that peak wavelength drops with increasing voltage. This phenomenon can be ascribed to the non-uniform band-filling and to the screening of the QCSE induced by the carrier density increase. Moreover, OP increases monotonically with current and voltage, suggesting that radiative recombination is dominating. For higher voltages (>4 V), also Auger recombination

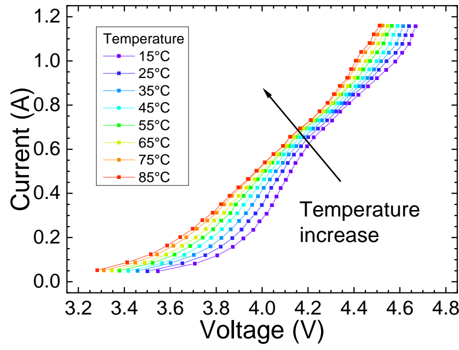

(a) *Pulsed I-V performed at different temperatures. The pulse width is 1ms.*

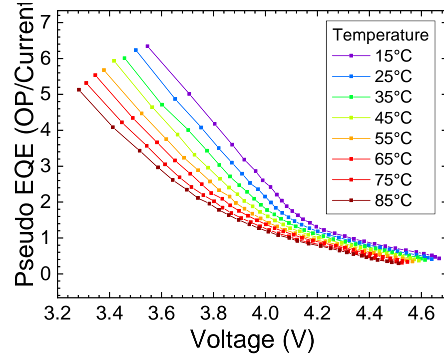

(b) *Pseudo external quantum efficiency (EQE) calculated as the optical power-injected current rough ratio. The graph describes the behavior of the device pulse mode (pulse width = 1 ms).*

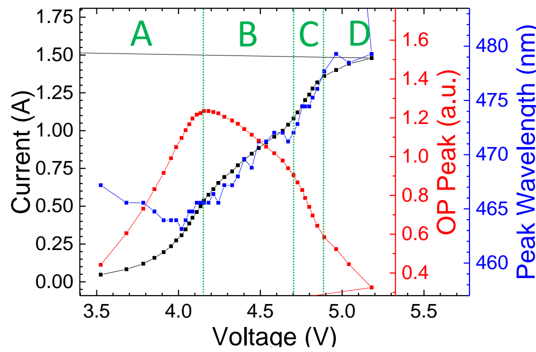

(c) *Peak wavelength and peak optical power measured during the pulsed I-V characterization. The correlation between the electrical curve and the wavelength one suggests the strong role of temperature in the device.*

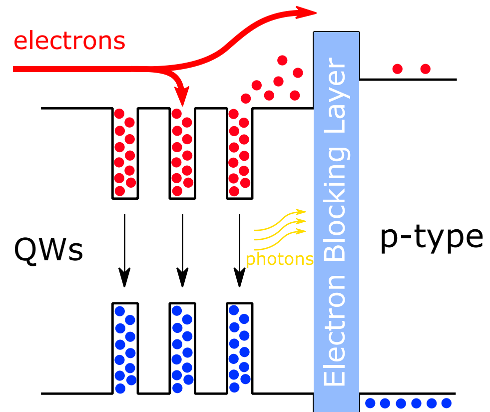

(d) *Example of the internal structure of a GaN based LED. For very high current densities, a condition of strong carrier overflow may occur, in which the electrons are able to reach the p-type region, going over the electron blocking layer. In this condition, the resulting equivalent resistance decreases due to the less resistive leakage path.*

Figure 4.2: Results of the electrical and optical characterizations carried out at different temperatures and interpretation of the degradation mechanisms that are taking place in the device. [26].

may play a role. In region B, the sudden decrease of the optical power suggests that the power dissipation starts to induce a strong self-heating. This hypothesis can be confirmed by the peak wavelength increase. In region C, an increase in the slopes of (increasing) current density and (decreasing) optical power is observed. Considering the very high current density, the behavior can be ascribed to the saturation of the QWs, which induces a strong overflow (see 4.2d). In this sense, a non-negligible portion of the injected electrons would be able to reach the electron blocking layer and, eventually, the space charge region on the p side. This further lowers the efficiency of the devices (OP decreases in region C), and may lead to additional power dissipation. In the last region D, the very high current density induces the current crowding effect (see 4.3a). The current crowding effect is related to the localized power dissipation around the injection point, which leads to a progressive decay of the optical properties of the device, especially to the global optical power and the carrier distribution. The uniformity drop displayed in the 4.3a can be ascribed to the formation of leakage paths, which act like non-radiative recombination centers, under the anode pad [61]. This is compatible with the resistance decrease detected in the last pulses. Finally, the catastrophic failure of the device is reached. An additional consideration can be deduced by the spectra in the 4.3b: another source of emission can be noticed around the 400 nm. This emission, taking place only at extremely high current densities, can be ascribed to electrons overflowing the electron blocking layer, reaching the p-side of the junction, and recombining at donor-acceptor pairs in the p-type layer [62, 63].

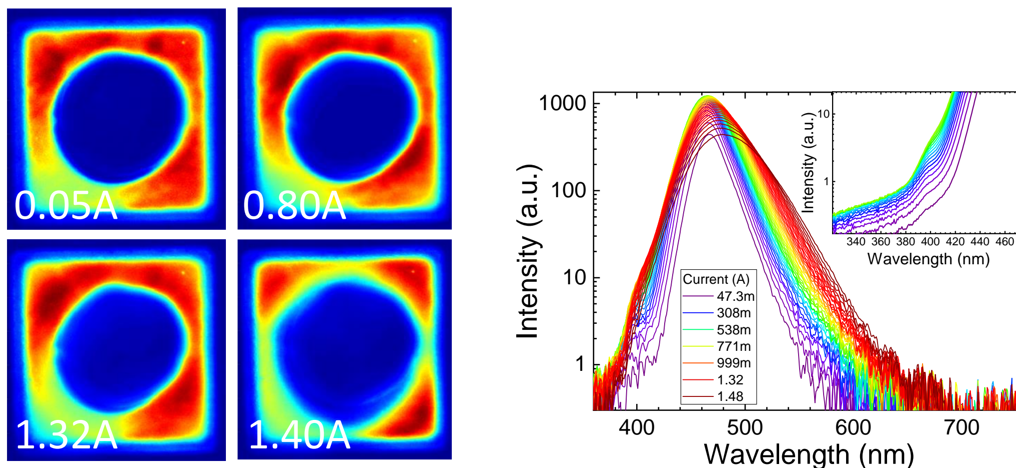

(a) *Spatially resolved electro-luminescence images of the tested device with pulse width = 1 ms, normalized. The analysis exhibits the current crowding effect induced by the extremely high current densities reached during the EOS event.*

(b) *Spectra of the analyzed device (pulse width = 1 ms). In the inset, the emission at 400nm can be noticed.*

Figure 4.3: Results of the spatially resolved and spectrally resolved optical characterizations. [26].

4.4 Conclusions

In this work, the degradation mechanisms induced by extremely high current densities on GaN based LEDs were analyzed. By using a custom setup, we were able to investigate the dependence of failure power level on pulse width, the impact of temperature on the pulsed characteristics of the devices, and the correlation between electrical and optical parameters with increasing current level until failure.

The statistical description of the failure events suggest that they are enhanced by the temperature of the sample: due to the strong self-heating, the power dissipation required to reach the failure condition is less if the biasing time is longer, leading to open-like failures (package-related) for the longest pulse width. Further experiments at high current densities identified a thermally-assisted conduction mechanism and, by the estimation of the external quantum efficiency, the enhancing of the non-radiative recombination promoted by the high junction temperature.

The comparison of electrical and optical characteristics during the EOS stress tests allow us to define four different regions:

- *region A* radiative recombination is dominating and non-uniform band-filling can be detected
- *region B* strong self-heating can be noticed due to the peak wavelength increase
- *region C* the saturation of the QWs induces a strong overflow and may lead to additional power dissipation
- *region D* the very high current density induces the current crowding effect, leading to a progressive decay of the optical properties of the device due to to the formation of leakage paths under the anode pad.

The detection of optical emission around the 400 nm can be ascribed to electrons overflowing the electron blocking layer, reaching the p-side of the junction.

Chapter 5

Evidence for avalanche generation in reverse-biased InGaN LEDs

Avalanche generation is a physical mechanism responsible for the breakdown at extremely high field, such as in the reverse bias conditions typical of ESD discharges. In this part is presented the experimental evidence that avalanche generation can take place in state-of-the-art InGaN-based blue LEDs. We measured the current-voltage and electro-luminescence curves of the devices while pulsing them with increasing reverse voltages. We investigated a wide span of temperatures (from cryogenic to room temperature) in order to verify that the increase in leakage current detected below -80 V is related to avalanche generation (positive temperature-coefficient). Numerical simulations show that in this bias condition the band-to-band tunneling barrier thickness is low, leading to the possible injection of highly-energetic electrons from the p-side to the n-side that can start the avalanche process.

The relevant outcomes of this work were presented to the conference *Photonics West 2019* and included in the conference proceedings with the title "Evidence for avalanche generation in reverse-biased InGaN LEDs", reference [27].

5.1 Introduction

Impact-ionization is a three-particle generation process in which carriers gain high energies, while traveling through high field regions, and undergo scattering events with bonded electrons in the valence band. The excess energy is transferred to this electron, which is lifted into the conduction band creating a new electron-hole pair. This secondary electron-hole pair can also have a rather high energy. In this case the *avalanche effect* can be triggered and the carrier density increases heavily.

This process is exploited in avalanche p-i-n diodes, by which a small optical signal (an absorbed photon) is amplified before entering an external electronic circuit. In fact, before the signal is given to the receiver circuitry, the photon is multiplied with the photocurrent, increasing the sensitivity of the receiver. In this way, photocurrent is multiplied before en-

countering of the thermal noise associated with the receiver circuit.

In a simple p-n junction, like a Schottky diode, impact ionization can be obtained under strong reverse-bias conditions: in this case high-energy carriers impact-ionize atoms of the semiconductor, possibly triggering the avalanche generation. In this process, holes are created in the valence band as well as electrons in the conduction band, which will eventually recombine thereby creating light.

In this work, the aforementioned phenomenon is observed and analyzed, for the first time, in an high-power state-of-the-art GaN-based LED by means of a custom experimental setup able to emulate ESD events.

5.2 Experimental details

The devices studied in this work are state of the art high power blue LEDs: the device structure consists in a vertical epitaxial structure, with InGaN quantum wells. The devices were submitted to pulsed reverse bias, in order to detect the conduction mechanisms responsible for the leakage in high reverse bias conditions.

The electrical characterization was carried out with a custom high power pulser based on a capacitor and high power MOSFET. In this setup, the capacitor is pre-charged by a power supply, then a micro-controller enables the MOSFET, allowing the discharge of the capacitance through the device under test. The voltage and current waveforms are recorded by two differential voltage probes, connected to a 500 MHz 2-channel oscilloscope. To measure the current waveform, a small resistor was placed in series to the device under test: measuring the voltage drop across the resistor we were able to calculate the amount of current that was flowing through the sample. As result, the waveform data were collected with a 4-wire configuration.

For the optical characterization, a high sensitivity optical spectrometer (model CAS140 – Instrument Systems) was used. In order to obtain a better comparison among different electro-luminescence spectra, a current pulser (model 6221 – Keithley) was used.

All the measurements were performed at controlled temperature, into an open-loop cryostat.

5.3 Electrical characterization

The graphs in 5.1a and 5.1b show the results of the pulsed current-voltage characterization (IV), performed with $1\mu s$ pulse width. The electrical quantities are extrapolated from the current and voltage waveforms acquired during the pulse. The values reported into the graphs are calculated as average of the current and voltage values into a specific portion of the waveform, defined as measurement window (MW). In order to avoid the possible ringing and achieve a strong repeatability, the measurement windows are placed over the last portion of each pulse, in which the waveform is in the most stable condition.

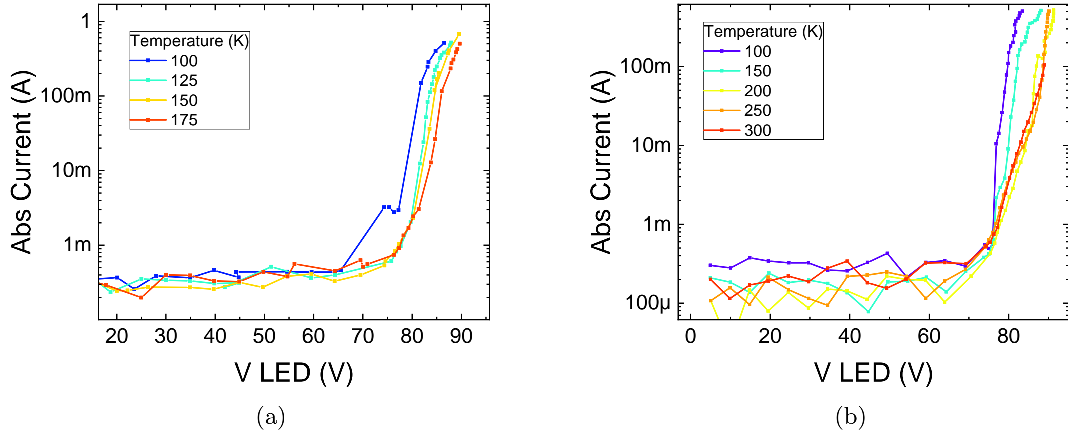

Figure 5.1: Pulsed current-voltage characteristic of a GaN based blue LED in reverse bias condition. (a) The leakage current increases dramatically below -80V: the right-shift in the IV suggests the impact of avalanche generation. (b) The overlap in the curves between 200 and 300K suggests the presence of a competing conduction mechanism, which limits the impact of the avalanche generation [64].

The magnitude of the leakage current until -80V is below the noise floor. For stronger reverse bias conditions, leakage current increases significantly. This behavior can be ascribed to band to band tunneling which is triggered by the extremely high electric field, becoming the dominant conduction mechanisms at such reverse voltages [65]. Moreover, the rightward shift in the IV curves below -80V with the increasing temperature suggests that also avalanche generation plays a role [28]: being the impact ionization strongly dependent on the mean free path, a higher temperature of the device is able to limit it, inducing the right-shift in the IV. In fact, in the drift-diffusion model, the impact-ionization rate is usually expressed using the impact-ionization coefficients α_n and α_p . These two coefficients describe the number of electron-hole pairs generated per unit distance traveled [66] by a solitary carrier between two collisions. Considering only electrons generated by electrons, one can write

$$\alpha_n = \frac{1}{n}\frac{dn}{d(t\nu_n)} = \frac{1}{n\nu_n}\frac{dn}{dt} \tag{5.1}$$

where ν_n is the carrier velocity, n is the electron concentration and $dn/d(t\nu_n)$ is the generated carriers per distance. According to the work of Chynoweth [67], the same coefficient can be written as

$$\alpha_n = A_n \exp\left(-\frac{B_n}{E}\right) \tag{5.2}$$

where A_n and B_n are parameters. The temperature dependence of the impact ionization can found with the latter parameter (see [68]), because B_n can be rewritten as

$$B_n(T) = C_n + D_nT. \tag{5.3}$$

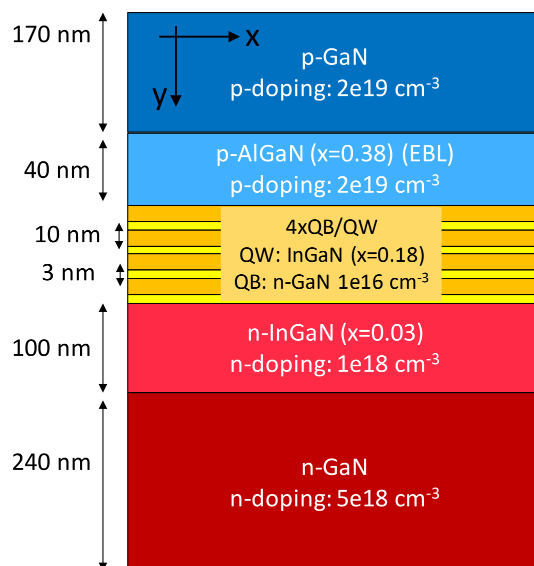

Figure 5.2: Simplified structure of a GaN-based LED. The epitaxial stack is not identical to the real device but it's used here for the purpose of simulation.

In this way, an increase of temperature induces the B_n parameter increase, limiting the effect of the electric field on the impact ionization.

In 5.1b, the overlap of the curves above 200K suggests that another conduction mechanism may play a role, limiting the impact of avalanche generation.

A T-CAD simulation of the band diagram at -80V is reported in the 5.3: the simulated structure (reported in 5.2) is a simplified structure, not identical to real devices but used here for the purpose of simulation. The simulated structure is a vertical epitaxy, with n-GaN/QW region/p-GaN stack. The results suggest that, in such strong reverse bias condition, the estimated thickness for band-to-band tunneling is 6 nm. This result supports the interpretation mentioned above, about the band-to-band tunneling being triggered by extremely high electric field.

5.4 Optical characterization

The graph in 5.4 shows the electro-luminescence (EL) spectra of the device submitted at current pulses in reverse bias condition, at room temperature (25°C). The spectra are acquired over a wide range of currents and all of them are related to the avalanche region (voltage below -80V). The spectra overlap suggests that the physical origin of such photons is common to all the explored current levels. The graph in 5.5a show a comparison between the electro-luminescence of the device at -1mA and the emission of a Maxwellian source at 4000K, corrected with the absorption profiles of GaN. This comparison suggests that, on the high energy side (above 2.8 eV), the LED emission in reverse bias is compatible with a source that follows the Maxwell-Boltzmann statistics. The graph in 5.5b is focused instead, on the low

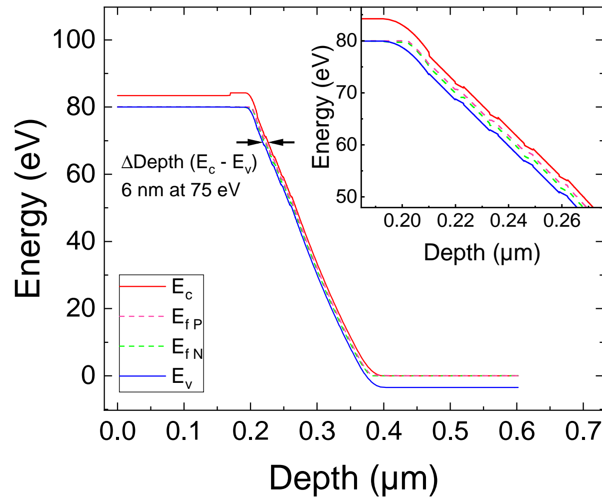

Figure 5.3: T-CAD simulation of a vertical epitaxial structure based on 4 InGaN/GaN quantum wells[64].

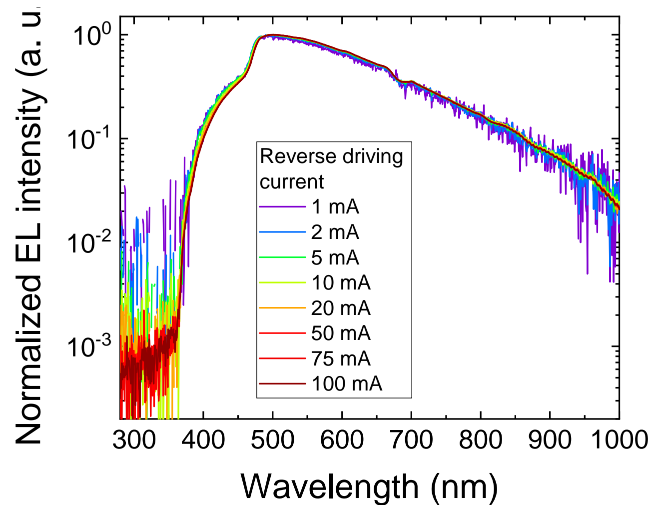

Figure 5.4: Electro-luminescence (EL) in pulsed reverse bias condition at various current levels taken at room temperature (25°C) [64].

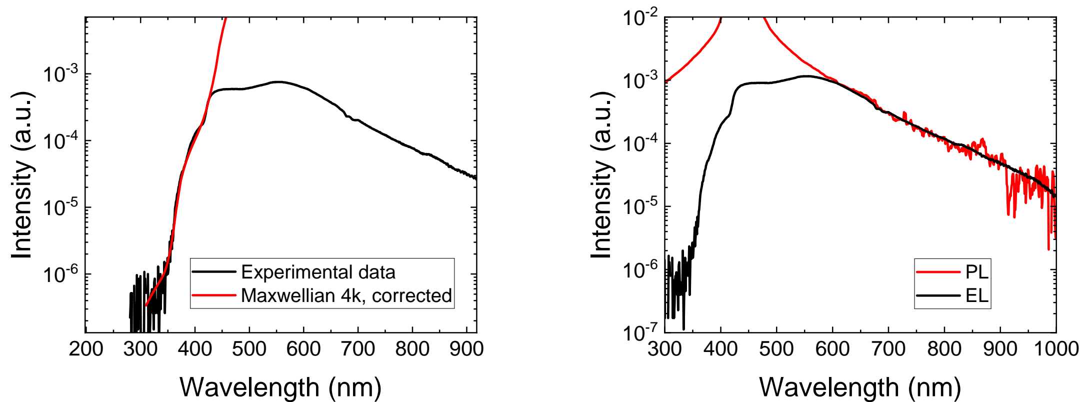

(a) *Comparison of the electro-luminescence LED spectrum submitted to reverse bias and the emission of a 4000K Maxwellian source.*

(b) *Comparison of the electro-luminescence LED spectrum submitted to reverse bias and the photo-luminescence of the same device under a 450nm photo-excitation.*

Figure 5.5: Modeling of the electro-luminescence LED spectrum [64].

energy side (below the 2.5 eV): this region is not compatible with Maxwellian emitter, but the spectral shape follows the photo-luminescence of the LED exposed to a 450nm source. The lack of low-energy emission from the Maxwellian distribution could be tentatively explained as follows: since we are in avalanche condition, we have a hole density equal to the electron density. As a consequence, the dominant process leading to the excitation of the deep levels could no longer be the relaxation of the highly-energetic electron to the edge of the conduction band, but the recombination of that electron with an hole in the valence band. Further analysis is needed to explain the region between 2.5 and 2.8 eV.

The interpretation of the experimental data can be seen in 5.6:

- hole and electron pairs generated by the avalanche process recombine radiatively, generating photons
- these photons are partially re-absorbed in the In-containing layers and n-GaN side, as confirmed by the red-shift at higher temperature (see the high energy side on the 5.4)
- that energy is re-emitted as internal photoluminescence of the yellow-emitting defects in the n-GaN layer, as suggested by PL measurements with external excitation.

5.5 Conclusion

In this work, the physical conduction mechanisms that occur in state-of-art GaN based LEDs submitted to extremely high reverse bias were analyzed. By using custom setups, we were able to investigate the temperature dependence of the current-voltage characteristics in pulsed reverse bias conditions, detecting a positive temperature coefficient, indicative of avalanche generation. A numerical simulation was proposed to support the presence of band-to-band

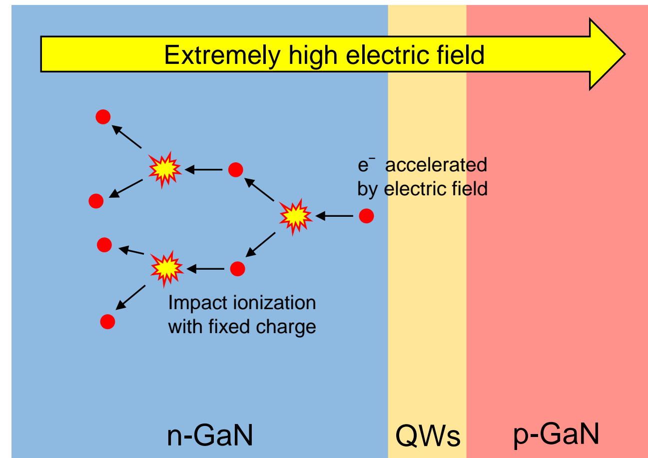

(a) *Phase I: Avalanche generation, due to extremely high electric field, generates hole-electron pairs.*

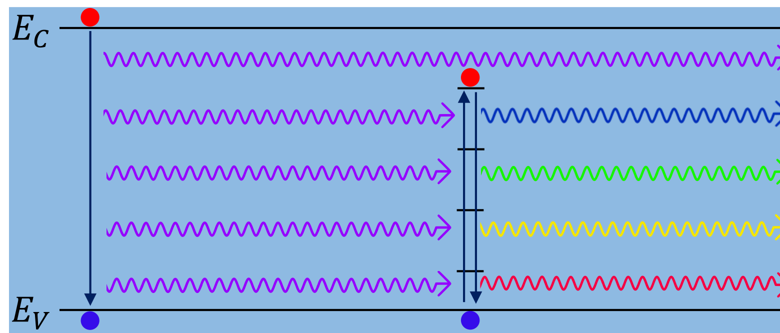

(b) *Phase II and III: Band-to-band radiative recombination of the hole-electron pairs, generated by avalanche generation, emits UV photons. Such photons are partially re-absorbed by QWs and deep levels and re-emitted with longer wavelengths.*

Figure 5.6: Interpretation of the observed phenomenon.

tunneling and the related impact ionization. By the spectral analysis of the electro- and photo-luminescence of the devices under test, an interpretation of the experimental data was proposed.

Chapter 6

Gradual degradation of color coded test structures

Commercially available GaN-based devices are typically designed to have from 3 to 5 quantum wells in their active region, because this amount of QWs allow to maximize the internal quantum efficiency. Moreover, all the QWs have the same energy gap and then emit photons with the same wavelength. Instead, the color coded devices are epitaxial vertical structures where the quantum wells are designed to have different energy gaps. In this way, the QW in which a particular photon was generated can be detected by analyzing the wavelength of that photon.

This type of structures, not commercially exploited, are very useful in research applications, because the contribution of every single QW can be analyzed performing a spectrally resolved optical characterization.

6.1 Experimental details

The epitaxial structure of the three different test devices are reported in figure 6.1: all the structures have two quantum wells, emitting at different wavelengths and a surface area of 500x500μm. The QW emitting at 495 nm is referred to as reference quantum well, since this is the one whose degradation is monitored during stress time. The QW emitting at 405 nm is referred to as secondary quantum well, and is used as a "placeholder" to ensure that the all the structures are fabricated in similar conditions (e.g. similar growth temperatures, similar indium contents). We chose not to use simple GaN in place of the secondary QW, since GaN and InGaN are grown at different temperatures, and it is known that growth temperature can significantly impact on radiative efficiency [69]. By doing so, we ensured the maximum similarity between the first two structures. In the structure A, the reference QW is located closer to the p-side, while in the structure B it is located closer to the n-side. Structure C is a variation of the A one, in which the Al density into the electron blocking layer (EBL) is lower compared to the A version, resulting in to a lower energy barrier defined by the EBL.

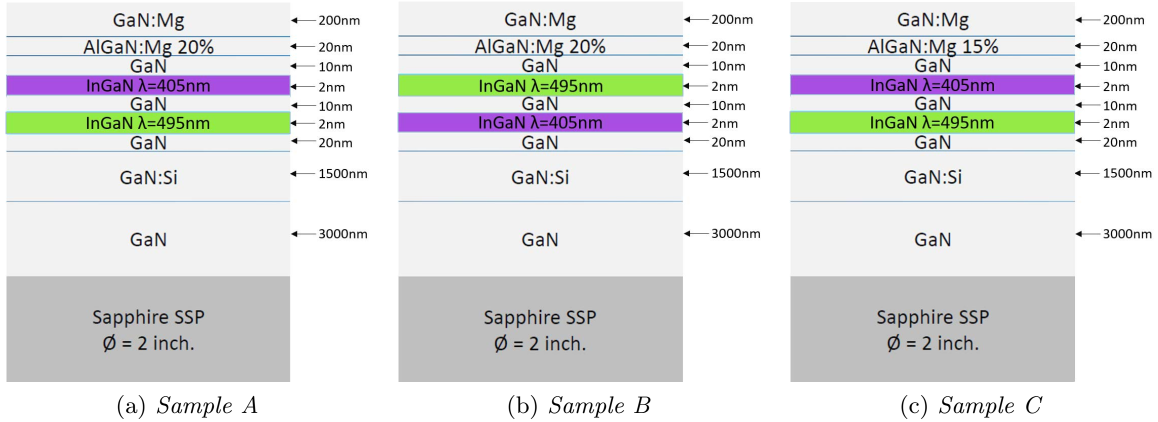

(a) *Sample A* (b) *Sample B* (c) *Sample C*

Figure 6.1: Epitaxial structure of the tested samples.

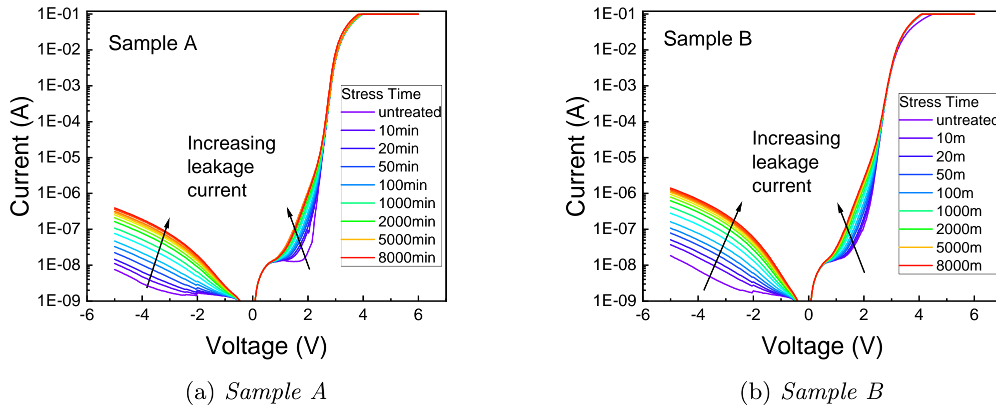

(a) *Sample A* (b) *Sample B*

Figure 6.2: IV characteristics measured during the constant current stress at 200mA.

The devices were submitted to constant current stress at 200 mA (80 A/cm^2), at room temperature. During stress, the electrical characteristics of the devices were monitored by means of high-sensitivity current-voltage (I-V) measurements, while the optical and spectral characteristics were analyzed by means of a compact array spectrometer (CAS). The effects of the gradual degradation will be analyzed separately, comparing samples A and B (different QW order) and then samples A and C (different EBL).

6.2 Structures A and B: different QWs order

The first comparison is related to the samples A and B, which differ in the order of the QWs. Figure 6.2 reports the current-voltage characteristics of the stressed devices collected before and during stress at 200 mA. As can be noticed, stress induced a significant increase in both reverse current and sub turn-on forward leakage (in the voltage range between 1 and 2.5 V). In both voltage ranges, conduction is mainly dominated by defect-assisted mechanisms.

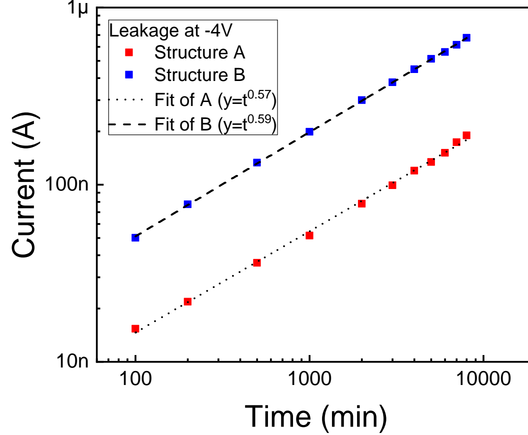

Figure 6.3: Change in the reverse leakage over time at -4V.

In the reverse-bias regime, hopping (either variable-range hopping, VRH, or nearest-neighbor hopping, NNH) typically dominates [70, 37, 71, 72]; the contribution of thermally-assisted multistep tunneling has also been proposed to contribute [37]. As a consequence, reverse conduction is strongly dependent on the density of defects within the depleted region or, equivalently, on the distance between neighboring traps. An analytical model was recently proposed in [71], according to which reverse leakage due to VRH and NNH can be expressed as:

$$J/F,T) \propto D_x exp\left(-\frac{4\sqrt{2m^*}\epsilon^{3/2}}{3qF\hbar}\right) exp\left[-\left(\frac{T_0}{T}\right)^V\right] \tag{6.1}$$

where D_x is the volume density of unoccupied states at point x, F is the maximum electric field in the depletion region and T_0 is the characteristic temperature. In the low forward bias regime (here between 1 and 2.5 V), conduction is mostly dominated by trap-assisted tunneling, as demonstrated by recent papers [73]. Also in this regime, the defect-mediated current is proportional to the density of defects, see for instance [74], where the following formula is proposed:

$$J \propto \frac{qN_T}{E} \int f(\phi) d\phi \tag{6.2}$$

where $f(\phi)$ is a function describing the shape and properties of the tunneling barrier. Moreover, a lower series resistance can be noticed in the sample A in the high forward bias region.

As shown in figure 6.3, during stress the reverse leakage of the devices showed a monotonic increase, indicating a gradual increase in the density of defects within the active region. Remarkably, reverse leakage increased with the square-root of stress time. Here the hypothesis is that the leakage increase is due to the increase in the defect density in the depleted region due to a diffusion process, in agreement with previous papers on laser diodes [75, 76, 77]. We suppose the existence of a defect concentration gradient from one of the doped layers (either n-type or p-type) to the intrinsic quantum well region: the high stress current densities may

promote the propagation of defects, from the region with high concentration towards the quantum wells. Once defects are generated, they can propagate according to the known diffusion equation:

$$N(z) = N_0 erfc\left(\frac{z}{2\sqrt{Dt}}\right) \tag{6.3}$$

where $N(z)$ is the defect density at position z (with respect to the concentration gradient), and D is the diffusion coefficient of the defect involved in the degradation process [75]. Possible diffusing defects may be hydrogen [78, 79, 80], hydrogen/oxygen vacancy complexes [81, 82], magnesium [83, 75, 84], or intrinsic defects as vacancy complexes [81, 85, 86].

Once they reach the quantum wells, the diffusing defects may act as SRH recombination centers, thus lowering the quantum efficiency of the devices. The non-radiative nature of the degradation process was confirmed by the optical measurements 6.4: optical power degradation was found to be present only in the low current regime (below 1 mA), i.e. in the current range where recombination efficiency is limited by SRH losses [87].

To understand if the diffusion process responsible for the degradation is initiated at the p-side or at the n-side of the diode, we analyzed the spectral and EL characteristics of the two sets of LEDs, those with the reference QW closer to the p-side and those with the reference QW closer to the n-side. The results are shown in figures 6.4 and 6.5. It is worth noticing that for the structure with the reference (495 nm) QW close to the p-side, emission from the 405 nm QW is not detected at RT, due to the higher hole capture efficiency of the 495 nm QW. In fact, as can be noticed by the band diagram simulated by Lorenzo Avataneo and Michele Goano of PoliTO reported in figure 6.6, almost all holes are captured by the 495 nm QW in the structure C. Both QWs showed a decrease in luminescence intensity during stress time; remarkably, the EL drop was found to be much stronger when the reference QW is closer to the p-side. Despite this, the analysis of the OP drop kinetics indicates that it does not follow a square-root dependence on time, suggesting that the diffusion process responsible for the changes in the electrical characteristics is not the dominant cause for the degradation of the optical performance.

To investigate the physical origin of optical degradation, we analyzed the correlation between the spectral data and the degradation rate for the 405 nm and 495 nm. The results indicated a correlation between the initial luminescence of a given well, and its degradation rate: this is summarized by figure 6.7a, that reports the OP drop (measured at 100 µA, after 1000 min of stress) as a function of the initial QW luminescence. As can be noticed, QWs with higher initial luminescence show the strongest degradation rate. It is worth noticing that on the horizontal axis of figure 6.7a we put the square root of electro-luminescence, that is proportional to carrier density because the radiative recombination rate is proportional to the square of the carrier density. Thus, the log-log diagram demonstrates that degradation rate has a power-law dependence on carrier density (n $\approx$ 1.6).

The physical origin of the optical properties degradation could be related to two dominant non-radiative processes: SRH recombination, which depends linearly on the carrier density,

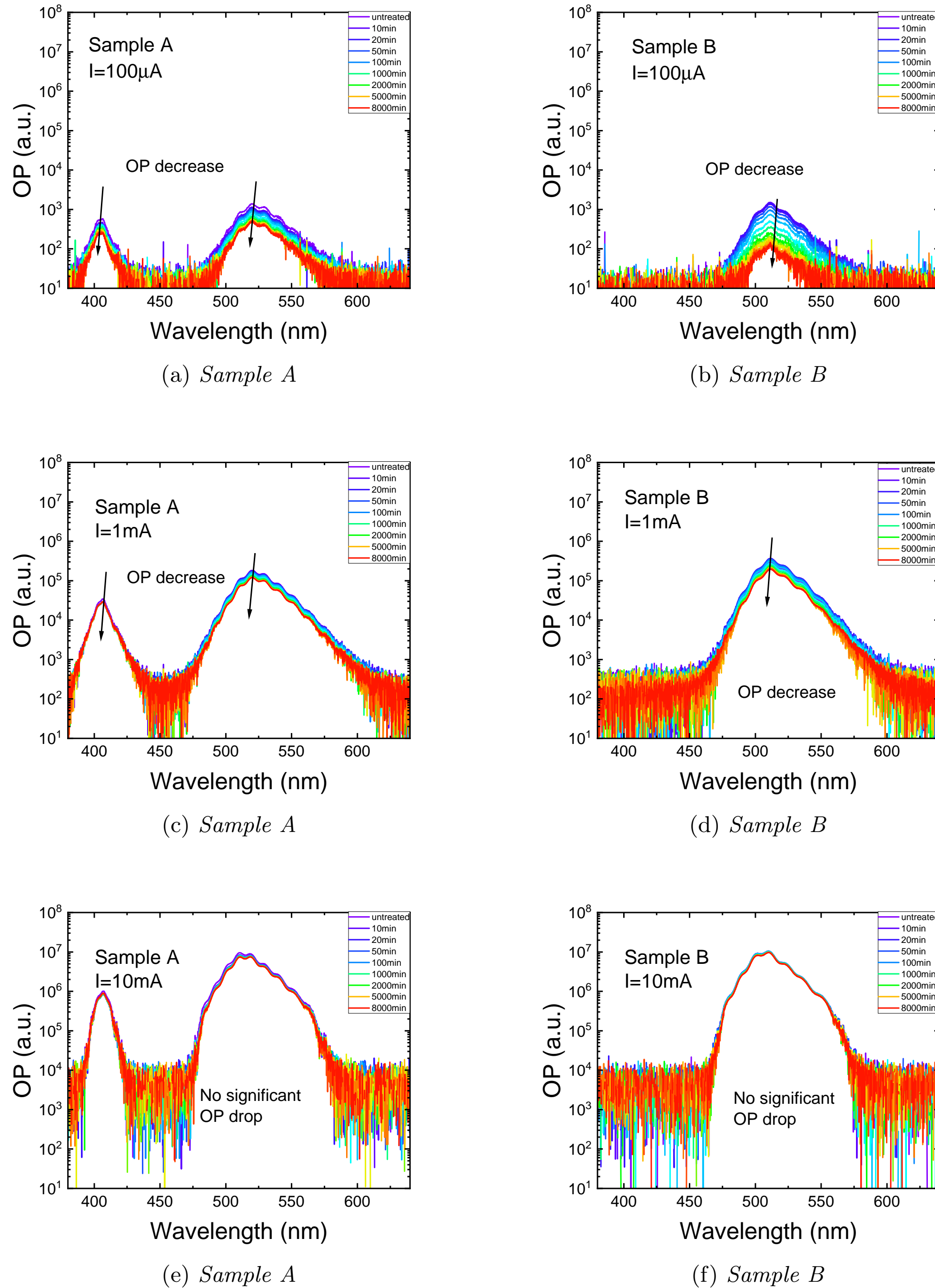

(a) *Sample A* (b) *Sample B*

(c) *Sample A* (d) *Sample B*

(e) *Sample A* (f) *Sample B*

Figure 6.4: Spectra of electro-luminescence measured at different driving current during the constant step-stress at 200mA. All the spectra are taken at room temperature.

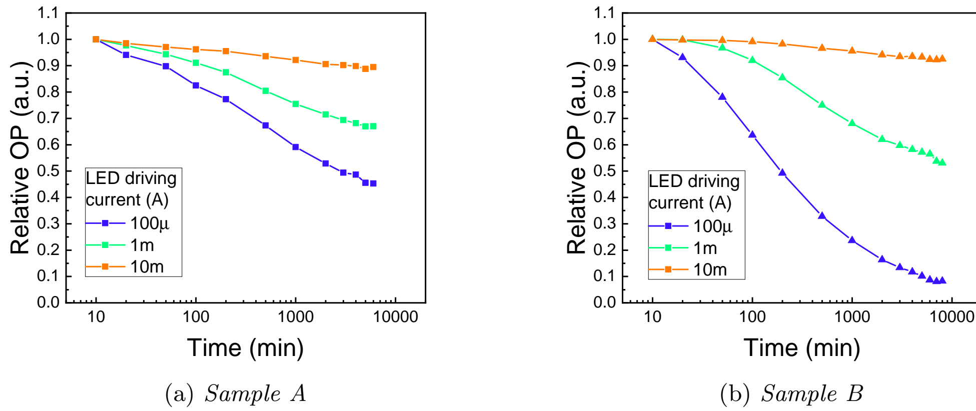

(a) *Sample A* (b) *Sample B*

Figure 6.5: Degradation kinetics of electro-luminescence of samples A and B: the measured optical power is related to the reference QW only (495 nm).

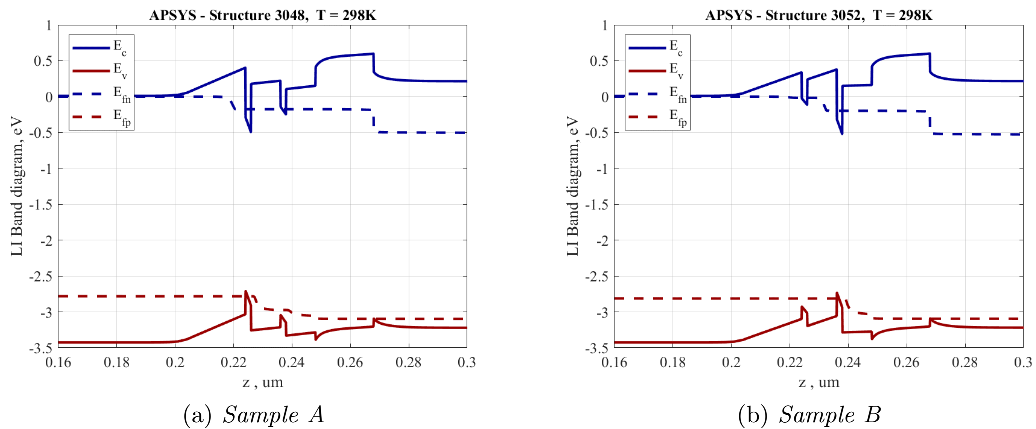

(a) *Sample A* (b) *Sample B*

Figure 6.6: Numerical simulations of the energy bands at 4V of the structures A and B. Courtesy of Lorenzo Avataneo and Michele Goano of the Department of Electronics and Telecommunications of PoliTO.

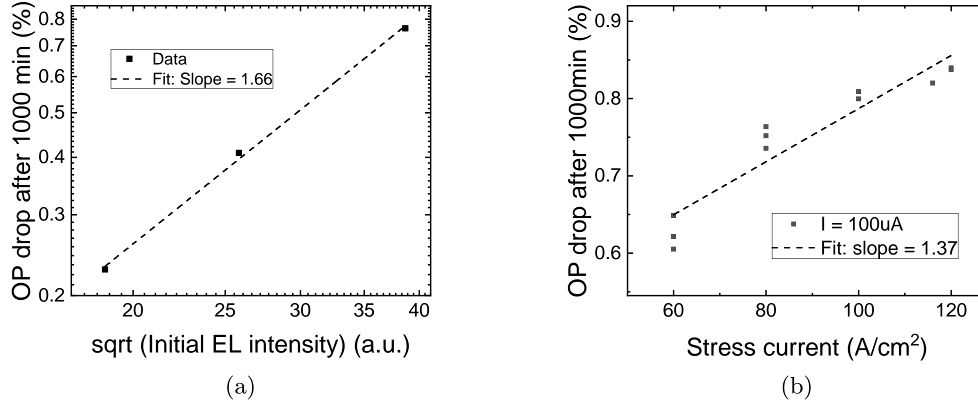

(a)

(b)

Figure 6.7: (a) Power-law dependence between the initial luminescence of a given well and tis degradation rate. (b) Statistical distribution of the OP drop after 1000 min of constant current stress at different current densities. The characterization current is 100μA.

and Auger recombination, which scales with n^3. Both the processes release the recombination energy as heat in the QWs region, which may be sufficient to break defect-impurity bonds in GaN [81, 88] and promote the defects propagation. Due to the power-law dependence of 1.3, the observed phenomenon is not compatible with Auger nor with standard SHR recombination. However, recent papers demonstrate the existence of superlinear defect-related recombination process, whose exponent may be higher than 1 (in [89], n $\approx$ 1.38). That superlinear behavior may be due to the presence of Urbach-like tails [89] on the conduction and valence bands. In this scenario, the SRH mechanism gains strength with injection because more defect levels become available as the quasi-Fermi energies move toward the band edges. Alternatively, the superlinearity may arise from density-driven delocalization, which permits carriers to be captured by non-radiative centers further from localization sites [89]. Based on this, we suggest that the defect generation process is initiated by SRH recombination and the process is accelerated by carrier density. In fact, by stressing devices at various current levels, we further confirmed the role of carrier density in the degradation process: degradation rate (OP drop after 1000 min of stress) was found to have a linear dependence on stress current level (see figure 6.7b, slope = 1.37), in agreement with previous reports on the topic.

The electrical and optical characteristics at the stress current value were measured during the constant stress by means of a sourcemeter and a photodiode. in figure 6.8 is reported the signal detected by the photodiode: sample A emits more light that the B variant, revealing the lower efficiency of the sample B. The latter is also the only sample that shows a OP drop at the stress current level. About the electrical characteristics, the device voltage drop measured at the stress current is reported in figure 6.9: the lower energy efficiency of sample B is confirmed, being the electrical power higher than the sample A one. The gradual decrease of the voltage drop may be ascribed to the gradual annealing of Mg due to the high power dissipation within the device, which may improve the electric contact. Differences in the

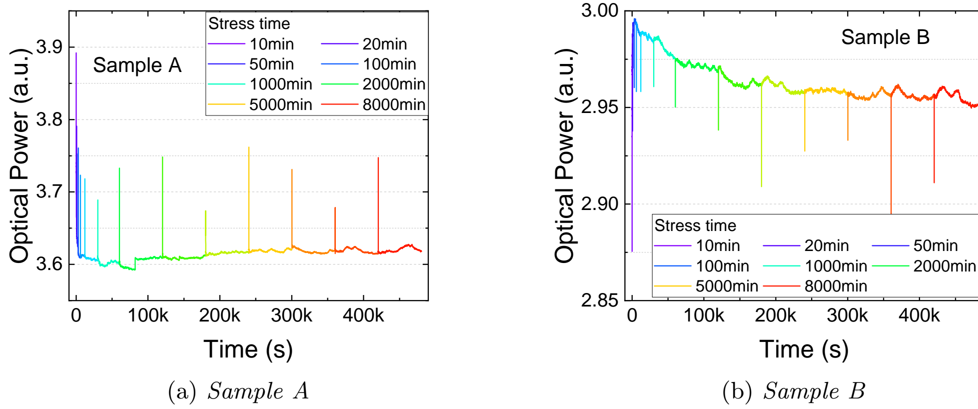

(a) *Sample A* (b) *Sample B*

Figure 6.8: Degradation kinetics of electro-luminescence of samples A and B evaluated at the stress current (200mA). The signal is the panchromatic integral of the electro-luminescence of the analyzed devices.

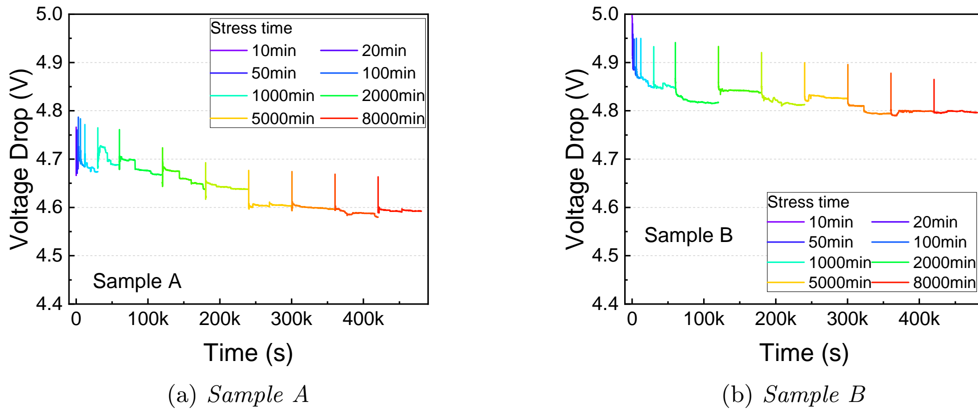

(a) *Sample A* (b) *Sample B*

Figure 6.9: Voltage drop on analyzed devices during the constant current stress. The higher voltage of the sample B may be related to a worst contact on the p-side.

electric contact are in agreement with what can be noticed in the IV characterization in figure 6.2: sample A shows a lower series resistance in the high forward bias region, if compared with the other variant.

To be more specific on the properties of the defects involved in the degradation process, we carried out DLOS measurements with increasing stress times. The results are reported in figure 6.10: one needs to consider the spectral range below 2.5-2.7 eV, since above this energy generation in the QWs becomes relevant, thus covering defect-generated signal. As can be noticed, stress induced an increase in the density of deep levels within the active region of the devices; such increase is particularly noticeable for energies lower than 2.3 eV (corresponding to defects located between midgap and E_C-2.3 eV). Albeit the measurement sensitivity was not enough for clearly estimating the energy position of such levels, the results support the

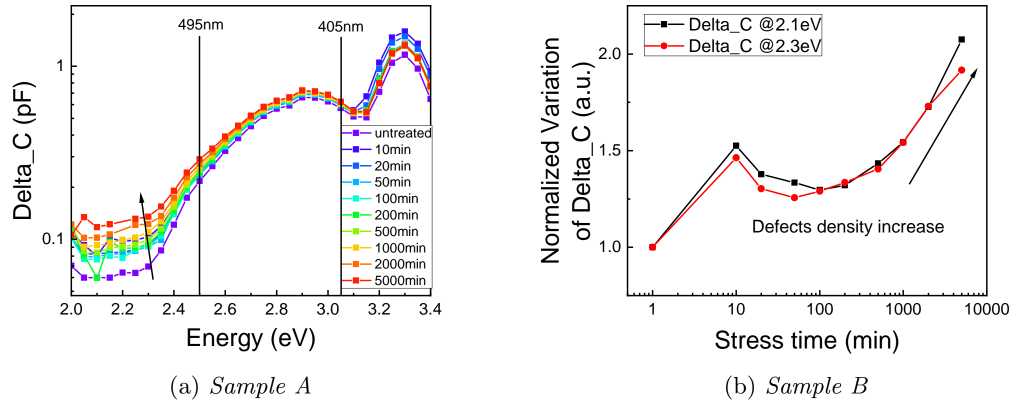

(a) *Sample A* (b) *Sample B*

Figure 6.10: Deep Level Optical Spectroscopy measurements on sample A during constant current stress at 200mA: the increase of DLOS signal confirms defect density increase.

hypothesis that stress induced an increase in the density of deep traps. Such defects are supposed to be located near midgap, since they act as efficient SRH centers, and they impact on the sub-threshold forward leakage (as predicted theoretically in [90, 91]).

6.3 Structures A and C: different Al concentration in EBL

The second comparison is related to the samples A and C, which differ in the aluminum doping in the electron blocking layer, resulting in a different height of the energy barrier of that region. Figure 6.11 reports the current-voltage characteristics of the stressed devices collected before and during stress at 200 mA. Similarly to what was observed for the first comparison, stress induced a significant increase in both reverse current and sub turn-on forward leakage (in the voltage range between 1 and 2.5 V). In both voltage ranges, conduction is mainly dominated by defect-assisted mechanisms. The behavior of the two structures is more similar than the two compared in figure 6.2, being here the EBL the only difference into the epitaxial stack. Namely, this stronger similarity can be noticed in the comparison draw in figure 6.12.

Also in this case, the reverse-bias regime is typically dominated by hopping transport mechanism (either variable-range hopping, VRH, or nearest-neighbor hopping, NNH) [70, 37, 71, 72] and partly helped by the contribution of thermally-assisted multistep tunneling [37]. As a consequence, reverse conduction is strongly dependent on the density of defects within the depleted region or, equivalently, on the distance between neighboring traps. In the low forward bias regime (still between 1 and 2.5 V), conduction is mostly dominated by trap-assisted tunneling [73]: the defect-mediated current is proportional to the density of defects [74].

As shown in figure 6.12, during stress the reverse leakage of the devices showed a monotonic increase, indicating a gradual increase in the density of defects within the active region. Remarkably, reverse leakage increased with the square-root of stress time. Here the hypothesis

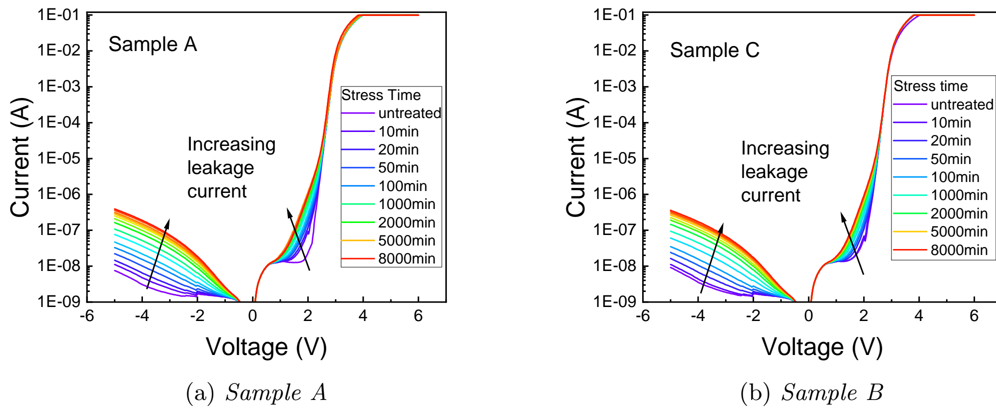

(a) *Sample A*　(b) *Sample B*

Figure 6.11: IV characteristics measured during the constant current stress at 200mA.

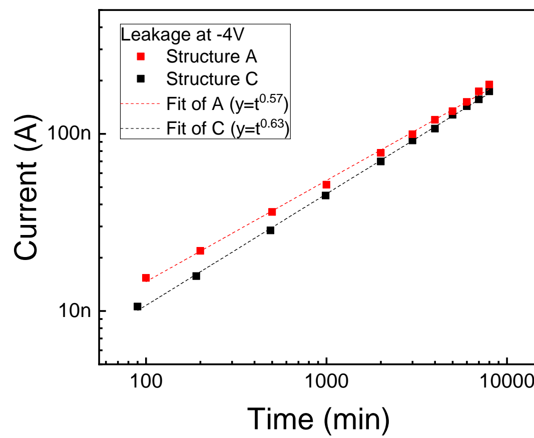

Figure 6.12: Change in the reverse leakage over time at -4V.

is that the leakage increase is due to the increase in the defect density in the depleted region due to a diffusion process [75, 76, 77]. The interpretation of those experimental data follows the aforementioned hypothesis: a defect concentration gradient from one of the doped layers to the intrinsic quantum well region is present. Due to the high stress current densities, the energy released by non-radiative recombination may promote the propagation of defects, from the region with high concentration towards the quantum wells. Once they reach the quantum wells, the diffusing defects may further increase the impact of SRH recombination, by acting as non-radiative recombination centers, thus lowering the quantum efficiency of the devices. The non-radiative nature of the degradation process was confirmed by the optical measurements 6.13: optical power degradation was found to be present only in the low current regime (below 1 mA), i.e. in the current range where recombination efficiency is limited by SRH losses [87].

The graphs in figure 6.13 show the spectra of the devices during the constant current stress, measured at bias levels below the nominal current of the device. As can be noticed, the optical emission of both the quantum wells is present in both the samples, being the QW order the same. The emission of the reference QW (495 nm) is still higher than the 405nm one, due to higher capture efficiency of the first QW. In low injection conditions (for current levels below 1mA) the behavior of the samples is very similar. Increasing the current level of the optical characterization, few differences can be identified: as reported in figure 6.14b, the 405 nm QW (close to p-side) improves its optical performance when the current level is higher than 1mA. Moreover, a 20% improvement can be noticed in the sample C at the end of the experiment. Focusing on the 495 nm QW (close to n-side) the stronger degradation can be noticed in the sample A, the one with the higher EBL, but only at low injection densities.

The optical power comparison in th figure 6.15 reveals the higher efficiency of the sample C, if compared with the other one. Both the samples does not show any optical degradation at the stress current level, but sample A shows that OP decreases with stress time (figure 6.16). Namely, sample C has also a higher power efficiency, being the voltage at 200mA lower than the A variant.

The experimental data can be interpreted as follows:

- as mentioned for the comparison between samples A and B, the increase of the leakage current in reverse and low forward bias regions could be ascribed to the propagation of defects towards the QWs region.
- the generation of non-radiative recombination centers is related to the OP drop detected at low injection levels, where the impact of SRH recombination is stronger.
- the absence of significant OP degradation at high injection levels is in agreement with the defect-propagation hypothesis, being the reference QW far from the p-side.
- the OP improvement of the 405 nm QW may be correlated to a better injection of holes due to the high power dissipation: i) the high temperature reached in the QW region

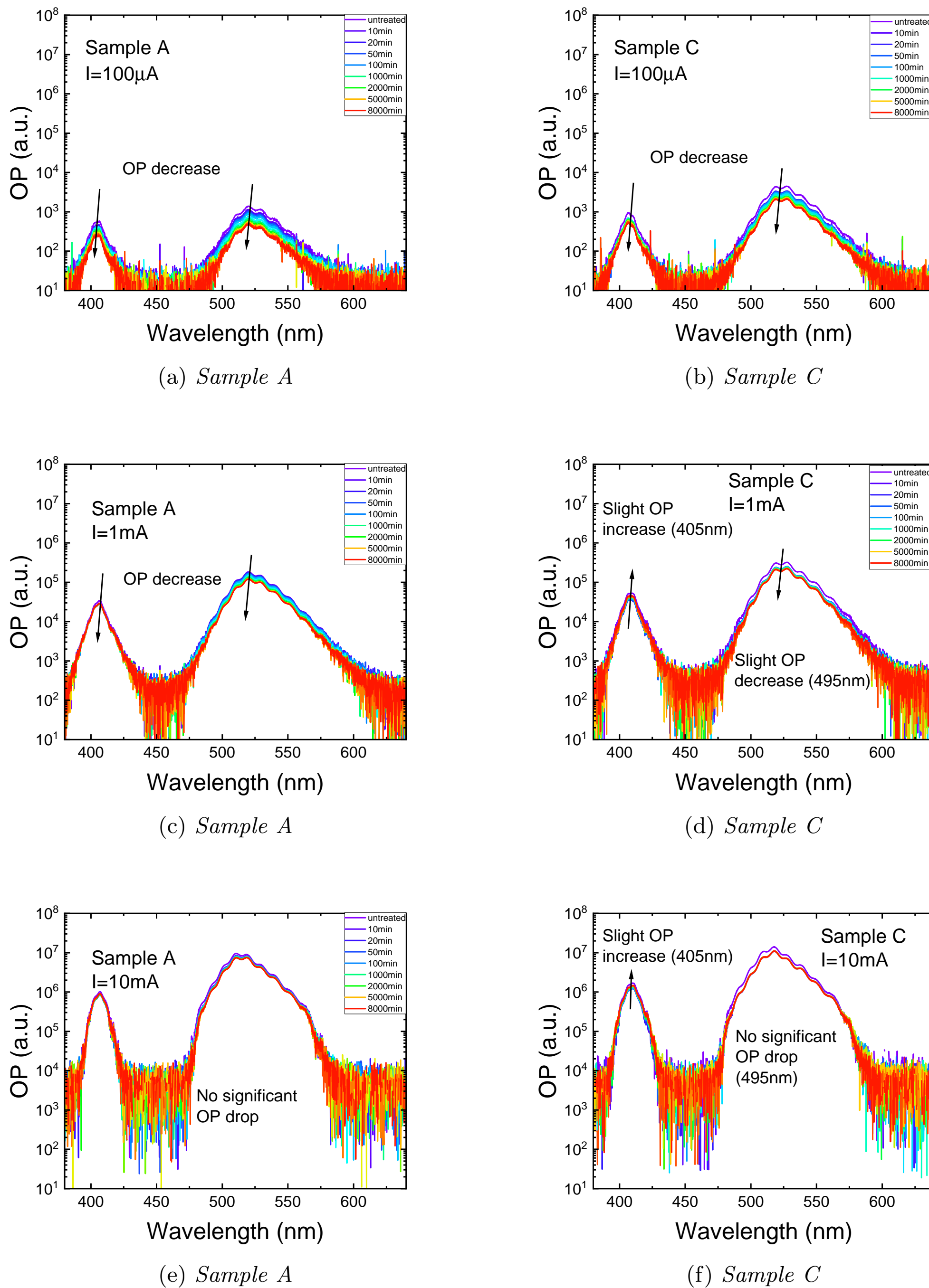

(a) *Sample A* (b) *Sample C*

(c) *Sample A* (d) *Sample C*

(e) *Sample A* (f) *Sample C*

Figure 6.13: Spectra of electro-luminescence measured at different driving current during the constant step-stress at 200mA. All the spectra are taken at room temperature.

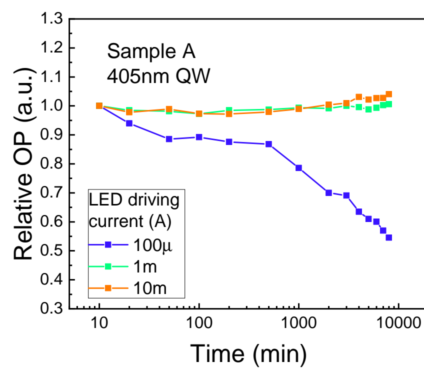

(a) *Sample A, 405nm QW*

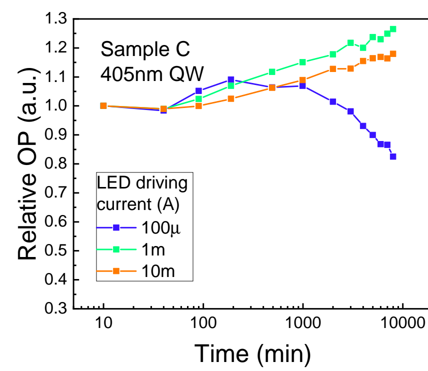

(b) *Sample C, 405nm QW*

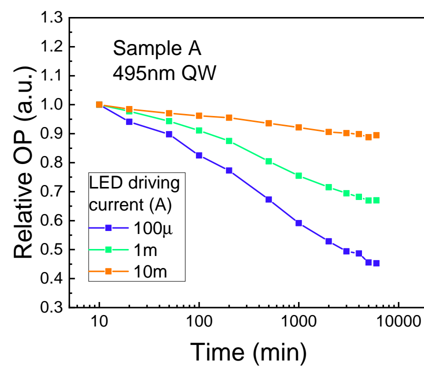

(c) *Sample A, 495nm QW*

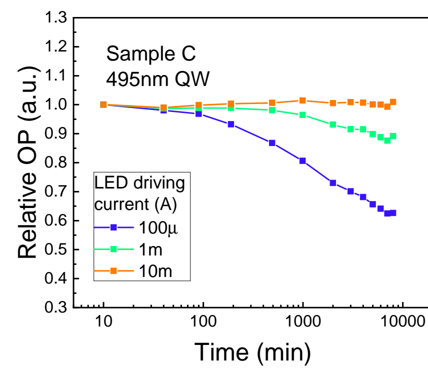

(d) *Sample C, 495nm QW*

Figure 6.14: Degradation kinetics of electro-luminescence of samples A and C.

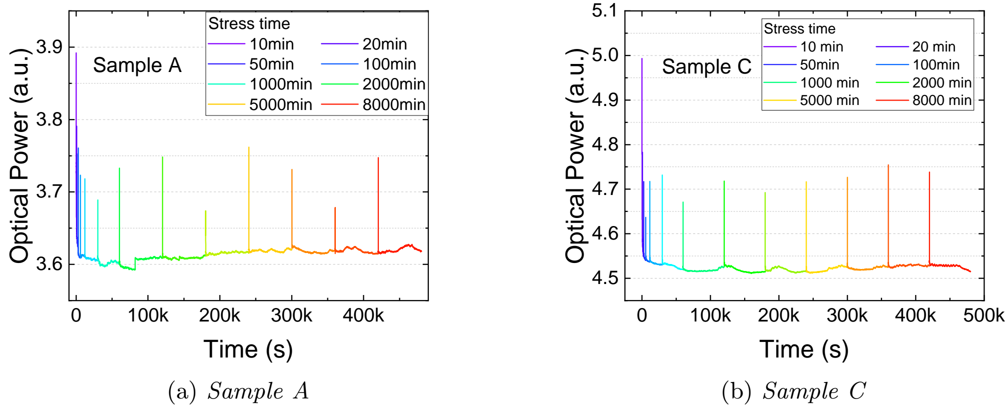

(a) *Sample A* (b) *Sample C*

Figure 6.15: Degradation kinetics of electro-luminescence of samples A and C evaluated at the stress current (200mA). The signal is the panchromatic integral of the electro-luminescence of the analyzed devices.

may trigger the annealing of Mg and other dopants or ii) holes could be able to reach the QW region through the defects that are moving towards the QWs.

- the higher quantum efficiency of the sample C can be related to the lower height of the EBL: according to the literature, a higher EBL should improve the quantum efficiency, due to a better electron confinement; by contrary, not having any grading in the EBL Al doping, these samples may suffer of a poor hole injection due to a spike into the energy barrier, which could limit the injection into the active region. Therefore, a lower Al content (sample C) reduces the resistance to the hole injection, improving the internal quantum efficiency. This hypothesis can be confirmed by the simulated band diagram performed by Lorenzo Avataneo and Michele Goano of the Department of Electronics and Telecommunications of PoliTO, reported in figure 6.17.
- the lower voltage drop detected on the sample C is in agreement to the hole injection hypothesis mentioned above.

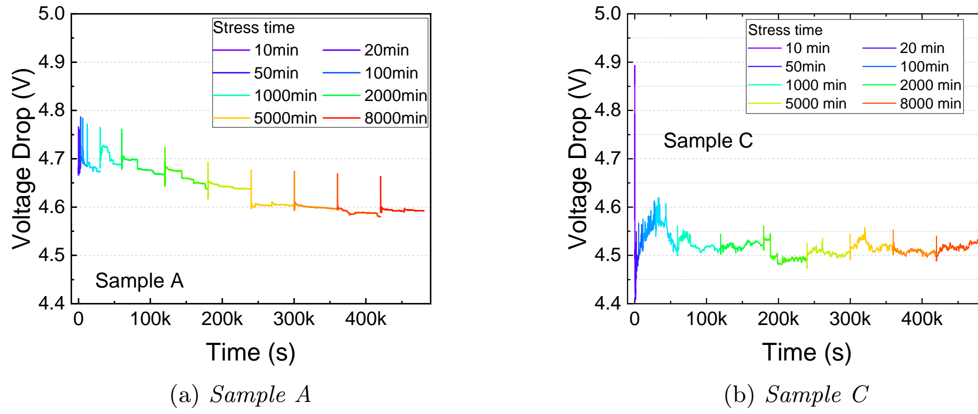

(a) *Sample A* (b) *Sample C*

Figure 6.16: Voltage drop on analyzed devices during the constant current stress.

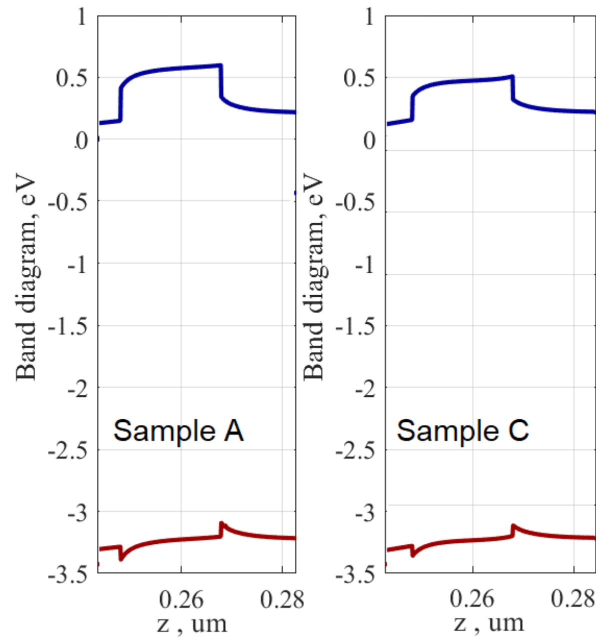

Figure 6.17: Numerical simulation of the band diagram of samples A and C, focus on the EBL: can be noticed as the different Al content is related to a sharper edge of the EBL on the valence band, inducing a higher barrier for the holes injection. Courtesy of Lorenzo Avataneo and Michele Goano of the Department of Electronics and Telecommunications of PoliTO.

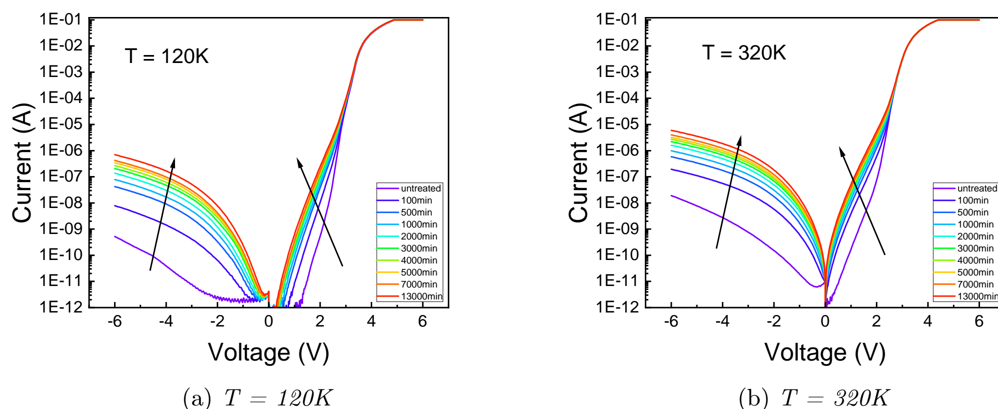

(a) $T = 120K$ (b) $T = 320K$

Figure 6.18: Electrical characterization of sample B at different temperatures.

6.4 DLTS on Wafer B

Deep Level Transient Spectroscopy (DLTS) analysis was carried out on a sample of Wafer B, with the aim to identify the physical origin of the lattice defects. To this aim, a sample was submitted to a constant current stress at 150mA (room temperature) and characterized during the stress test. Being the sample into the DLTS cryostat, also IV and LI in temperature were performed, by means of a semiconductor parameter analyzer and a compact array spectrometer (CAS) with low noise cooled-detector. in figure 6.18 are reported the current-voltage characterization in temperature (IVT) of the tested sample during the stress experiment. The comparison of the two analyzed temperatures (120K and 320K) shows the strong differences in leakage current in reverse and low forward bias in the two conditions, for all the duration of the constant stress. Being the conduction in this bias conditions normally related to variable hopping mechanisms, here the strong role of a thermally assisted conduction mechanism can be noticed [37, 92]. The leakage current increase in the reverse bias conditions (in the -4/-6V range) is about three orders of magnitude during the stress experiment, in both the showed temperatures. This suggests as, the defects which contribute to the leakage conduction are active in the whole temperature range.

The temperature influence can be noticed also in the spectrally resolved optical characterization displayed in figure 6.19: the spectral shape significantly changes between the two temperatures. In fact, at cryogenic temperatures, luminescence from the 405 nm QW and a peak at 366 nm can be detected. The latter suggests band-to-band recombination in GaN: being visible only at the highest current level, band-to-band recombination could take place in the p-side region, thanks to electrons which are able to overcome the EBL, or in the GaN spacer between the EBL and the QWs.

The data in figure 6.19 can be interpreted as follows:

- The role of the non-radiative recombination is clear in the narrowing of the electroluminescence spectra by increasing the temperature (6.19a and -b), which limits the

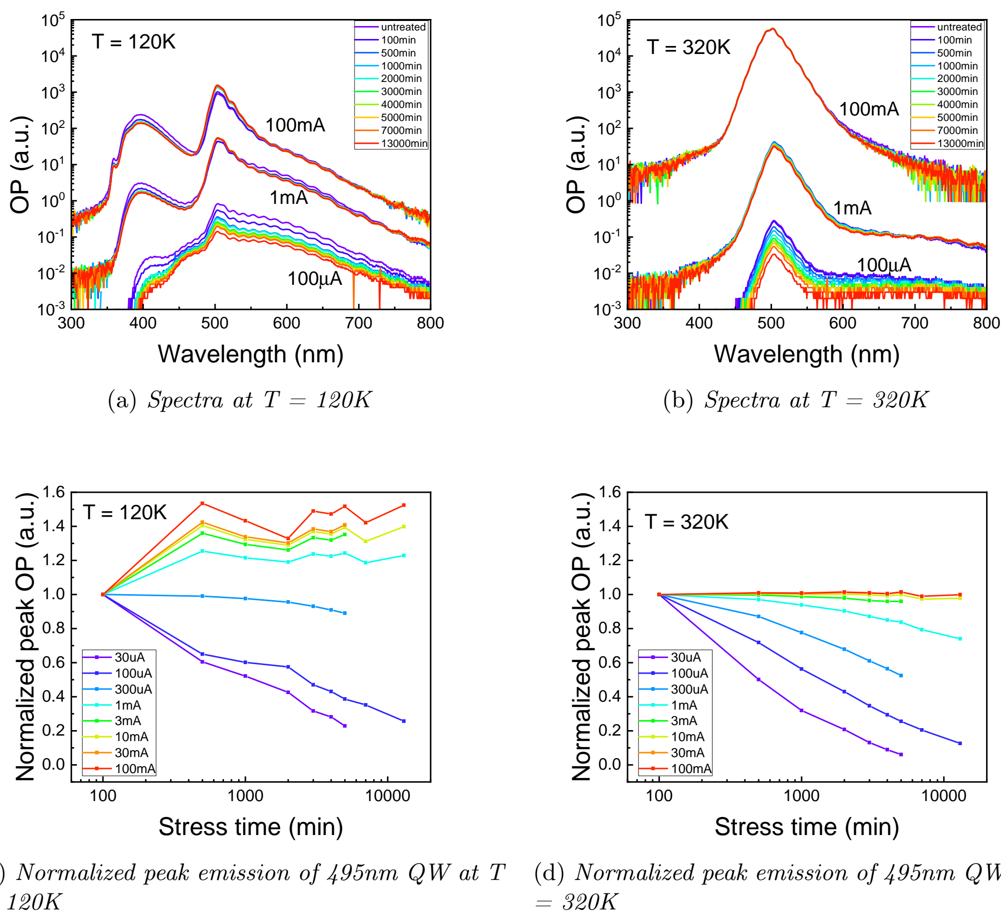

(a) *Spectra at T = 120K*

(b) *Spectra at T = 320K*

(c) *Normalized peak emission of 495nm QW at T = 120K*

(d) *Normalized peak emission of 495nm QW at T = 320K*

Figure 6.19: Spectrally resolved optical characterization of sample B at different temperatures and normalized peak emission at 495 nm over time.

yellow-band emission at 320K. SHR recombination can also be related to the OP drop detected at low injection levels.

- The emission from the 405nm QW, detected at cryogenic conditions, could be related to the limited impact of SHR and to limited lattice scattering at such low temperature, which improve the holes injection into that QW.

- The drop in the OP of the 405 nm QW is probably related to the holes density decrease. This behavior could be ascribed to the improvement of the capture rate of the reference QW, as suggested by the OP increase detected in 6.19c for high injection levels.

- The OP drop at 320K for low injection levels is in agreement with the aforementioned experimental data of the constant current stress performed at room temperature.

Focusing on the DLTS characterization results, reported in figure 6.20, two different epitaxial regions were analyzed: the first one (a) is defined by the measure voltage -2V and filling

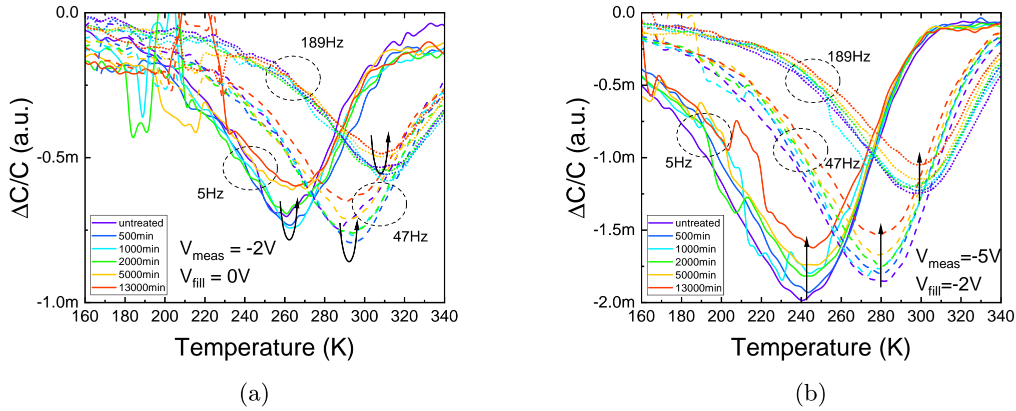

Figure 6.20: DLTS characterization of sample B during the constant current stress.

voltage 0V, the second one (b) is defined by the measure voltage -5V and filling voltage -2V. Due to the selected voltage ranges, the (a) region is closer to the QWs than the region (b). Being the signal amplitude $\Delta C/C$ proportional to the defect density, two different behaviors can be noticed: in the region (a) there is a first increase and then a decrease of the defect density during the constant current stress but the defect density is always lower (3 times roughly) than the (b) one during the experiment; this behavior is compatible with migration of defects within the analyzed region; the region (b) shows a decrease of the defect density with the stress time increase.

The further analysis of the DLTS data, by means of the Arrhenius activation energy analysis, suggest that the physical origin of those defects could be related to impurities on the AlGaN/GaN interface [93, 94] or to nitrogen vacancies into the lattice [95]. Moreover, further tests varying the filling time conditions suggest that the identified defects are probably point defects distributed along threading dislocations.

6.5 Closing remarks

In this chapter, the investigation on three different color coded test structures were presented. The structures have two quantum wells, emitting at different wavelengths: the 495nm QW is referred to as reference quantum well, whereas the QW emitting at 405 nm is referred to as secondary quantum well and is used as a “placeholder” to ensure that the all the structures are fabricated in similar growth conditions.

In the structure A, the reference QW is located closer to the p-side, whereas in the structure B it is located closer to the n-side. Structure C is a variation of the A one, in which the Al density (15%) into the electron blocking layer (EBL) is lower compared to the A version (20%), resulting in to a lower energy barrier defined by the EBL. The devices were submitted to constant current stress at 200 mA (80 A/cm^2) at room temperature and, during the stress, electrical and optical characteristics were monitored.

The analysis of the first two structures, which differ in the order of the QWs, reveals that the increase of leakage current in reverse and low forward bias regions is triggered by a diffusion process, due to their kinetics that scale with the square-root of time. In fact, in this bias range the typical dominant conduction mechanisms are variable-range hopping and nearest-neighbor hopping. Thus, the increase of the defect density strongly enhance the impact of such trap-assisted transport mechanisms.

Focusing on the optical characterization, the decrease of OP power over time is stronger on the structure where the reference QW is close to the p-side and has a higher impact at low injection levels: this suggests the possible propagation of defects from the p-side, which may act as non-radiative recombination centers and worse the optical performance of the device. Despite this, the evolution of the OP drop does not follow the square-root of time, indicating that the diffusion is not the dominant cause for the optical degradation. Then, the energy released (as heat) by non-radiative recombination in the QWs region may be the physical cause of the degradation, by triggering the propagation of defects and further enhancing the non-radiative recombination. According to recent papers ([89]), the non-radiative process responsible for the defects propagation could be SHR (rather than Auger) due to the power-law dependence on carried density of the degradation rate.

DLOS characterization confirms the increase of defect concentration, consisting in deep levels in the region between midgap and E_C-2.3 eV: due to their position, they act as efficient SRH centers and impact on the sub-threshold forward leakage.

The comparison between the structures with different EBL confirms the aforementioned hypothesis about the defects propagation and suggest the presence of spikes in the energy barrier of the EBL. Those spikes are related to the lack of grading in the Al doping concentration and generate a barrier on the valence band, limiting the injection of holes from the p-side. This reduces the quantum efficiency of the structure with the highest Al content (higher EBL) and increases the power dissipation on that structure. These hypothesis are in agreement with the simulation carried out the PoliTO on the same test structures.

DLTS characterizations on the sample with the reference QW on the n-side suggest the role impurities on the AlGaN/GaN interface or nitrogen vacancies into the lattice as physical origin of the defects that limit the device performance.

Chapter 7

Conclusions

This thesis investigated the reliability of state-of-the-art InGaN LEDs for lighting applications and the impact of the diffusion-related mechanisms on optoelectronic GaN-based wafers by means of specific tests and procedures, with the aim to identify the physical mechanisms responsible for the degradation of those devices. By means of custom experimental setups, developed during the research activity, it was possible to identify the dominant failure modes and degradation mechanisms of GaN LEDs subjected to electrical over-stress, both in forward and reverse bias, and to correlate specific failures with the epitaxy related weaknesses of state-of-the-art LEDs. In particular, to understand the role of defects in the device degradation, advanced techniques such as Deep-Level Transient Spectroscopy (DLTS) and Deep-Level Optical Spectroscopy (DLOS) were employed. Moreover, by means of thermal storage at high temperature and low energy electron beam irradiation (LEEBI) tests it was possible to investigate the role of the different epitaxial layers in the diffusion-related mechanisms. The information about the physical mechanisms responsible for degradation have been used as a feedback for devices manufacturers, for the improvement of the technological processes.

The most important achievements of the research activity are summarized in the next paragraphs.

Impact of growth parameters on the ESD robustness

An extensive analysis aimed to correlate the epitaxial growth parameters and LEDs ESD robustness in reverse bias was presented. The analysis investigated separately the roles of the epitaxial features on the n- and p-side by means of DC and pulsed characterizations and Deep Level Transient Spectroscopy technique. Due to the confidentiality of the presented data, the nature of the growth parameters and their actual values were not specified.

The results about the investigation on the n-side suggested the strong importance of the parameter A in the robustness to ESD events and the fact that defects involved in the reverse conduction are not critical for the robustness to this kind of extrinsic events. Optical DLTS characterizations revealed that the physical origin of those defects can be ascribed to nitrogen vacancies in the lattice.

The investigation on the p-side, instead, suggested the strong importance of the parameter C: spatially resolved electro-luminescence measurements revealed that leakage paths in the epitaxial structure could limit the robustness to ESD events. In fact, the most uniform and the least bright sample was the one with the highest C parameter: the leakage paths that acted as radiative recombination sites in reverse bias conditions could be responsible for the failure of the device, via shorting of the junction. These leakage paths might act also as non-radiative recombination sites. C-DLTS characterizations on those samples confirmed the impact of C parameter in the reduction of defect density in the epitaxial structure and suggested that nitrogen atoms may play a role as physical cause of those defects.

Failure limits of GaN-based LEDs under EOS

The analysis was carried out by a custom-setup, that allowed us to measure the current-voltage (I-V) and electro-luminescence curves of the devices while pulsing them with increasing voltages in forward bias, up to failure. The aim of this work was to analyze and characterize the degradation mechanisms induced by the extremely high current densities reached during the EOS events. In this work were investigated (i) the dependence of failure current/power on pulse duration, (ii) the dependence of the electrical characteristics on temperature and (iii) the optical characteristics of the devices under over-stress conditions.

The statistical description of the failure events suggested that they were enhanced by the temperature of the sample: due to the strong self-heating, the power dissipation required to reach the failure condition is less if the biasing time is longer, leading to open-like failures (package-related) for the longest pulse width. Further experiments at high current densities identified a thermally-assisted conduction mechanism and the enhancing of the non-radiative recombination promoted by the high junction temperature.

The comparison of electrical and optical characteristics during the EOS stress tests allowed us to identify four different regions: (i) region A, in which radiative recombination was dominating and non-uniform band-filling could be detected; (ii) region B, in which strong self-heating could be noticed; (iii) region C, where the saturation of the QWs induced a strong overflow and might lead to additional power dissipation; (iv) region D, in which the very high current density induced the current crowding effect, leading to a progressive decay of the optical properties of the device due to to the formation of leakage paths under the anode pad. The detection of optical emission around the 400 nm could be ascribed to electrons overflowing the electron blocking layer, reaching the p-side of the junction. The results of this work were published on the scientific journal *Microelectronics Reliability* ([26]).

Evidence for avalanche generation in reverse-biased InGaN LEDs

Avalanche generation is a physical mechanism responsible for the breakdown at extremely high field, such as in the reverse bias conditions typical of ESD discharges. In this part was presented the experimental evidence that avalanche generation can take place in state-of-

the-art InGaN-based blue LEDs.

The significant increase of leakage current at reverse bias voltages below -80V suggested that the extremely high electric field triggered band to band tunneling, becoming the dominant conduction mechanisms at such reverse voltages. Moreover, the rightward shift in the IV curves below -80V with increasing temperature suggested that also avalanche generation played a role: being the impact ionization strongly dependent on the mean free path, a higher temperature of the device is able to limit it, inducing the right-shift in the IV. TCAD simulations on a simplified epitaxial structure suggested that the estimated thickness for a band-to-band tunneling is 6 nm when the device is biased in such strong reverse bias conditions.

Further analysis of the electro-luminescence spectral distribution, in this extreme bias conditions, showed that (i) hole and electron pairs generated by the avalanche process recombine radiatively, generating photons, (ii) which are partially re-absorbed in the In-containing layers and n-GaN side and then (iii) re-emitted as internal photoluminescence of the yellow-emitting defects in the n-GaN layer.

The relevant outcomes of this work were presented to the conference *Photonics West 2019* and included in the conference proceedings [27].

Gradual degradation of color coded test structures

In this chapter, the investigation on three different color coded test structures were presented. The structures had two quantum wells, emitting at different wavelengths.

In the structure A, the reference QW was located closer to the p-side, whereas in the structure B it was located closer to the n-side. Structure C was a variation of the A one, in which the Al density (15%) into the electron blocking layer (EBL) was lower compared to the A version (20%), resulting in to a lower energy barrier defined by the EBL. The devices were submitted to constant current stress at 200 mA (80 A/cm^2) at room temperature and, during the stress, electrical and optical characteristics were monitored.

The analysis of the first two structures, which differ in the order of the QWs, revealed that the increase of leakage current in reverse and low forward bias regions was triggered by a diffusion process, due to their kinetics that scaled with the square-root of time. Focusing on the optical characterization, the decrease of OP power over time was stronger on the structure where the reference QW was close to the p-side and had a higher impact at low injection levels: this suggested the possible propagation of defects from the p-side, which might act as non-radiative recombination centers and worsen the optical performance of the device. The optical degradation was not dominated by the diffusion process, but the energy released (as heat) by non-radiative recombination in the QWs region might be its physical cause. According to recent papers ([89]), the non-radiative process responsible for the defects propagation could be SHR recombination.

The comparison between the structures with different EBL confirmed the aforementioned hypothesis about the defects propagation and suggested the presence of spikes in the energy

barrier of the EBL. Those spikes were related to the lack of grading in the Al doping concentration and generated a barrier on the valence band, limiting the injection of holes from the p-side. These hypothesis are in agreement with the simulation carried out the PoliTO on the same test structures.

DLOS and DLTS characterizations confirmed the increase of defect concentration, consisting in deep levels in the region between midgap and E_C-2.3 eV, and suggested the role impurities at the AlGaN/GaN interface or of nitrogen vacancies into the lattice as physical origin of these defects.

List of Abbreviations

DLOS	Deep Level Optical Spectroscopy
DLTS	Deep Level Transient Spectroscopy
EBL	Electron Blocking Layer
EOS	Electrical Over Stress
ESD	Electro-Static Discharge
LED	Light Emitting Diode
LEEBI	Low Energy Electron Beam Irradiation
QW	Quantum Well
SRH	Shockley–Read–Hall

Bibliography

[1] Shuji Nakamura, Takashi Mukai, and Masayuki Senoh. "High-Power GaN P-N Junction Blue-Light-Emitting Diodes". In: *Jpn. J. Appl. Phys* 30 (1991). URL: http://iopscience.iop.org/1347-4065/30/12A/L1998.

[2] T Egawa, T Jimbo, and M Umeno. "Characteristics of InGaN/AlGaN light-emitting diodes on sapphire substrates". In: *Journal of Applied Physics* 82.11 (1997), pp. 5816–5821. ISSN: 0021-8979. DOI: 10.1063/1.366450. URL: http://dx.doi.org/10.1063/1.366450http://aip.scitation.org/toc/jap/82/11http://aip.scitation.org/doi/10.1063/1.366450.

[3] Yukio Narukawa et al. "Improvement of Luminous Efficiency in White Light Emitting Diodes by Reducing a Forward-bias Voltage". In: *Japanese Journal of Applied Physics* 46.No. 40 (2007), pp. L963–L965. ISSN: 0021-4922. DOI: 10.1143/JJAP.46.L963. URL: http://stacks.iop.org/1347-4065/46/L963.

[4] Lilin Liu, Jianfu Yang, and Gang Wang. "The investigation of LED's reliability through highly accelerated stress testing methods". In: *14th International Conference on Electronic Materials and Packaging, EMAP 2012* (2012), pp. 2–4. DOI: 10.1109/EMAP.2012.6507888.

[5] K. R. Shailesh, S. Tanuja, and M. Vijendra Kamath. "Analysis of energy savings from replacing HPSV lighting with LED lighting in road lighting application". In: *Proceedings - ICETEEEM 2012, International Conference on Emerging Trends in Electrical Engineering and Energy Management* (2012), pp. 473–477. DOI: 10.1109/ICETEEEM.2012.6494510.

[6] B. H. Hamon et al. "A new lifetime estimation model for a quicker LED reliability prediction". In: *Thirteenth International Conference on Solid State Lighting* 9190 (2014), p. 919007. DOI: 10.1117/12.2060791.

[7] Yukio Narukawa et al. "Ultra-high efficiency white light emitting diodes". In: *Japanese Journal of Applied Physics, Part 2: Letters* 45.37-41 (2006), pp. 58–61. ISSN: 00214922. DOI: 10.1143/JJAP.45.L1084.

[8] Y. Wu, C.-Y. Chen, and J. A. del Alamo. "Electrical and structural degradation of GaN high electron mobility transistors under high-power and high-temperature Direct Current stress". In: *Journal of Applied Physics* 117.2 (2015), p. 025707. ISSN: 0021-8979. DOI: 10.1063/1.4905677. URL: http://aip.scitation.org/doi/10.1063/1.4905677.

[9] L.-R. Trevisanello et al. "Thermal stability analysis of high brightness LED during high temperature and electrical aging". In: 6669 (2007), p. 666913. DOI: 10.1117/12.732398. URL: http://proceedings.spiedigitallibrary.org/proceeding.aspx?doi=10.1117/12.732398.

[10] M. Meneghini et al. "A model for the thermal degradation of metal/ (p-GaN) interface in GaN-based light emitting diodes". In: *Journal of Applied Physics* 103.6 (2008). ISSN: 00218979. DOI: 10.1063/1.2885703.

[11] Matteo Meneghini et al. "A review on the physical mechanisms that limit the reliability of GaN-based LEDs". In: *IEEE Transactions on Electron Devices* 57.1 (2010), pp. 108–118. ISSN: 00189383. DOI: 10.1109/TED.2009.2033649. URL: http://ieeexplore.ieee.org/document/5332356/.

[12] C. De Santi et al. "Failure causes and mechanisms of retrofit LED lamps". In: *Microelectronics Reliability* 55.9-10 (2015), pp. 1765–1769. ISSN: 00262714. DOI: 10.1016/j.microrel.2015.06.080.

[13] K.T. Kaschani. "What is Electrical Overstress? - Analysis and Conclusions". In: *Microelectronics Reliability* 55.6 (2015), pp. 853–862. ISSN: 00262714. DOI: 10.1016/j.microrel.2015.03.003. URL: http://dx.doi.org/10.1016/j.microrel.2015.03.003https://linkinghub.elsevier.com/retrieve/pii/S0026271415000530.

[14] OSRAM Opto-Semiconductors GmbH. "The Basic Principles of Electrical Overstress (EOS)". In: July (2013), pp. 1–10.

[15] M. Meneghini et al. "Degradation mechanisms of high-power LEDs for lighting applications: An overview". In: *IEEE Transactions on Industry Applications* 50.1 (2014), pp. 78–85. ISSN: 00939994. DOI: 10.1109/TIA.2013.2268049.

[16] M. Meneghini et al. "Leakage current and reverse-bias luminescence in InGaN-based light-emitting diodes". In: *Applied Physics Letters* 95.17 (2009), pp. 11–14. ISSN: 00036951. DOI: 10.1063/1.3257368.

[17] E Zanoni et al. "Aging behavior, reliability, and failure physics of GaN-based optoelectronic components". In: *Proceedings of SPIE - The International Society for Optical Engineering* 9768.ii (2016), pp. 1–8. ISSN: 1996756X. DOI: 10.1117/12.2225128. URL: http://www.scopus.com/inward/record.url?eid=2-s2.0-84978704686{\&}partnerID=MN8TOARS.

[18] Haicheng Cao et al. “Degradation behaviors and reliability of high power GaN-based white LEDs with different structures”. In: *2016 13th China International Forum on Solid State Lighting (SSLChina)*. IEEE, 2016, pp. 74–79. ISBN: 978-1-5090-5611-8. DOI: 10.1109/SSLCHINA.2016.7804355. URL: http://ieeexplore.ieee.org/document/7804355/.

[19] Matteo Meneghini et al. “Chip and package-related degradation of high power white LEDs”. In: *Microelectronics Reliability* 52.5 (2012), pp. 804–812. ISSN: 00262714. DOI: 10.1016/j.microrel.2011.07.091. URL: http://dx.doi.org/10.1016/j.microrel.2011.07.091.

[20] Steven H. Voldman. *Electrical overstress (EOS) : devices, circuits, and systems*. 1st ed. Chichester, UK: Wiley, 2014, p. 368. ISBN: 9781118511886. URL: http://books.google.com/books?id=eu3pQAHTl6sC{\&}pgis=1.

[21] R. Tuttle. “Electrical Overstress Simulation and Failure Mechanisms of Light Emitting Diodes”. In: *LED Professional 2014 symposium* (2014).

[22] Cree Inc. *Cree XLamp LED Electrical Overstress*. 2010.

[23] Tingting Nan et al. “An analysis on damage of light-emitting diodes reliability induced by electronic static discharge”. In: *2016 17th International Conference on Electronic Packaging Technology, ICEPT 2016* (2016), pp. 1122–1126. DOI: 10.1109/ICEPT.2016.7583322.

[24] Shih Wei Wang et al. “Investigation of the effect of nitride-based LEDs fabricated using hole injection layer at different growth temperatures”. In: *Japanese Journal of Applied Physics* 55.5 (2016). ISSN: 13474065. DOI: 10.7567/JJAP.55.05FJ14.

[25] M. Dal Lago et al. “ESD on GaN-based LEDs: An analysis based on dynamic electroluminescence measurements and current waveforms”. In: *Microelectronics Reliability* 54.9-10 (2014), pp. 2138–2141. ISSN: 00262714. DOI: 10.1016/j.microrel.2014.07.122. URL: http://dx.doi.org/10.1016/j.microrel.2014.07.122.

[26] N. Renso et al. “Failure limits and electro-optical characteristics of GaN-based LEDs under electrical overstress”. In: *Microelectronics Reliability* 88-90 (2018), pp. 887–890. ISSN: 00262714. DOI: 10.1016/j.microrel.2018.06.054. URL: https://linkinghub.elsevier.com/retrieve/pii/S0026271418304700.

[27] Nicola Renso et al. “Demonstration of band-to-band tunneling and avalanche regime in InGaN LEDs”. In: *ICNS-13 Proceedings*. 2019.

[28] E. Fred Schubert. *Light-Eitting Diodes*. Cambridge: Cambridge University Press, 2006, p. 422. ISBN: 978-0-511-34476-3. DOI: 10.1017/CBO9780511790546. URL: http://ebooks.cambridge.org/ref/id/CBO9780511790546.

[29] R. L. Longini and R. F. Greene. “Ionization Interaction between Impurities in Semiconductors and Insulators”. In: *Physical Review* 102.4 (1956), pp. 992–999. ISSN: 0031-899X. DOI: 10.1103/PhysRev.102.992. URL: https://link.aps.org/doi/10.1103/PhysRev.102.992.

[30] W. Shockley and W. T. Read. “Statistics of the Recombinations of Holes and Electrons”. In: *Physical Review* 87.5 (1952), pp. 835–842. ISSN: 0031-899X. DOI: 10.1103/PhysRev.87.835. URL: https://link.aps.org/doi/10.1103/PhysRev.87.835.

[31] R. N. Hall. “Electron-Hole Recombination in Germanium”. In: *Physical Review* 87.2 (1952), pp. 387–387. ISSN: 0031-899X. DOI: 10.1103/PhysRev.87.387. URL: https://link.aps.org/doi/10.1103/PhysRev.87.387.

[32] Umesh K. Mishra and J. Singh. *Semiconductor Device Physics and Design*. Dordrecht: Springer Netherlands, 2007. ISBN: 978-1-4020-6480-7. DOI: 10.1007/978-1-4020-6481-4. URL: http://link.springer.com/10.1007/978-1-4020-6481-4.

[33] X. A. Cao et al. “Investigation of radiative tunneling in GaN/InGaN single quantum well light-emitting diodes”. In: *Solid-State Electronics* 46.12 (2002), pp. 2291–2294. ISSN: 00381101. DOI: 10.1016/S0038-1101(02)00190-9.

[34] X. A. Cao et al. “Defect generation in InGaN/GaN light-emitting diodes under forward and reverse electrical stresses”. In: *Microelectronics Reliability* 43.12 (2003), pp. 1987–1991. ISSN: 00262714. DOI: 10.1016/j.microrel.2003.06.001.

[35] V. Veleschuk et al. “Electroluminescence of InGaN / GaN heterostructures at the reverse bias and nitrogen temperature”. In: *Optica Applicata* XLV.4 (2015). DOI: 10.5277/oa150409.

[36] Eunjin Jung et al. “Leakage Current Analysis of GaN-Based Light-Emitting Diodes Using a Parasitic Diode Model”. In: *IEEE Transactions On Electron Devices* 62.10 (2015), pp. 3322–3325.

[37] Qifeng Shan et al. “Transport-mechanism analysis of the reverse leakage current in GaInN light-emitting diodes”. In: *Applied Physics Letters* 99.25 (2011), pp. 2009–2012. ISSN: 00036951. DOI: 10.1063/1.3668104.

[38] Kyu Sang Kim, Jin Ha Kim, and S. N. Cho. “Leakage current characteristics of nitride-based InGaN light-emitting diode”. In: *IEEE Photonics Technology Letters* 23.8 (2011), pp. 483–485. ISSN: 10411135. DOI: 10.1109/LPT.2011.2109705.

[39] Pei Wang et al. “Simulation of current spreading for GaN-based light-emitting diodes”. In: *Optics and Laser Technology* 42.5 (2010), pp. 737–740. ISSN: 00303992. DOI: 10.1016/j.optlastec.2009.11.018.

[40] Han-Youl Ryu and Jong-In Shim. “Effect of current spreading on the efficiency droop of InGaN light-emitting diodes.” In: *Optics express* 19.4 (2011), pp. 2886–2894. ISSN: 1094-4087. DOI: 10.1364/OE.19.002886.

[41] S. Vaccari. “Electrostatic Discharges on LEDs”. PhD thesis. Padua, pp. 83–108.

[42] M. Buffolo et al. “Failure of High Power LEDs Submitted to EOS : Dependence on Device Layout and Pulse Properties”. In: (2016), pp. 1–5.

[43] D. V. Lang. “Deep-level transient spectroscopy: A new method to characterize traps in semiconductors”. In: *Journal of Applied Physics* 45.7 (1974), pp. 3023–3032. ISSN: 0021-8979. DOI: 10.1063/1.1663719. URL: http://aip.scitation.org/doi/10.1063/1.1663719.

[44] A Chantre, G Vincent, and D Bois. “Deep-level optical spectroscopy in GaAs”. In: *Physical Review B* 23.10 (1981), pp. 5335–5359. ISSN: 0163-1829. DOI: 10.1103/PhysRevB.23.5335. URL: https://link.aps.org/doi/10.1103/PhysRevB.23.5335.

[45] Andrew M Armstrong. “Investigation of deep level defects in GaN:C, GaN:Mg and pseudomorphic AlGaN/GaN films”. In: (2006).

[46] S. K. Zhang et al. “Photoionization study of deep centers in GaN/AlGaN multiple quantum wells”. In: *Journal of Vacuum Science & Technology B, Nanotechnology and Microelectronics: Materials, Processing, Measurement, and Phenomena* 28.3 (2010), pp. C3I10–C3I12. ISSN: 2166-2746. DOI: 10.1116/1.3268613.

[47] Roland Pässler. “Photoionization cross-section analysis for a deep trap contributing to current collapse in GaN field-effect transistors”. In: *Journal of Applied Physics* 96.1 (2004), pp. 715–722. ISSN: 00218979. DOI: 10.1063/1.1753076.

[48] Z-q Fang et al. “Deep centers in n -GaN grown by reactive molecular beam epitaxy”. In: *Applied Physics Letters* 72.18 (1998), pp. 2277–2279.

[49] A. R. Arehart et al. “Comparison of deep level incorporation in ammonia and rf-plasma assisted molecular beam epitaxy n-GaN films”. In: *Physica Status Solidi (C) Current Topics in Solid State Physics* 5.6 (2008), pp. 1750–1752. ISSN: 18626351. DOI: 10.1002/pssc.200778622.

[50] A R Arehart. “Investigation of electrically active defects in GaN, AlGaN, and AlGaN/GaN high electron mobility transistors”. In: (2009), pp. 1–402.

[51] Michael R. Hogsed. “Deep level defects in electron-irradiated aluminum gallium nitride grown by molecular beam epitaxy”. In: (2005).

[52] N. M. Shmidt et al. “Effect of annealing on defects in as-grown and γ-ray irradiated n-GaN layers”. In: *Physica Status Solidi (B) Basic Research* 216.1 (1999), pp. 533–536. ISSN: 03701972. DOI: 10.1002/(SICI)1521-3951(199911)216:1<533::AID-PSSB533>3.0.CO;2-S.

[53] J. Osaka et al. “Deep levels in n -type AlGaN grown by hydride vapor-phase epitaxy on sapphire characterized by deep-level transient spectroscopy”. In: *Applied Physics Letters* 87.22 (2005), pp. 1–3. ISSN: 00036951. DOI: 10.1063/1.2137901.

[54] P. Kamyczek et al. "A deep acceptor defect responsible for the yellow luminescence in GaN and AlGaN". In: *Journal of Applied Physics* 111.11 (2012). ISSN: 00218979. DOI: 10.1063/1.4725484.

[55] D. Kindl et al. "Deep defects in GaN/AlGaN/SiC heterostructures". In: *Journal of Applied Physics* 105.9 (2009). ISSN: 00218979. DOI: 10.1063/1.3122290.

[56] Z. Zhang et al. "Deep traps in nonpolar m-plane GaN grown by ammonia-based molecular beam epitaxy". In: *Applied Physics Letters* 100.5 (2012), pp. 1–5. ISSN: 00036951. DOI: 10.1063/1.3682528.

[57] Daniel Johnstone et al. "Comparison of deep levels in GaN grown by MBE, MOCVD, and HVPE". In: 5739 (2005), p. 7. ISSN: 0277786X. DOI: 10.1117/12.591047. URL: http://proceedings.spiedigitallibrary.org/proceeding.aspx?doi=10.1117/12.591047.

[58] P. Hacke et al. "Analysis of deep levels in n-type GaN by transient capacitance methods". In: *Journal of Applied Physics* 76.1 (1994), pp. 304–309. ISSN: 00218979. DOI: 10.1063/1.357144.

[59] A. R. Arehart et al. "Spatially-discriminating trap characterization methods for HEMTs and their application to RF-stressed AlGaN/GaN HEMTs". In: *Technical Digest - International Electron Devices Meeting, IEDM* 4 (2010), pp. 464–467. ISSN: 01631918. DOI: 10.1109/IEDM.2010.5703396.

[60] C D Wang et al. "Deep level defects in n-type GaN grown by molecular beam epitaxy". In: *Appl. Phys. Lett.* 72.10 (1998), pp. 1211–1213. ISSN: 0003-6951. DOI: 10.1063/1.121016.

[61] N. Renso et al. "Understanding the degradation processes of GaN based LEDs submitted to extremely high current density". In: *Microelectronics Reliability* 76-77.2016 (2017). ISSN: 0026-2714. DOI: 10.1016/j.microrel.2017.06.044. URL: http://dx.doi.org/10.1016/j.microrel.2017.06.044.

[62] F. Rossi et al. "The role of Mg complexes in the degradation of InGaN-based LEDs". In: *Superlattices and Microstructures* 36.4-6 (2004), pp. 859–868. ISSN: 07496036. DOI: 10.1016/j.spmi.2004.09.041. URL: https://www.sciencedirect.com/science/article/pii/S0749603604003210https://linkinghub.elsevier.com/retrieve/pii/S0749603604003210.

[63] R. Juday et al. "Hydrogen-related, deeply bound excitons in Mg-doped GaN films". In: *Applied Physics Letters* 103.8 (2013), pp. 8–13. ISSN: 00036951. DOI: 10.1063/1.4819029. URL: http://aip.scitation.org/doi/10.1063/1.4819029.

[64] Nicola Renso et al. "Evidence for avalanche generation in reverse-biased InGaN LEDs". In: *Light-Emitting Devices, Materials, and Applications*. Ed. by Martin Strassburg, Jong Kyu Kim, and Michael R. Krames. SPIE, 2019, p. 70. ISBN: 9781510625228. DOI: 10.1117/12.2511152. URL: https://www.spiedigitallibrary.org/conference-proceedings-of-spie/10940/2511152/Evidence-for-avalanche-generation-in-reverse-biased-InGaN-LEDs/10.1117/12.2511152.full.

[65] Hsiang Chen, Chyuan-haur Kao, and Tien-chang Lu. "Characterizing Reverse-bias Electroluminescence of InGaN/GaN LEDs". In: *CS Mantech*. Palm Springs, USA, 2011, pp. 253–256. ISBN: 1893580172.

[66] S.M. Sze and Kwok K. Ng. *Physics of Semiconductor Devices*. Hoboken, NJ, USA: John Wiley & Sons, Inc., 2006. ISBN: 9780470068328. DOI: 10.1002/0470068329. URL: http://doi.wiley.com/10.1002/0470068329.

[67] A. G. Chynoweth. "Ionization Rates for Electrons and Holes in Silicon". In: *Physical Review* 109.5 (1958), pp. 1537–1540. ISSN: 0031-899X. DOI: 10.1103/PhysRev.109.1537. URL: https://link.aps.org/doi/10.1103/PhysRev.109.1537.

[68] D. J. Massey, J. P.R. David, and G. J. Rees. "Temperature dependence of impact ionization in submicrometer silicon devices". In: *IEEE Transactions on Electron Devices* 53.9 (2006), pp. 2328–2334. ISSN: 00189383. DOI: 10.1109/TED.2006.881010.

[69] C. Haller et al. "GaN surface as the source of non-radiative defects in InGaN/GaN quantum wells". In: *Applied Physics Letters* 113.11 (2018). ISSN: 00036951. DOI: 10.1063/1.5048010. URL: http://dx.doi.org/10.1063/1.5048010.

[70] Shengjun Zhou et al. "Reverse leakage current characteristics of InGaN/GaN multiple quantum well ultraviolet/blue/green light-emitting diodes". In: *Japanese Journal of Applied Physics* 57.5 (2018). ISSN: 1347-4065. DOI: 10.7567/JJAP.57.051003.

[71] Linna Zhao et al. "Tunneling-Hopping Transport Model for Reverse Leakage Current in InGaN/GaN Blue Light-Emitting Diodes". In: *IEEE Photonics Technology Letters* 29.17 (2017), pp. 1447–1450. ISSN: 10411135. DOI: 10.1109/LPT.2017.2724143.

[72] Moonsang Lee et al. "Significant improvement of reverse leakage current characteristics of Si-based homoepitaxial InGaN/GaN blue light emitting diodes". In: *Scientific Reports* 9.1 (2019), pp. 1–6. ISSN: 20452322. DOI: 10.1038/s41598-019-38664-x. URL: http://dx.doi.org/10.1038/s41598-019-38664-x.

[73] Wolf Alexander Quitsch et al. "Low injection losses in InGaN/GaN LEDs: The correlation of photoluminescence, electroluminescence, and photocurrent measurements". In: *Journal of Applied Physics* 123.21 (2018). ISSN: 10897550. DOI: 10.1063/1.5022026.

[74] D. Mahaveer Sathaiya and Shreepad Karmalkar. "Thermionic trap-assisted tunneling model and its application to leakage current in nitrided oxides and AlGaN/GaN high electron mobility transistors". In: *Journal of Applied Physics* 99.9 (2006). ISSN: 00218979. DOI: 10.1063/1.2191620.

[75] Kenji Orita et al. "Analysis of Diffusion-Related Gradual Degradation of InGaN-Based Laser Diodes". In: *IEEE Journal of Quantum Electronics* 48.9 (2012), pp. 1169–1176. ISSN: 0018-9197. DOI: 10.1109/JQE.2012.2203795. URL: http://ieeexplore.ieee.org/document/6218742/.

[76] Shigetaka Tomiya et al. "Dislocation related issues in the degradation of GaN-based laser diodes". In: *IEEE Journal on Selected Topics in Quantum Electronics* 10.6 (2004), pp. 1277–1286. ISSN: 1077260X. DOI: 10.1109/JSTQE.2004.837735.

[77] Piotr Perlin et al. "Degradation mechanisms of InGaN laser diodes". In: *Proceedings of the IEEE* 98.7 (2010), pp. 1214–1219. ISSN: 00189219. DOI: 10.1109/JPROC.2009.2030826.

[78] C. De Santi et al. "Experimental Demonstration of Time-Dependent Breakdown in GaN-Based Light Emitting Diodes". In: *IEEE Electron Device Letters* 37.5 (2016), pp. 611–614. ISSN: 0741-3106. DOI: 10.1109/LED.2016.2543805. URL: http://ieeexplore.ieee.org/lpdocs/epic03/wrapper.htm?arnumber=7436711.

[79] C. H. Seager et al. "Drift, diffusion, and trapping of hydrogen in p-type GaN". In: *Journal of Applied Physics* 92.12 (2002), pp. 7246–7252. ISSN: 00218979. DOI: 10.1063/1.1520719.

[80] J. Glaab et al. "Degradation of (In)AlGaN-Based UVB LEDs and Migration of Hydrogen". In: *IEEE Photonics Technology Letters* 31.7 (2019), pp. 529–532. ISSN: 10411135. DOI: 10.1109/LPT.2019.2900156.

[81] Cyrus E. Dreyer et al. "Gallium vacancy complexes as a cause of Shockley-Read-Hall recombination in III-nitride light emitters". In: *Applied Physics Letters* 108.14 (2016), p. 141101. ISSN: 0003-6951. DOI: 10.1063/1.4942674. URL: http://aip.scitation.org/doi/10.1063/1.4942674.

[82] John L. Lyons et al. "First-principles theory of acceptors in nitride semiconductors". In: *Physica Status Solidi (B) Basic Research* 252.5 (2015), pp. 900–908. ISSN: 15213951. DOI: 10.1002/pssb.201552062.

[83] I. S. Romanov et al. "Effect of Magnesium Diffusion Into the Active Region of LED Structures with InGaN/GaN Quantum Wells on Internal Quantum Efficiency". In: *Russian Physics Journal* 57.4 (2014), pp. 533–535. ISSN: 15739228. DOI: 10.1007/s11182-014-0271-1.

[84] Lutz Kirste et al. "SIMS depth profiling of Mg back-diffusion in (AlGaIn)N light-emitting diodes". In: *Journal of Materials Science: Materials in Electronics* 19.SUPPL. 1 (2008), pp. 176–181. ISSN: 09574522. DOI: 10.1007/s10854-007-9515-y.

[85] Shigefusa F. Chichibu et al. "Room temperature photoluminescence lifetime for the near-band-edge emission of epitaxial and ion-implanted GaN on GaN structures". In: *Japanese Journal of Applied Physics* 58.SC (2019), SC0802. ISSN: 0021-4922. DOI: 10.7567/1347-4065/ab0d06.

[86] S. F. Chichibu et al. "The origins and properties of intrinsic nonradiative recombination centers in wide bandgap GaN and AlGaN". In: *Journal of Applied Physics* 123.16 (2018). ISSN: 10897550. DOI: 10.1063/1.5012994.

[87] Otto Pursiainen et al. "Identification of aging mechanisms in the optical and electrical characteristics of light-emitting diodes". In: *Applied Physics Letters* 79.18 (2001), pp. 2895–2897. ISSN: 00036951. DOI: 10.1063/1.1413721.

[88] I. S. Romanov, I. A. Prudaev, and V. N. Brudnyi. "Diffusion of Magnesium in Led Structures with InGaN/GaN Quantum Wells at True Growth Temperatures 860–980°C of p-GaN". In: *Russian Physics Journal* 61.1 (2018), pp. 187–190. ISSN: 15739228. DOI: 10.1007/s11182-018-1383-9.

[89] T. H. Gfroerer et al. "Impact of superlinear defect-related recombination on LED performance at low injection". In: *Journal of Applied Physics* 125.20 (2019), p. 204502. ISSN: 0021-8979. DOI: 10.1063/1.5089125. URL: http://aip.scitation.org/doi/10.1063/1.5089125.

[90] Marco Mandurrino et al. "Physics-based modeling and experimental implications of trap-assisted tunneling in InGaN/GaN light-emitting diodes". In: *Physica Status Solidi (A) Applications and Materials Science* 212.5 (2015), pp. 947–953. ISSN: 18626319. DOI: 10.1002/pssa.201431743.

[91] M. Auf Der Maur et al. "Trap-assisted tunneling in InGaN/GaN single-quantum-well light-emitting diodes". In: *Applied Physics Letters* 105.13 (2014). ISSN: 00036951. DOI: 10.1063/1.4896970.

[92] Robert M. Hill. "Hopping conduction in amorphous solids". In: *Philosophical Magazine* 24.192 (1971), pp. 1307–1325. ISSN: 00318086. DOI: 10.1080/14786437108217414.

[93] M Gassoumi et al. "Evidence of surface states for AlGaN / GaN / SiC HEMTs passivated Si 3 N 4 by CDLTS". In: (2012), pp. 396–399.

[94] Engin Arslan et al. "The persistent photoconductivity effect in AlGaN/GaN heterostructures grown on sapphire and SiC substrates". In: *Journal of Applied Physics* 103.10 (2008). ISSN: 00218979. DOI: 10.1063/1.2921832.

[95] A. R. Arehart et al. "Direct observation of 0.57 eV trap-related RF output power reduction in AlGaN/GaN high electron mobility transistors". In: *Solid-State Electronics* 80 (2013), pp. 19–22. ISSN: 00381101. DOI: 10.1016/j.sse.2012.09.010. URL: http://dx.doi.org/10.1016/j.sse.2012.09.010.